Title
The effect of Amyloid Precursor Protein (APP) and APP-cleavage Products on Spinal Locomotive Circuit

Author
Huang, Ruyi

Publication Date
2017

Peer reviewed|Thesis/dissertation

UNIVERSITY OF CALIFORNIA

Los Angeles

The effect of Amyloid Precursor Protein (APP) and APP-cleavage Products on Spinal Locomotive Circuit

A dissertation submitted in partial satisfaction

of the requirements for the degree

Doctor of Philosophy in Neuroscience

by

Ruyi Huang

2017

ABSTRACT OF THE DISSERTATION

The effect of Amyloid Precursor Protein (APP) and APP-cleavage Products on Spinal Locomotive Circuit

by

Ruyi Huang

Doctor of Philosophy in Neuroscience

University of California, Los Angeles, 2017

Professor Daniel C. Lu, Chair

Amyloid Precursor Protein (APP) was first identified in 1987 as one of the most important biomarkers in the Alzheimer's disease (AD) subject brain tissue. Besides being involved in AD cognitive deficits, there is an accumulating body of evidence supports that APP and APP-cleavage products participate in multiple pathological and physiological processes in brain, spinal cord and the peripheral nervous system. In this study, we are interested in the effect of APP and APP-cleavage products on spinal circuit based locomotion. While the cognitive deficits related to AD have being thoroughly studied, locomotion impairments observed in AD patients as well as in transgenic model animals are understudied. Locomotion deficits like loss of balance and slowness in stepping speed were previously thought to be caused by brain degeneration and only occurring late in the disease progression (3). However, there is evidence showing that motor deficits precede cognitive failure (4). Recent researches show that, spinal cord changes have been observed in early

stage of AD. It is possible that AD pathology also happens locally in the spinal cord, contributing to AD-related motor deficits.

In this study, I aim to address two hypotheses:

1) APP and APP-cleavage products in spinal cord participate in locomotion regulation in an expression dependent manner;

2) APP and its cleavage products impair neuronal plasticity in spinal cord as they do in the brain.

To test these two questions, I first investigated the APP/Aβ expression in AD patient spinal cord. Immunohistochemistry staining in AD spinal cord showed an increase in Aβ immunoreactivity. I further investigated if the spinal Aβ increase was correlated with locomotion deficits by using a human APP over-expressing model mouse, PDGFβ-$APP_{Sw/Ind}$ (J20) (Fig 1-1). The locomotion of J20 mice was tested before and after complete spinal cord transection, and the spinal learning was also evaluated by an instrumental learning paradigm, paw withdrawal learning paradigm (PaWL). Changes in locomotion kinematics patterns and spinal learning have been detected in J20 mice when compared to their WT littermates. These alternations are correlated to the lumbar spinal hAβ expression level and down-regulating the spinal Aβ expression levels can restore locomotion function in both intact and spinal cord transected J20 mice.

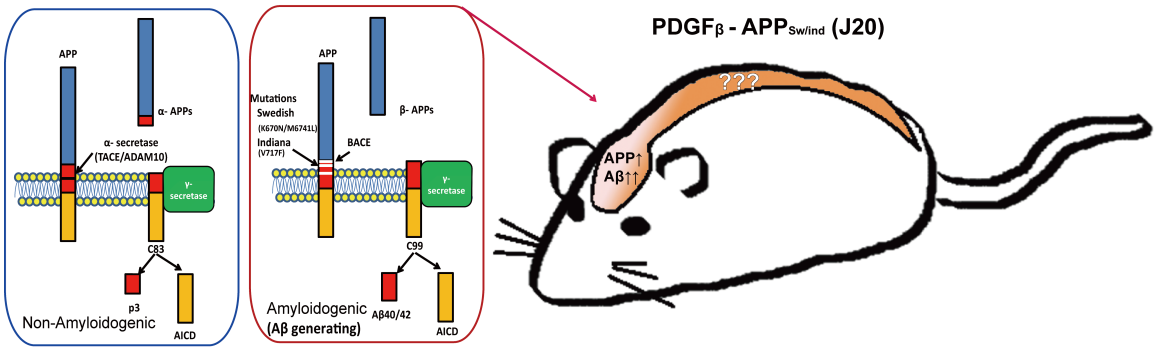

Figure 1- 1

Figure 1-1 Illustration of APP/ Aβ overexpression transgenic mouse model, J20.

Full length APP is subjected to 3 secretases: α-, β- and γ-secretase. The full length APP will generate non-amyloidogenic products (p3) when it is subject to the sequential cleavages of α- and γ-secretase. When APP undergoes the sequential cleavages by β- and γ-secretase, the amyloidogenic Aβs ($Aβ_{40}$, $Aβ_{42}$) are generated. Because J20 mouse overexpresses two mutated human APP genes, which contain the point mutations on the β- and γ-secretase cleavage sites that help to increase the generation of Aβs, APP/ Aβ is overexpressed in J20 mouse. The overexpressed human mutated APP genes are driven by the platelet-derived growth factor-β ($PDGF_β$) promoter, which only expressed in the central nervous system.

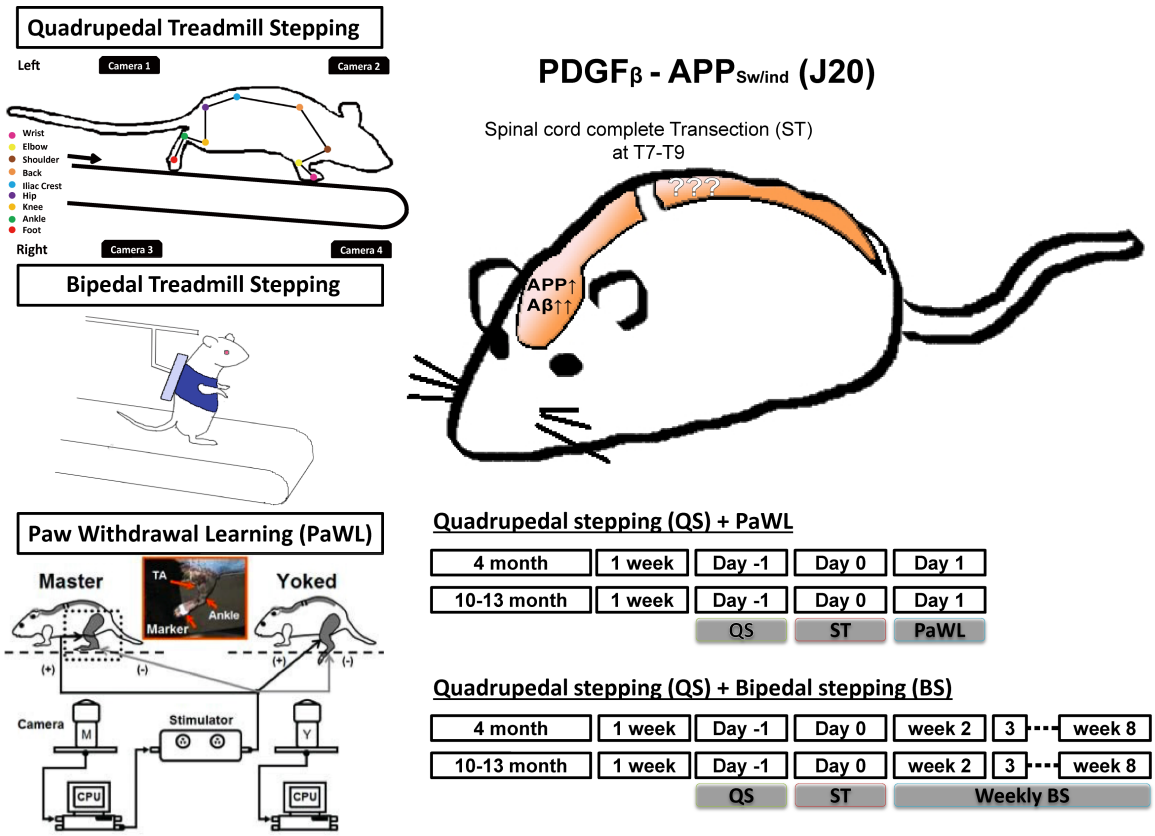

Figure 1- 2

Figure 1-2. Illustration of the experimental design and timeline.

Three different behavioral tests are performed to evaluate the locomotion or locomotion-related function of J20 mice: quadrapedal treadmill stepping test, bipedal treadmill stepping test and paw withdrawal-learning (PaWL) paradigm.

The dissertation of Ruyi Huang is approved.

S. Lawrence Zipursky

Michael Sofroniew

Tom O'Dell

Victor R. Edgerton

Daniel C Lu, Committee Chair

University of California, Los Angeles

2017

TABLE OF CONTENT

LIST OF FIGURES AND TABLES

DEDICATION

This dissertation is dedicated to my beloved mother

Yongwei Zou

And

my father

Xiaofeng Huang

You have cultivated my curiosity and courage in exploring this world.

ACKNOWLEDGEMENTS

First of all, I would like to thank my beloved family, my parents Yongwei Zou and Xiaofeng Huang for their sacrifice so that I could have this opportunity to accomplish my studies and do what I have dreamt to do. I would like to thank my grandparents, Gaoyu Zhang and Zhijie Huang as well as my late grandparents, Benhu Zou and Chengjia Yang for their support, encouragement and love in helping me accomplish my studies. I would also like to thank my dear aunt Yongrui Zou and uncle Hua Gu for introducing the love of science into my heart.

I would like to thank my Committee Chair and advisor, Professor Daniel C Lu for academic guidance, professional development, opportunity and his unwavering support during my graduate studies. I want to thank my two wonderful co-mentors, Professor. Reggie Edgerton and Professor James Leiter for mentoring me to acquire skills, knowledge, and expertise in research and for always providing me with constructive criticism. I would like to thank the remaining advisor, Professor Michael Sofroniew, Professor Tom O'Dell, and Professor Lawrence Zipursky, for their academic support and guidance in my progress towards the completion of my doctoral studies. I consider myself to be uniquely fortunate to have worked with such great mentors and scientists. Thank you.

I would like to extend my hearty gratitude to my lab mates and friends, Lisa Moore, Erika Galer, Tali Homsey, Hamid Ghasemi, Stephanie Wang, Selvan Michael Joseph, Dr. Niranjala Tillakaratne, Shron Zdunowski, Dr. Roland Roy, Dr. Hui Zhong, Benita Jin, Bo Xu, Sajedeh Eftekhari, Seok White, Yangzi She, Sisi Feng, Bau Pham, Kyeigh De Petro, Naomi Gonzalez, Amanda Turner, Vanessa Contreras, Timothy Le, Yin Yang, Jinnan Li, Bo Wang, Mengjie

Wu, Cenlin He, Yuting Guan, Jinxing Li, Kazu Christopher, Xiuzhe Wu and Jingyi Li, for all their help, love, friendship and emotional support in the process of completing my studies.

Special thanks to my undergraduate research assistants: Xingquan Liu (Tony), Yeji Seo, Ashok Bhattarai, Lai-Yan Li, Marisela Iglesia, Woo Jung Kim, Alyssa Go, Nicholas Zahos and Shane Shahrestani. Thank you so much for your extreme hard working and commitment in data analysis, animal surgery shadowing, covering animal care, etc. for my project.

Thank you all.

Curriculum Vitae

Education

PhD candidate, Neuroscience IDP, University of California Los Angeles (UCLA) — Expected Jun 2017

CSST UCLA Summer Research Program — Summer 2009

B.S. Fudan University, Shanghai — 2006 - 2010

Professional Experience

UNIVERSITY OF CALIFORNIA, LOS ANGELES (UCLA)

DEPARTMENT OF NEUROSURGERY, LABORATORY OF DANIEL LU, GRADUATE RESEARCHER — 2013-Present

PROJECT: Investigating spinal cord circuit changes in Alzheimer's Disease (AD) model mice PDGF-APP$_{Swe-ind}$ (J20).

DEPARTMENT OF PHARMARCHOLOGY, LABORATORY OF YI SUN, GRADUATE RESEARCHER — 2011 -2013

PROJECT: Suppressing the microRNA interaction network in MeCP2 knockout Rett's Syndrome model neural cells and restoring BDNF expression.

FUDAN UNIVERSITY

BRAIN INSTITUTE, LABORATORY OF YU-QIU ZHANG, UNDERGRADUATE RESEARCHER — 2007 -2010

PROJECT: SIP30 in anterior cingulated cortex contributes to the induction of pain-related negative emotional effect in rats.

HONORS & FELLOWSHIP

2017 Young Investigator of Alzheimer's Drug Discovery Foundation — 2017-2015

Society of Neuroscience Travel Grant, UCLA NSIDP

China Scholar Council Fellowship — 2010-2014

Thermo-Fisher Scientific Scholarship — 2010

Fudan University, Chancellor Prize — 2007-2009

PUBLICATIONS

1. Hindlimb locomotion deficits are related to spinal beta amyloid in both intact and spinal Alzheimer's disease model J20 mice
   Huang RY* , Joseph MS, Zhong H, Seo Y, Liu XQ, Guo W, McArthur D, Shahrestani S, Roy RR, KOO E, Leiter JC, Edgerton VR, Lu DC. Manuscript *in preparation.* 2017

2. Identify locomotion kinematics changes reflect Alzheimers pathological changes using Support Vector Machine
   Huang RY* , Ghasemi H* , Xu Bo, Joseph MS, Seo Y, Liu XQ, Shahrestani S, KOO E, Edgerton VR, Lu DC. Manuscript *under review.* 2017

3. Modulation of respiratory output by cervical epidural stimulation in the anesthetized mouse
   Huang RY* , Baca SM* , Worrell JW, Liu XQ, Seo Y, Guo W, Leiter JC, Lu DC. J Appl Physiol, 2016 Oct 7, doi: 10.1152/japplphysiol.00473.2016 2016

4. SIP30 Is required for neuropathic pain-evoked aversion in rats.
   Han M* , Xiao X, Yang Y, **Huang RY,** Cao H, Zhao Z, Zhang Y. The Journal of Neuroscience, 2014 January 8, 34(2): 346-355; doi: 10.1523/JNEUROSCI.3160-13.2014 2014

5. Early intervention of ERK activation in the spinal cord can block initiation of peripheral nerve injury-induced neuropathic pain in rats. 2011
   Han M* , **Huang RY*** , Du Yiming, Zhao Zhiqi, Zhang Yuqiu, Sheng Li Xue Bao. 2011 Apr 25;63(2):106-14.

CONFERENCES

1. Hindlimb locomotion pattern changes are detected in both the intact and spinal Alzheimer's disease model J20 mice with a spinal learning paradigm
   Huang RY* , Joseph MS, Zhong H, Seo Y, Liu XQ, Guo W, McArthur D, Shahrestani S, Roy RR, KOO E, Edgerton VR, Lu DC. Alzheimer's disease drug discovery conference, Oral Presentation. 2017

2. Lumbar beta amyloid accumulation impairs spinal learning in J20 mice
   Huang RY* , Joseph MS, Zhong H, Seo Y, Liu XQ, Guo W, McArthur D, Shahrestani S, Roy RR, KOO E, Edgerton VR, Lu DC. UC Neurotrauma Meeting, Oral Presentation. 2016

3. Hindlimb locomotion pattern changes are detected in both the intact and spinal Alzheimer's disease model J20 mice
   Huang RY* , Joseph MS, Zhong H, Roy RR, McArthur D, KOO EH, Edgerton VR, Lu DC. Society of Neuroscience, Poster 2015

4. Locomotion deficits detected in Alzheimer's disease model J20 mice
   Huang RY* , Joseph MS, Zhong H, Roy RR, McArthur D, KOO EH, Edgerton VR, Lu DC. UC Neurotrauma Meeting, Oral Presentation 2015

CHAPTER OVERVIEW

Chapter 1 is the literature review of background significance for understanding the effects of APP and its cleavage products. The effect APP and APP-cleavage products on the learning and memory as well as the locomotion rehabilitation after spinal cord injury are reviewed in this chapter with emphasis.

Chapter 2 describes a supportive vector machine (SVM) based mathematical model our lab established for identifying subtle changes in locomotion kinematics that classify J20 and WT locomotion patterns. Locomotion kinematics data of J20 and WT were collected from the quadrupedal gait pattern in intact mice, whose locomotion control and regulation were executed by both brain and spinal cord.

The aim of **Chapter 3** is to identify the locomotive spinal circuit changes by studying the spontaneous hind limb locomotion recovery in complete spinal cord transected J20 mice. In order to investigate spinal locomotion circuit without supraspinal inputs, complete spinal cord transection was applied to the tested animal groups to separate the lumbosacral spinal cord completely from any superior central nervous system (CNS) structures. The bipedal treadmill stepping test was used to evaluate the spontaneous locomotion recovery in spinalized J20 mice. In bipedal stepping test, the J20 mice demonstrated a delay in locomotion recovery. This result suggests that a local hAPP/hAβ overexpression in lumbar spinal cord might impair the plasticity of the locomotive spinal circuit.

In **Chapter 4**, to investigate the lumbar locomotive spinal circuit plasticity changes, we tested the spinal learning in completely transected J20 and WT mice using the paw withdrawal learning (PaWL) paradigm. In PaWL paradigm, spinal mice dorsiflex the hind

paw in response to position-dependent mild electric shocks to the tibialis anterior muscle and learn to hold the paw to minimize the net exposure to shocks. This simple *in vivo* learning model provides an opportunity to identify molecules and neural pathways that mediate spinal learning in mammals, while the important molecular substrates of instrumental learning in the spinal mouse have been validated by pharmacological manipulations and viral tracing[1,2]. We discover that the J20 spinal mice took longer time in learning to respond successfully towards the electric stimulation, comparing to the WT littermates. Further analysis show that the quality of PaWL learning in J20 mice is negatively correlated to the lumbar soluble $A\beta_{42}$ expression level. This result suggests that the lumbar soluble $A\beta_{42}$ may cause the impairments observed in lumbar locomotive circuit.

In **Chapter 5** test the hypothesis that lumbar soluble $A\beta_{42}$ increase causes locomotive spinal circuit plasticity and spinal learning deficits, new Aβ generations in J20 and WT mice were blocked by γ-secretase inhibitor (GSI, LY411575). The quadrupedal treadmill stepping kinematics pattern, the spontaneous bipedal locomotion recovery and the spinal learning assessed by PaWL were all tested with GSI to explore whether GSI application in J20 mice can rescue the locomotive deficits observed earlier.

Chapter 6 Because GSI also targets the Notch signaling pathway, the long-term application of GSI in AD model animals and patients could cause side effects. In this chapter, we are trying to search alternative methods, which can also modulate spinal cord circuit. I found that the electrical epidural stimulation on cervical spinal cord is efficient in modulating the respiration rhythm of WT BL6 mice. Because locomotion and respiration are both rhythmic activities, applying electrical epidural stimulation on lumbar spinal cord may also facilitate and correct the locomotion patterns as well as modulating the lumbar circuit plasticity in J20 mice.

CHAPTER 1: Background and Significance

Impact of Alzheimer's disease

Alzheimer's disease (AD) is a devastating neurodegenerative disease. As the leading cause of dementia in the aging population, AD is estimated to hit over 10 million people in the United States, and the United States alone will see a ~50% annual increase of AD by the year 2025 [3]. However, there hasn't been an effective way to cure, prevent or even halt AD yet.

Alzheimer's disease and the amyloid hypothesis

Understanding the causes and underlying mechanisms of Alzheimer's disease has always been a challenge since the first day it was described. When Alois Alzheimer first described the neuropathological syndrome of Alzheimer's disease (AD) in 1907[4], two characteristic lesions, 'plaques and tangles', were emphasized. Plaques and tangles refer to the dense amyloid depositions and the paired helical filaments composed of phosphorylated microtubule-associated protein tau respectively. It took a further 75 years before Allsop et al. identified biochemically the major constituent of these amyloid plaques as a 40-42 amino acid peptide termed amyloid-β (Aβ)[5]. Subsequent research determined that this peptide fragment originated from a larger precursor protein, which consists about 700 amino acids, named somewhat predictably, the amyloid-β precursor protein (APP)[6]. These advances led to the formulation of the amyloid hypothesis, which states that overproduction of Aβ and its aggregation in senile plaques is the root cause of AD[7]. Although the hypothesis received further supports (e.g. genetic studies revealed that all cases of familial AD are linked to genes that affect the processing of APP[8–13], the roles of Aβ in neurotoxicity[14–17]), the failure of APP as well as Aβ targeting clinical trials casts a shadow on the amyloid hypothesis.

There's no one hypothesis is resolute and demonstrating whether Aβ accumulation is a cause or effect of all AD up to date. Indeed, familial type AD only accounts for 2-3% of all cases of AD; what's more, neurofibrillary tangle formation correlates better with cognitive decline than amyloid plaque burden. These facts raise questions about the significance of plaque amyloid. Consideration has been given to Aβ deposition being merely a side effect of the disease process in which tangles play a primary role. Neurofibrillary tangles are composed of hyperphosphorylated tau proteins[18–24], which appear to play a role in microtubules function in normal brain and spinal cord[20,25].

However, Aβ has still remained a central feature of neurobiological research into AD through three significant reasons. **First,** abnormality of tau cannot fully explain AD pathology[26]. **Secondly**, many clinical failures are due to strong side-effect of the APP/ Aβ targeting drugs, suggesting that physiological processes have been impaired when blocking APP processing. This suggestion has been further supported by researches of APP and its cleavage products role in neural development, brain/spinal cord injury and learning/memory[27–31]. It is possible that current APP/Aβ targeting drugs failures are caused by the shifting of APP/ Aβ homeostatic point interferes physiological functions that leading to there has been a shift in emphasis away from the dense core amyloid to smaller aggregates, such as soluble oligomers and fibrils[32–42], as being major contributors to neural dysfunction[43–48]. The level of soluble Aβ is raised in AD and correlated with the disease symptomatology. Furthermore, soluble Aβ exerts a number of physiological and cellular effects that may be sufficient to account for much of the cognitive decline, including lose of synapses, especially early in the course of AD before plaques formation[26,32]. With these new developments has come a shift in the research toward understanding in more detail 1) the physiological actions of soluble Aβ, and 2) the normal functions performed by APP both in the AD brain and other parts of neural

system, in order to more fully comprehend the disease process. In association with the resulting increased appreciation of the multiple roles play by APP and its fragments in neuronal cell biology, there has been a resurgence of interest in the amyloid hypothesis. This is reflected in the numerous recent researches that touch on various aspects of APP processing and the activity of its fragments[49–52]. APP function is suggested more than just an "amyloid precursor"[28]. Its full role in the central nervous system is still an enigma.

What is APP?

APP is a single membrane-spanning protein possessing a large extracellular amino-terminal domain and a small intracellular cytoplasmic domain. Within the extracellular domain the protein has a cysteine-rich subdomain close to the extreme amino terminus, followed by an acidic subdomain, and two other subdomains, one of which has been deduced to have a neuroprotective function[6,8]. A number of functional domains have since been mapped to the extra- and intracellular regions of APP. These include metal (copper and zinc) binding, extracellular matrix components (heparin, collagen, and laminin), neurotrophic and adhesion domains, and protease inhibition domains[6,11,29,53,54].

Human APP is a member of the APP family of proteins, which also includes APP-like protein 1 and 2 (APLP1 and APLP2). This family is conserved across a variety of species, and members can be found in both vertebrates and invertebrates but not in prokaryotes, plants and yeasts. APP, APLP1, and APLP2 are all single-pass transmembrane proteins with a small intracellular C-terminal domain and a large N-terminal extracellular region reminiscent of a transmembrane receptor protein. Notably, APP is the only family member with an Aβ peptide domain[53].

The APP gene is localized to chromosome 21 (21q21.2-3) and is expressed in many cell and tissue types including endothelia, glia and neurons[29]. The pre-mRNA is alternatively spliced to produce three major protein isoforms APP_{770}, APP_{751}, and APP_{695}[29]. APP_{695} is the only isoform that lacks a kunitz protease inhibitor (KPI) domain in its extracellular portion although the functional relevance of this domain is unclear. Interestingly, in different neural structures, the ratio of three isoforms is different. The brain neuron seems to predominantly produce the 695 amino acid non-KPI-containing APP isoform (APP 770:751:695 mRNA ratio is 1:10:20[55]), while astrocytes predominantly express KPI-containing APPs (APP 770:751:695) [53].

APP participated in normal neuronal function

APP is a resource-rich molecule. It has at least three isoforms arising from the alternative splicing of its pre-mRNA, it is extensively processed post-translationally by both glycosylation and specific proteolytic cleavage[56,57], and the resulting fragments seem to participate widely in adhesion, neurotrophic and neuroproliferative activity, intercellular communication and membrane-to-nucleus signaling[14,15,29]. Based on these characteristics it was presumed that APP must serve critically important functions. Therefore, it was not surprising to discover the APP knockout mice were viable but exhibited several different types of deficits, including reduced brain weight[58], axonal growth/white matter defects[58], altered performance in learning and memory tasks[59,60], as well as axonal growth/transport defects[61–63]. While APP knockout didn't affect the animal viability, the combined gene knock-outs of APP, APLP1 and APLP2 was perinatal lethal[63]. This result indicates that APLP1 and APLP2, existing in both humans and mice, have very similar function to APP in many biochemical pathways. Furthermore, these results suggest that APP and the APP-like proteins are together involved in functions and pathways that are essential to normal

metabolism and development. Interestingly, the fragment of APLP1 and APLP2 that corresponds to Aβ does not form amyloid plaques[53].

APP processing and Aβ generation

APP undergoes a series of proteolytic processing before releasing Aβ peptides. With a complex processing pathway that results in secretion of relatively large fragments of ~600 amino acids that are derived from the extracellular amino-terminal domain and, depending on the cleavage pattern, smaller fragments including Aβ as well as various C-terminal fragments (typically 83 or 99 amino acids in length but also smaller fragments [53].

APP secretases

Two predicted cleaves, one in the extracellular domain (β-secretase cleavage) and the other in the transmembrane region (γ-secretase cleavage), are necessary to release Aβ from the precursor molecule. APP is first cleaved within the lumenal domain by α- or β- secretase, resulting in the shedding of nearly the entire ectodomain and generation of membrane-tethered α- or β- C- terminal fragments respectively. The α- or β- C- terminal fragments are subsequently cleaved within the transmembrane domain by γ-secretase to release p3 (3kDa) and Aβ (4kDa) peptides, respectively, into the extracellular milieu. In addition, γ-secretase cleavage generates a cytoplasmic polypeptide termed AICD (the amyloid precursor protein intracellular domain).

γ –Secretases and Aβs generation

γ -secretase is made of four essential subunits: presenilin-1 or -2, nicastrin, APH-1, and PEN-2. γ -Secretase cleaves at multiple sites within the transmembrane domain of APP, generating

Aβ peptides ranging in the length from 38 to 43 residues. Nearly 90% of secreted Aβ ends in residue 40, whereas Aβ42 accounts for <10% of secreted Aβ. Moreover, minor amounts of shorter Aβ peptide such as Aβ38 and Aβ37 have also been detected. Familial AD-linked mutations in APP just beyond the C terminus of the Aβ domain increase Aβ42 production.

Aβ Aggregation

Aβ peptides vary in size from 39 to 43 amino acids. Different types of Aβs exist as monomers, dimers, and higher oligomers [64], while further aggregation yields protofibrils and then fully-fledged fibrils that seem to compose the bulk of the amyloid plaques in AD brain tissue [35,65,66]. In vitro experiments demonstrate that aggregation into fibrils is dependent on both time and concentration [64]**.** These characteristics fit neatly with two observed risk factors for AD, namely age and an increase in production of the fibrillogenic 1-42 fragment in many familial types of AD [35,64]. Intriguingly, the time-dependence of aggregation is due to what is termed the "lag phase". During the lag phase no aggregation is detectable, after the lag phase, aggregation proceeds very rapidly. This suggests that nucleation from a peptide of different structure is necessary, much like seeding a crystallization process. This hypothesis is supported by the observation that seeding Aβ monomers with pre-aggregated Aβs can eliminate the lag phase[67–69]This suggests an acute effect of soluble forms of amyloid shift the homeostasis state of the Aβs aggregating process. While $A\beta_{42}$ aggregates more readily than any other Aβs [67–71], the ratio of soluble $A\beta_{42}$ and the most abundant version of soluble Aβ, soluble $A\beta_{40}$, change reflects the Aβs aggregation homeostasis shifts the best. It is interesting that while soluble $A\beta_{42}$ amount or phosphorylated-tau amount only in patients' cerebral spinal fluid (CSF) discrepant with the clinician's diagnosis, CSF soluble $A\beta_{42/}$ $A\beta_{40}$ ratio leads to a reliable biological conclusion in over 50% of cases that agreed with the diagnosis[72,73],

Aβ peptides and Learning and memory

These Aβ peptides arise from β and γ-secretase processing of APP has received much attention as a major player in AD. Many researches support that soluble Aβ is toxic to cultured cells of various types[50,74–80] and also has long-term damaging effects when injected directly into the brain[35,64,65,81,82]. Both exogenously applied and endogenously expressed Aβ can regulate learning and retention of an active avoidance response[49]. Several Aβ peptide fragments ($A\beta_{12-28}$, $A\beta_{18-28}$ and $A\beta_{12-20}$) were effective in causing dose-dependent reductions in memory retention[34,69,81]while, peptide injections into several specific limbic structures, including the hippocampus, were also amnestic [83].

Synthetic peptides, including $A\beta_{40}$, $A\beta_{42}$, and $A\beta_{25-35}$ [38,68,69,84], as well as naturally secreted oligomers of Aβ [66] have been found to inhibit the formation of LTP. The inhibition of LTP is not due to covert aggregation into fibrils, since fibril-free peptide carefully prepared in organic solvents and characterized by atomic force microscopy[47,71,85]was observed to be as potently inhibitory as peptide kept nominally soluble in less carefully controlled conditions in other solutions. On the other hand, LTP inhibition is dependent on soluble oligomer formation, since Aβ monomers appear to be inactive against LTP [86]. LTP inhibition is also unrelated to neurotoxicity. First, the effects have a rapid onset without significantly affecting basal synaptic transmission [31]. Second, and critically, peptide substitutions at position 35, which prevent cytotoxicity in cultured neurons, do not affect the inhibition of LTP [86].

While the inhibition of LTP by Aβ has been consistently reported, there is less agreement over whether Aβ acutely affects LTD. Two studies have found no effect of soluble Aβ on LTP in either area CA1 ($A\beta_{1-40,}$ [87]) or the dentate gyrus ($A\beta_{1-42,}$ [88,89]) of hippocampal slices. In contrast, the exogenous $A\beta_{1-42}$ facilitates the induction of LTD in area CA1 of anesthetized

animals. One way that these apparently diverse findings can be reconciled is if Aβs act *in vivo* by regulating modulatory pathways afferent to the hippocampus that would be absent in hippocampal slice preparations.

In summary, exogenous Aβ clearly has a potent inhibitory effect on the induction of hippocampal LTP, and possibly facilitates LTD. However, it appears that Aβ acts not through inhibiting the initial induction mechanisms, such as NMDA receptor activation, but rather through regulation of the downstream signaling cascades. Unfortunately, little is known about the mechanisms that are triggered to cause these alterations in synaptic plasticity. The regulation of MAPK and PKA provide useful clues for future experiments, but undoubtedly many other signaling molecules need to be investigated, including the key receptor for Aβ, before a complete picture will emerge. No studies have yet directly addressed whether endogenous Aβ peptide, whether present intra- or extracellularly, regulates synaptic plasticity. However, major reductions in Aβ peptide levels caused by PS1 knockout strategies leave LTP and LTD unaltered [86], suggesting that the peptide does not exert a constitutive regulation of synaptic plasticity, either because it is not reduced to low enough concentrations or because it does not have access to the regulatory machinery.

APP and Aβ expression in spinal cord

Though often reported as a biomarker of AD highly expressed in cortex and hippocampus, APP is ubiquitously expressed in many cell and tissue types including endothelia, glia and neurons of the brain and spinal cord. However, the majority of research is focus on brain APP instead of the one in spinal cord. Recent researches indicate that APP increase in spinal cord correlate with neuropathological states, including motor neuron death, lost of synapses, and a shift of neuronal excitability homeostasis. Nevertheless, motor deficits like loss of balance

are also features of AD and usually precede cognitive failure. It is possible that there are changes affecting the spinal cord contributing to AD-related motor deficits.

There are more and more researches supported the hypothesis that the spinal APP expression has a correlation with motor degenerative diseases. Amyotrophic lateral sclerosis (ALS) onset is accompanied by an increase in APP, and elevated levels of both APP and Aβ have been observed in motor neurons and their surrounding glial cells in the spinal cord of ALS mouse models [90]. Patients with multiple sclerosis (MS) show APP up-regulation in both acute and chronic lesions [91]and APP expression has been suggested as a biomarker for disease progression [92]Aβ has also been implicated in microglial activation and associated neuroinflammation [93]. Furthermore, Aβ peptide injections decreases paralysis and spinal cord inflammation by suppressing activated lymphocytes in MS mouse model [94].

Moreover, Aβ deposits have been observed following traumatic brain injury (TBI) [62] as well as after spinal cord injury (SCI) [90,92,95] . Interestingly, researches show that inhibiting the activity of APP secretases and Aβ reduces recovery after SCI [96] reduces recovery after SCI in mouse. However, the mechanism of how spinal APP and Aβ involve in these processes are still not clear.

---

hAPP overexpression mouse model, PDGFB-APPJ20PSwInd , J20.

To investigate the effect of APP and Aβ on spinal cord, I used a human familial AD transgenic APP overexpression mouse model, PDGFB-APPJ20*PSwInd*, J20. These transgenic mice express a mutant form of the human amyloid protein precursor bearing both the Swedish (K670/M671L) and the Indiana (V717F) mutations (*APPSwInd*). Expression of the transgenic insert is directed by the human platelet-derived growth factor beta polypeptide

(PDGFB) promoter, which is expressed in pericytes, the precursor cells of glia and neurons. Researches show that hemizygotes express immunodetectable transgene products incerebral neurons, with the highest level of expression occurring in the neocortex and hippocampus. Enzyme-linked immunosorbent assay (ELISA) analysis reveals approximate total amyloid beta peptides and 42 amino acid length amyloid beta peptides in neocortical and hippocampal tissue from mutant mice. At five to seven months of age diffuse amyloid beta peptides deposition in the dendate gyrus and neocortex forms. Amyloid deposition is progressive with all transgenic mice exhibiting plaques by age eight to 10 months. Pups born of carrier females have shown an increased mortality rate in our colonies. Mucke et al. observed an approximately 15% mortality rate in the first 6 months of life of these J20 mice. Video-EEG monitoring of 4 to 7 month old hemizygous transgenic mice, N10+ on the C57BL/6J background, reveals hippocampal hyerexcitability and cortical and hippocampal spontaneous nonconvulsive seizures. The mice are immobile, with no myoclonic behavior observed, during the non-convulsive electroencephalographic seizures. Pentylenetetrazole induced seizures have earlier onset, are more severe and result in more frequent deaths (50% develop fatal status epilepticus) than wildtype controls. Further studies showed that the synaptic losses in hippocampus occurring in neocortex and hippocampus at three to four months of age. This mutant mouse strain has been proved to be a useful tool in many studies of the pathogenesis of Familial AD and possible therapeutic treatments.

While the cerebral degeneration and cognition defects in J20 mice have been intensively studied, the motor changes in J20 were never characterized before. In this study, the first aim is to investigate whether motor deficits also exist in J20 mice. A preliminary motor function test was performed in this study and only J20 mice demonstrated hind limb clasping but not

the WT mouse **(Figure 1-1)**, indicating that motor alterations occur in J20 mice when compared to WT littermates.

To further identify and characterize the motor changes in J20 mice, I studied the locomotion kinematics pattern changes of J20 and compare it with that of the WT.

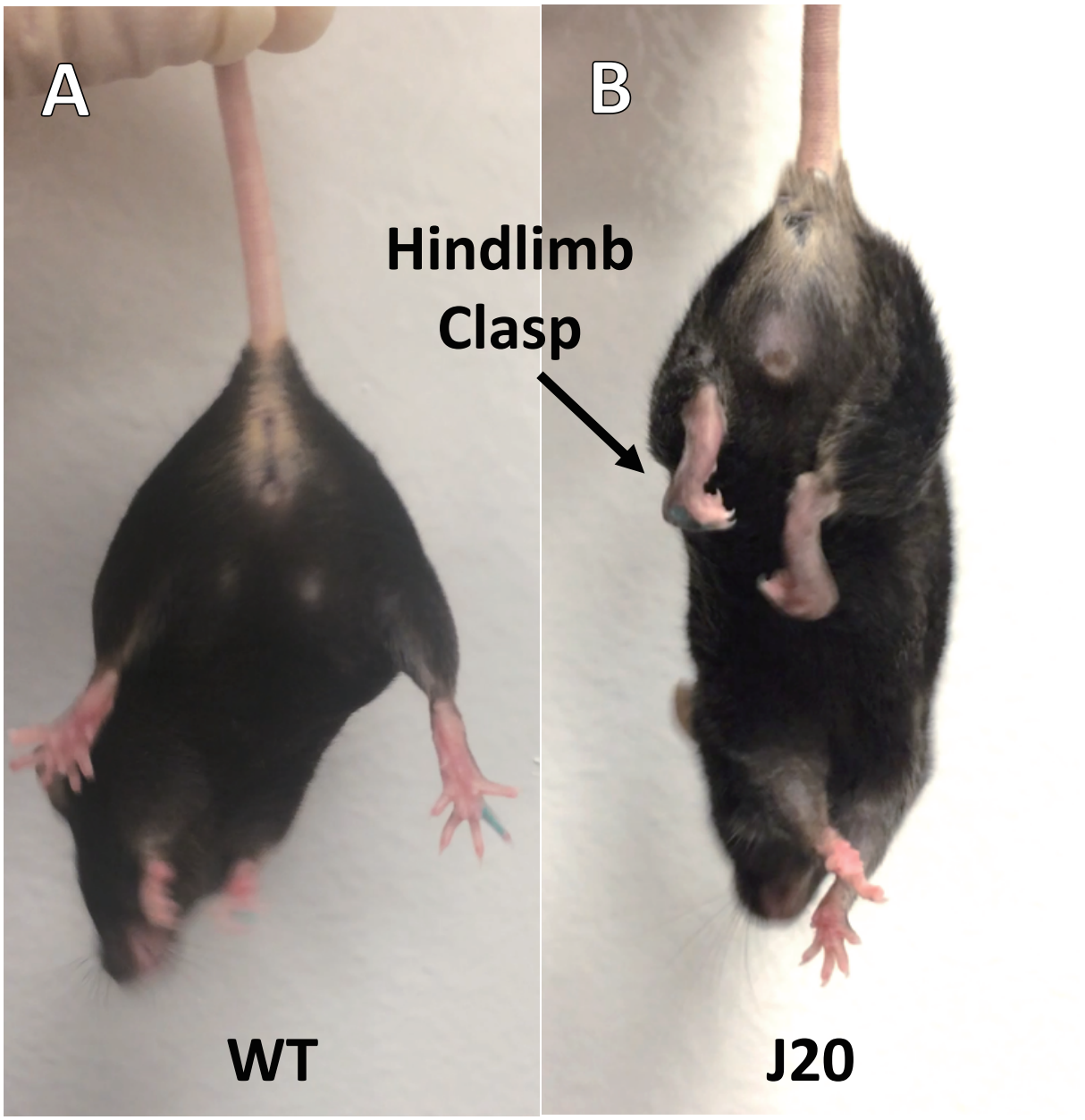

Figure 1- 3

Figure 1-3. Hindlimb clasp test showed significant motor changes in J20 mice (A) WT mice (n=28) spread out hindlimbs when they were hung by the tail while (B) hindlimb clasping were observed in J20 AD mice (n=36).

CHAPTER 2: Identify locomotion kinematics changes reflect Alzheimer's pathological in J20 mice changes using Support Vector Machine

INTRODUCTION

Motor function is not a unitary process, different motor abilities derive from the coordinated activity of various motor control systems located throughout the brain and spinal cord, and that extend via the peripheral nervous system to musculoskeletal structures[97–100]. Recent advances in imaging and neurophysiologic testing have begun to elucidate the complex processes necessary to ensure accurate movements. Integration of a wide range of sensory and visuospatial information is essential for accurate movements (i.e., postural control, spatial navigation and joint position) [101,102], and different motor-related brain regions may control distinct aspects of movements (i.e., speed versus balance) [103,104]. Finally, the increasing complexity and novelty of motor tasks demand increasing cognitive and sensory information processing for the accuracy of successful movements [103–105]. Consequently, motor impairment may derive from damage to the integrity of the sensorimotor related neural components [106,107], the connectivity and coordination among different neural components[108], or a combination of both types of damage [109–111]. As a result, the type of damage (i.e., loss of neuronal elements or accumulating pathology), and its location within CNS structures, may lead to different clinical motor deficits. These dissociations underscore that motor function is not a unitary process, and that several motor measures may be necessary to adequately assess neuropathological changes in patients.

Among a variety of motor measures, gait monitoring is crucial in patients with neuropathology (i.e., stroke, hemiplegia, ataxia, Parkinson, etc) [94,112–125]. Gait is a

complicated movement involves the coordination of multiple joints and usually with a usually stable pattern. Therefore, neuropathological changes at many level of the sensorimotor system will be reflected by the change of gait pattern [112,115,120,125]. Gait analysis is widely used for clinical evaluations and it is recognized as a central element in the quantitative evaluation of gait [125–127], diagnosis [128,129]and in the pre- versus post- intervention evaluations[130]. Furthermore, it is essential in spinal cord injured patients to monitor partial weight bearing [131,132] and also in older adults to predict potential falls[115,120].

Three-dimensional gait analysis has turned out to be a powerful tool for a quantitative assessment [112,114,121–125,133]. Several important features make gait analysis an ideal choice for the assessment of movements. It is non invasive, it allows one to repeat the examination several times within a short period of time, it provides quantitative and three-dimensional data as for kinematics (trajectories, velocity, accelerations, angles, etc.). Quantitative evaluation of motion represents a fundamental instrument in human subjects and experimental animal movement analysis. An accumulating body of research has shown that gait analysis provides highly informative data for evaluating selected specific gait parameters [94,123–127]. Moreover, the large volume of data produced by gait analysis makes it possible to quantitatively measure the patient's overall gait to understand the patient's condition. Different global indexes have been proposed in both for both human subjects and experimental animals, however these indexes have certain limitations. Some indexes are specifically designed for certain diseases, as Gillette Gait Index (GGI) and Gait Deviation Index (GDI) are specific for the overall gait evaluation in cerebral palsy children[111]. Several commercialized motion capture analysis software like Vicon and SIMI motion capture system provide built-in kinematics analysis besides data extraction but only compare no more than 10[118,134,135] kinematics features from three planes (sagittal, front and transverse

planes)[97,120,128,129]. These analyses described above are mainly applied in patients have severe morbidities and mortalities, with the cause well diagnosed. The gait analysis is currently applied in patients with cerebral palsy, spinal cord injury, stroke or with end stage diseases, in which the patient's/animal's gait is very significantly different from that of the normal one. There's more and more evidence indicate that gait changes can be important pre-clinical symptoms for different neuropathological conditions, like neurodegenerative disease (Alzheimer's Disease, Huntington Chorea, and Parkinson Disease) as well as for other chronic disease (i.e., chronic obstructive pulmonary disease) [108,136,137]. However, there's no quantitative gait analysis method in efficiently separating the gait pattern of healthy subjects or experimental animals from the diseased ones yet. This is probably because of three reasons:

1) The overall gait pattern in healthy subjects or experimental animals is not quantitatively characterized and measured;
2) Current gait analysis computational methods are not sensitive enough to recognize the pre-clinical changes in gait pattern;
3) The motor deficits caused by different neuropathological conditions don't always share the same features, it is difficult to use a same standard to quantitatively evaluate gait pattern with different pathological changes.

In this study we characterize gait kinematic patterns of J20 mice, a neurodegenerative disease model of Alzheimer's Disease in which the human amyloid precursor protein is overexpressed. Our aim is to determine a computational method to recognize unique gait kinematic features that will identify the transgenic mice from the WT mice and predict disease progression with kinematic data extracted by SIMI 2D/3D motion capture system. Because gait or kinematic data acquisition is usually performed through standardized

conditions (using treadmills, high-speed cameras motion captures and/or wearable sensors), the collected kinematics datasets are consistent among different clinical and animal research laboratories. Based on this, our algorithm has the potential to be applied to already collected datasets to characterize the early gait kinematics patterns unique for different neuropathological diseases.

MATERIALS AND METHODS

Animal Groups

All animal studies were performed according to protocols examined and approved by the Animal Use and Care Committee of University of California, Los Angeles. The J20 transgenic mouse line expresses a mutated human APP (hAPP: K670/M671L and V717F) under the control of the platelet-derived growth factor promoter (Mucke). In our studies, we have used a J20 mouse line crossed to a C57BL/6 background. In order to study the progression of the pathology, we further separate our animals by their age into 4 month (4mon) and 13 month (13mon) group. Because the cognitive deficits of the J20 animal start to be prominent after 5 month old, 4mon J20 mice are equivalent to pre-clinical phase animals. Our model dataset consists of thirty-one animals (4-month old, n=15; 13 month old, n=16) labeled as either WT or J20.

Quadrapedal treadmill stepping

Animals of all groups are tested according to protocols established in Edgerton lab [138]. In brief, treadmill stepping was measured utilizing video motion capture analysis tools. Retroreflective markers were placed on the wrist, shoulder, back, iliac crest, hip, knee, ankle, and foot bilaterally. Video was collected through the SIMI system while the mice stepped

quadrapedally on a treadmill. In order to obtain stable and representative gait pattern, the speed of the treadmill was increased by 3 cm/s once the animal was able to complete at least 10 consecutive steps. Speeds ranging from 3 to 30 cm/s (or until the mouse could not keep up with the treadmill) were tested. The 3D-coordinates (x, y, z) of all the tracked body parts under speed 6cm/s were extracted by SIMI 2/3D analysis software for further feature extraction.

Technical Approach

General kinematic analysis

In this study, there are two kinematic analysis methodology applied, general kinematic analysis and kinematic analysis using SVM. The general kinematic analysis determines the maximum speed the animal is capable of running and the number of steps with drag. The step with drag is defined as incidence of toe drags at toe-off during initiation of the swing phase of step. General kinematics analysis was done blindly to the animal's genotype.

The general kinematic analysis showed the difference of maximum speed and drag step number between J20 and WT (**Fig. 2-1**). The maximum speeds J20 mice could run on treadmill were significantly lower than their WT littermates in both 4mon and 13mon group (**Fig. 2-1A**). Moreover, the maximum speeds of the 4mon WT mice were also faster than 13mon WT mice but there was no significant difference between 4mon and 13mon J20 mice maximum speeds. Because all the animals could run at the speed of 6cm/s (Indicated by the grey line in **Fig. 2-1A**), the number of drag steps among 10 tracked treadmill steps was counted for all the animals. Steps with drag are more frequently observed in J20 but not WT mice in both 4mon and 13mon groups (**Fig. 2-1B**).

These results indicate that measuring the maximum speed the animals could run as well as the drag steps number can finely separate the J20 and WT quadrupedal treadmill stepping kinematics pattern. However, these general kinematics analyses cannot separate the patterns of J20 animals from different age groups. Furthermore, forcing the animals to run at their limit can cause potential stress and danger to the tested subjects (e.g., animals couldn't follow the treadmill speed often fell off the treadmill). These limitations of the general kinematic analysis compromise the method being translated to clinical testing for neurodegenerative or other diseased human subjects. Thus, we tested the kinematics analysis method with SVM, which studies the movement and coordination of multiple body parts at 6cm/s treadmill locomotion. We aim to use this method to discover the pathological changes in J20 mice and reveal further information on joint and muscle synergies which contribute to lower maximum speed and more drag steps observed in J20 mice.

Experimental procedure of kinematic analysis with SVM

Figure 2-2 illustrates the procedure to extract and select the features, which separated WT from J20 animals with the maximum accuracy, and then establish the prediction algorithm to predict the maximum speed the animal could run. In brief, after putting the animal on the treadmill, we captured extract our desired features through SIMI 2D/3D motion capture system (The feature extraction algorithms will be explained comprehensively in the ***Feature Selection*** Section). The features were separated into two types:

1) Trajectory, which focused on the individual body part kinematics (Features listed in **Table.2-1**);

2) Angle, which involved more body parts synergy information (e.g., the angle change of ankle suggested the synergy among foot, ankle and leg/knee, **Table.2-2**).

Our aim was to classify the animals into different genotype background (WT versus J20) and different age groups (4mon and 13mon) based upon the locomotion kinematic coordinates of each listed body part (**Fig. 2-2** Body Part Block). In this study, The Trajectory and Angle features collected from the left and right side are pooled together. Hence, we focused on identifying features that best represent and classify the kinematics of each individual body part. For each body part, we proceeded with Trajectory and Angle features leading to subsets of features that will maximally classify each feature. We chose one of the body parts and proceed with the Trajectory and Angle features in the selected body part. After the procession, the features subsets that lead to the maximum classification were recognized. Furthermore, because ten consecutive steps were tracked for each animal on the treadmill we also selected the optimal combination of the step (s^*) and the subset of features (f^*) leading to the maximum classification accuracy. Thus, we trained the SVM classifier using the different combinations of the step and the subset of features and then evaluated the accuracy score of the combination using the leave-one-out cross validation method. By applying the leave-one-out cross validation method, we selected one step from the N^{th}-element step set (s^N) and the $m^{th}(m \leq M)$-element combination of the features from the M^{th}-element feature set (f^M) each time. With the selected s^N and f^M, we constructed the input data while each row of this input dataset represents one animal's kinematics sample. With this input sample set, we set aside one sample for as the validation sample and train the SVM classifier with the remaining samples. Finally, the classification accuracy was computed for the testing sample. We repeated the same procedure on all ways to cut the original input sample set on a validation set of 1 sample and a training set until we exhausted our input sample set. The average classification accuracy of each input samples (each tested animal) was reported as the classification accuracy for this specific choice of step and features. In this manner, we achieved the optimal step and feature subset combination (Fig.2-2, Optimal Feature/Step

Selection). Finally, the output is the maximum accuracy that is a function of the optimal step and the optimal subset of features. We adopted the exhaustive search to choose the optimal subset of features which requires running $\sum_{m=1}^{m=M} \mathbf{(M\ m)=2^M-1}$ times, for each choice of step and body part. Therefore, with κ number of body parts, **N** number of steps and **M** number of features, the total running time of the proposed method is $\boldsymbol{O(\kappa\ X\ N\ X\ (2^M-1))}$.

Feature Extraction

Locomotion is a repetitious sequence of limb motions to simultaneously move the body forward while also maintaining stance stability. In this study, we extracted the features of at least 10 consecutive steps. The pre-selected features have been proven to be crucial for assessing the different movements necessary for locomotion by other researchers[139]. The capability of moving, keep limbs coordination and stance stability by other locomotion/gait analysis researches.

For locomotion, there are three important functional criteria for locomotion quality evaluation: the gait cycle execution of each individual body part, the synergies among different body parts, and the stability of the locomotion execution. Hence, two types of features analyses were set in this study:

1) The features related to trajectory of each gait cycle for individual tracked body parts (**Fig. 2-3 B1-2, C1-2, E1-2, F1-2**), reflecting the execution of body parts in gait cycles;

2) The features related to angle changes, reflecting the synergies among at least three body parts (**Fig. 2-3 A, D**). The stability of the locomotion patterns was reflected by the deviation for each analyzed feature of both Angles and Trajectory Analysis.

1) Trajectory analysis: To analyze the movement execution of each individual body part in the tracked gait cycles, we focused on the features related to body part movement trajectory. The following trajectory features were analyzed for every tracked step of

individual body parts respectively:

- Step Length: The maximum distance of the animal along x-axis:

$$sl^i_{BP} = \max_{1\leq j\leq n}(x^i_{j,BP}) - \min_{1\leq j\leq N}(x^i_{j,BP}) \quad (1)$$

- Step Height: The maximum distance of the animal along y-axis:

$$sh^i_{BP} = \max_{1\leq j\leq n}(y^i_{j,BP}) - \min_{1\leq j\leq N}(y^i_{j,BP}) \quad (2)$$

- Length/Height Ratio: The ratio between Step Length and Step Height:

$$\rho^i_{BP} = \frac{sl^i_{BP}}{sh^i_{BP}} \quad (3)$$

- Trajectory Path: The length that the animal passes within one step:

$$L^i_{BP} = \sum_{j=1}^{N} l^i_{j,BP} \quad (4)$$

- Step Speed: Th length that the animals passes for each of its sample within one step:

$$v^i_{BP} = \frac{L^i_{BP}}{N} \quad (5)$$

For all the equations listed above, x^i_{BP} and y^i_{BP} indicate the maximum distance in which the animal can take in x-coordinate and y-coordinate, respectively. Lij,BP is the distance the animal pass from j^{th} to $(j+1)^{th}$ sample while being at ith step and we are looking at its body part (BP). An example for Foot trajectory feature extraction with the x and y coordinates of each sample point (800 sample points were collected for each gait cycle) is shown in **Fig. 2-4**. The same calculation were applied to all nine tracked body parts, Foot, Ankle, Knee, Hip, Iliac Crest, Back, Shoulder, Elbow and Wrist for each body side. These trajectory features are summarized in **Table. 2-1**.

2) Angle analysis: In this analysis, the angles between the body parts of the animal as were used as features. Note, the **Ankle**, **Knee**, **Hip**, **Iliac Crest**, **Back**, **Shoulder** and **Elbow** angles were calculated bilaterally. Among these 9 denoted body parts, the angles of **Iliac**

Crest and **Back** were set as internal control for the angles since these joints are defined as part of the passenger unit because they are carried and do not directly contribute to the act of locomotion while the other 5 body parts belong to the locomotive unit. Thus the angles of 5 body parts (**Ankle**, **Knee**, **Hip**, **Elbow** and **Shoulder**) were analyzed for the following features. For each gait cycle, 800 samples per cycle were captured as summarized in **Table. 2-2**.

$\theta^i_{j,BP}$ represents the angle for the body part (BP) where the animal is in its jth step and we capture the jth sample. For example, in **Fig. 2-4**, BP=**Ankle**. Rij,BP denotes the rate of the change in the angle while the animal passing from the jth sample to (j+1)th. $r^i_{j,BP}$ is defined as:

$$r^i_{j,BP} = \frac{(\theta^i_{j+1,BP} - \theta^i_{j,BP})}{\Delta^i_{j,BP}} \qquad (6)$$

where Δij,BP is the time difference the jth and (j+1)th steps:

$$\Delta^i_{j,BP} = t^i_{j+1,BP} - t^i_{j,BP}$$

With these definitions, we will define our features as following while the animal is in its ith step on the treadmill:

- Maximum Angle ($\theta^i_{max,BP}$): The maximum angle of the animal:

$$\theta^i_{max,BP} = \max_{1 \le j \le N} \theta^i_{j,BP} \qquad (7)$$

- Minimum Angle ($\theta^i_{min,BP}$): The minimum angle of the animal:

$$\theta^i_{min,BP} = \min_{1 \le j \le N} \theta^i_{j,BP} \tag{8}$$

- Angle Average ($\theta^i_{min,BP}$): The average angle of the animal:

$$\theta^i_{avg,BP} = \frac{\sum_{j=1}^{N} \theta^i_{j,BP}}{N} \tag{9}$$

- Angle Standard Deviation: The standard deviation angle of the animal: ($\theta^i_{min,BP}$):

$$\theta^i_{std,BP} = \frac{\sum_{j=1}^{N} (\theta^i_{j,BP} - \theta^i_{avg,BP})}{N} \tag{10}$$

- Maximum Rate ($r^i_{max,BP}$): The maximum rate of the animal:

$$r^i_{max,BP} = \max_{1 \le j \le N} r^i_{j,BP} \tag{11}$$

- Minimum Rate ($r^i_{min,BP}$): The minimum angle of the animal:

$$r^i_{min,BP} = \min_{1 \le j \le N} r^i_{j,BP} \tag{12}$$

- Rate Average ($\theta^i_{min,BP}$): The average rate of the animal:

$$r^i_{avg,BP} = \frac{\sum_{j=1}^{N} r^i_{j,BP}}{N} \tag{13}$$

- Rate Standard Deviation ($r^i_{min,BP}$): The rate standard deviation of the animal:

$$r^i_{std,BP} = \frac{\sum_{j=1}^{N} (r^i_{j,BP} - r^i_{avg,BP})}{N} \tag{14}$$

These angle features are summarized in **Table. 2-2**.

RESULTS

The Trajectory Analysis showed the Step Height (sh) and Trajectory Line Speed (v) of bilateral Knees generated the highest maximum classification accuracy for separate J20 and WT Trajectory pattern.

As shown in **Table.2-3**, the maximum classification accuracy for Trajectory analysis was **80.65%.** This was achieved by sub-setting the optimal features of bilateral **Knee**, Step height (sh), and Step Trajectory Line Speed (v), from the $3rd$ step. The mean within one standard deviation of the optimal Knee Trajectory feature subset was shown in the supplementary data (**Supplementary Table. 2-1**) and there was no significant difference detected between the Knee (sh, v) of model classified animal groups and that of the actual animal genotype groups (**Supplementary Fig. 2-1**). For Knee (sh, v), 6 out of 31 entered samples were misclassified (80.65% classification accuracy). As shown in **Table.2-4** (Column "Trajectory Analysis Prediction"), all 6 misclassified samples were WT but classified into J20 group: 3 4mon WT samples (#17, #18, #22) and 3 13mon WT samples (#5, #9, #10) were misclassified as J20. While the Knee(sh, v) feature subset separating the J20 samples from the WT ones through SVM, the Knee sh (Step Height) and v (Step Trajectory Line Speed) of J20 samples showed no significant difference but only trends of decreasing compared to these of WT samples when these two features were analyzed separately (**Supplementary Fig. 2-1**). A further analysis showed that although Knee(sh, v) classified animals by genotype, this optimal trajectory feature subset could not effectively separate age groups within a genotype , especially the 4mon J20 and 13mon WT (**Supplementary Fig. 2-2**).

The Angle Analysis showed the Maximum Angle (θ_{max}), Angle Standard Deviation (θ_{std}), Angle Change Rate Maximum (r_{max}), and Angle Change Rate Average (r_{avg}) of Hip generated the highest maximum classification accuracy for separate J20 and WT Angle kinematics pattern.

Angle analysis performed better than Trajectory analysis by increasing the classification accuracy from **80.65%** to **87.10%**. This accuracy is achieved by Hip as the body part, step 2 as the optimal step and the combination of **(θ_{max} , θ_{std}, r_{max}, r_{avg})** as the optimal feature subset (**Table. 2-4**). The mean within one standard deviation of the optimal Hip Angle feature subset was shown in the supplementary data (**Supplementary Table. 2-2**) and there was no significant difference detected between the Hip (θ_{max} , θ_{std}, r_{max}, r_{avg}) of SVM estimated animal groups and that of the actual animal genotype groups (**Supplementary Fig. 2-3**). 4 out of 31 entered samples were misclassified (87.10% classification accuracy). As shown in **Table.2-5** (Column "Angle Analysis Prediction"), all 4 misclassified samples were J20 but classified into WT group: 3 4mon J20 samples (#15, #30, #31) and 1 13mon J20 samples (#3) were misclassified as WT. Similar to the Trajectory Analysis results, the further analysis of WT and J20 samples Hip (θ_{max} , θ_{std}, r_{max}, r_{avg}) showed that when being analyzed separately, none of the four features demonstrated significant difference between J20 and WT groups. Trends of increasing was observed in the θ_{std} (Hip Angle Standard Deviation) of 4mon J20 samples and the r_{max} (Angle Change Rate Maximum) (**Supplementary Fig. 2-3**). Notably, the Hip (θ_{max} , θ_{std}, r_{max}, r_{avg}) angle feature subset not only separate J20 and WT classes, but also performed better in separating J20 and WT samples from different age groups (**Supplementary Fig. 2-4**).

Angle Analysis reached the maximum classification between J20 and WT in our dataset.

The classification results from the Trajectory and Angle analyses were not completely the

same. In order to determine the final classes of the entered samples, we ran another round of SVM with the classes determined by the previous Trajectory and Angle analyses as two independent features (**Fig. 2-5**). The final classes were shown in the last column of **Table. 2-5** and the final classes were exactly the same as the classification result from the Angle analysis. This result means Angle analysis has achieved the maximum classification between J20 and WT in our dataset. The classification result also shows that the Trajectory Analysis generates higher False Positive results (classifying WT samples into J20) while the Angle Analysis generates higher False Negative results (classifying J20 samples into WT). These results suggest that the kinematics trajectory pattern is sensitive to other factors besides the pathological influences of APP overexpression in the J20 mice while the angle-changing pattern detects the changes in J20 samples more strictly.

Feature subsets of six body parts classified J20 from WT kinematics pattern with accuracies higher than 75%

Knee generated the optimal trajectory (**80.65%** maximum classification accuracy) and **Hip** generated the optimal angle feature subsets (**87.10%** maximum classification accuracy). Our analyses show that the kinematics of other body parts are also altered in J20 mice and these feature subsets enable classification of J20 kinematics pattern from the WT, but with relatively lower accuracy rates. The second highest trajectory maximum classification accuracy was **77.42%** from the **Shoulder** and **Iliac Crest (Table. 2-3)**. The **Ankle** generated the second best angle classification accuracy **83.87%**, followed by the Elbow feature subset with a classification accuracy of **80.65% (Table. 2-4)**. The feature subsets of body parts that generate the classification accuracy higher than **75%** are shown in **Table. 2-6**. The Angle Change Rate Average (r_{avg}) is the angle feature that was detected most frequently: the r_{avg} is among the three body parts (**Hip**, **Ankle** and **Elbow**) that

generated the top three Angle Analysis classification accuracies. This indicates that the r_{avg} of these three body parts are mostly changed in the J20 mice when compared to WT ones. Although no significant difference were detected in r_{avg} of these three body parts between WT and J20, a decreasing trend was observed in all three body parts, indicating a trend of slowing down in hip, ankle and elbow joint angle movement rates.

Because the joint angle movement reflects the coordination of three body parts (as shown in **Fig. 2-4**, feature definition), angle change differences of the joint could suggest trajectory change differences of its two adjacent body parts. As expected, the three body parts that generated the top classification accuracy rates are the adjacent body parts for **Hip**, **Ankle** and **Elbow** (**Knee**, **Iliac Crest**, **Shoulder**). **Knee** is the adjacent joint of **Ankle**, **Illiac Crest** and **Knee** are the two adjacent joint of **Hip** while **Shoulder** is the adjacent joint of **Elbow**. Interestingly, although wrist and foot are both extremities of upper and lower limbs as well as the adjacent parts for **Elbow** and **Ankle** respectively, both body parts could not generate high classification accuracy to separate the J20 and WT kinematics patterns. This suggested that **Foot** and **Wrist** trajectory changes detected in our dataset are not specific to J20 mice, while **Shoulder**, **Iliac Crest** and **Knee** trajectory feature subsets, as well as **Elbow**, **Hip** and **Ankle** angle feature subsets showed higher specificities in characterizing the J20 kinematics pattern.

The Trajectory and Angle Analysis results suggested Posture changes in J20 mice

Notably, the two passenger unit body parts, **Back** and **Iliac Crest** exhibited different patterns in the Trajectory Analysis. The trajectory feature subset of the **Back** did not generate a classification accuracy rate higher than 75% (as shown in **Table.2-3**, the classification accuracy of **Back**(*sl, L*) is 70.97%). The optimal feature subset of ***Iliac Crest*** (**Table. 2-3**, the classification accuracy of **Illiac Crest** (*L*) is 77.42%), indicating that the

Illiac Crest trajectory pattern change separate J20 and WT mice. This result also indicates that the upper extremity trajectory pattern changes is more specific to J20 mice compared to the lower extremity trajectory pattern, since Back is the passenger unit for the upper extremity while **Illiac Crest** is the passenger unit of the lower extremity.

The Angle Analysis results further supported this observation in the Trajectory Analysis. The top two classification accuracies are both from body parts of the lower extremity (**Table. 2-4**, **Hip** (θ_{std}, θ_{max}, r_{max}, r_{avg}) generates 87.1% classification accuracy and **Ankle** (θ_{std}, θ_{max}, r_{max}, r_{avg}) generates 83.87% classification accuracy). Furthermore, θ_{std} is the angle feature only detected in **Hip** and **Ankle** but not in any other body parts (Angle feature occurrence frequency is shown in **Supplementary Table. 2-4**, and Trajectory feature occurrence frequency is shown in **Supplementary Table. 2-3**), which indicates the stability of **Hip** and **Ankle** angles are most significantly affected in J20 mice. Furthermore, a trend of **Hip** θ_{max} increase together with a trend of **Elbow** θ_{min} decrease are observed in J20 mice (**Supplementary Fig. 2-4**), suggesting a potential trunk and pelvis alignment alteration. The further analysis of **Illiac Crest** and **Back** angle showed that a 2.5 degree trunk and pelvis alteration in J20 mice compared to WT ones (**Fig. 2-6**).

DISCUSSION

Locomotion kinematics pattern can be affected by deficits at multiple levels: muscle, neuromuscular connection, peripheral nerve conductance, spinal cord circuitry control, supraspinal motor control as well as cognition. This makes locomotion kinematics pattern alteration a common symptom of many different diseases. And because of its multi-level regulation nature, the locomotion pattern changes are usually one of the early symptoms of diseases. However, the lack of high-resolution kinematics data analytic methods and the

understanding of the underlying cause as well as the mechanism of specific kinematic pattern alteration, locomotion kinematics analysis cannot provide accurate diagnostic information.

The limitation of current locomotion kinematics analytics methods was also observed in this study. When using the General kinematics analysis, we were able to classify animals into J20 and WT by observing the drag step number at 6*cm/s* and the highest speed the animal could run on the treadmill but could not further classify the animals by their age groups. Moreover, to obtain the highest speed, we had to force the animals to reach their running limitations, which could cause stress and potential danger to the subjects. The kinematics of four extremities (bilateral wrist and foot) of the animal also only showed the trend of kinematics changes in J20 mice compared to WT, but the changes were not significant (**Supplementary Fig. 2-1**).

However, with our SVM based kinematics analysis, we identified body parts with the most changes in J20 as well as their mostly affected kinematics features subset compared to their WT control littermates. With this SVM based locomotion kinematics analysis we recognized several J20 specific kinematics pattern changes, which were not detected by General kinematics analysis. These J20 specific kinematics pattern changes include the slower angle speed changes of **Elbow**, **Hip**, and **Ankle**, the trajectory line speed decrease in **Knee** and **Shoulder**, the instability in joint angle change control of **Hip** and **Ankle** as well as a 2.5 degree trunk and pelvis axis alteration when compared to WT littermates. Moreover, our analysis shows that lower extremity changes are more specific for the J20 kinematics pattern while fewer upper extremity changes are specific to J20 animals.

With the SVM kinematics analysis method from this study, the final classification accuracy rate is 87.10% with a false negative rate of 13.9% (4 out of 31 entries). A further

analysis for the kinematics of these four samples (#3, #15, #30, #31) showed that these 4 animals have different left and right kinematics patterns (Results not shown). Because our current model is based on the assumption that the kinematics patterns from left and right sides of the body have no significant difference, we pooled the kinematics data from bilateral body parts together. This treatment averages the trajectory and angle feature values from left and right sides of the tested animal, that failed to detect the left and right kinematics pattern differences in animal #3, #15, #30, and #31. We ran our SVM based model with kinematics features from different sides of the body separately but unfortunately the entry number is not large enough for effective SVM analysis. We aim to collect more kinematics data to test our model with features from left and right side of the body run separately. Notably, the final classification result is exactly the same as the Angle Analysis result, which means the Angle Analysis only generate false negative result with our current dataset. Interestingly, just contrary to the Angle Analysis, the Trajectory Analysis only generated false positive result with current dataset. This suggests the Trajectory Analysis can be easily affected by changes of left and right incoordination while our current Angle Analysis is more specific to most J20 kinematics pattern changes except left and right limb kinematic pattern differences.

CONCLUSION

By establishing this SVM based kinematics analysis method, we characterized the specific kinematics pattern changes of J20 mice. With SVM Angles and Trajectory Analysis, this analysis method classifies the quadurapedal kinematics pattern for J20 and WT from different age groups (4mon and 13mon).

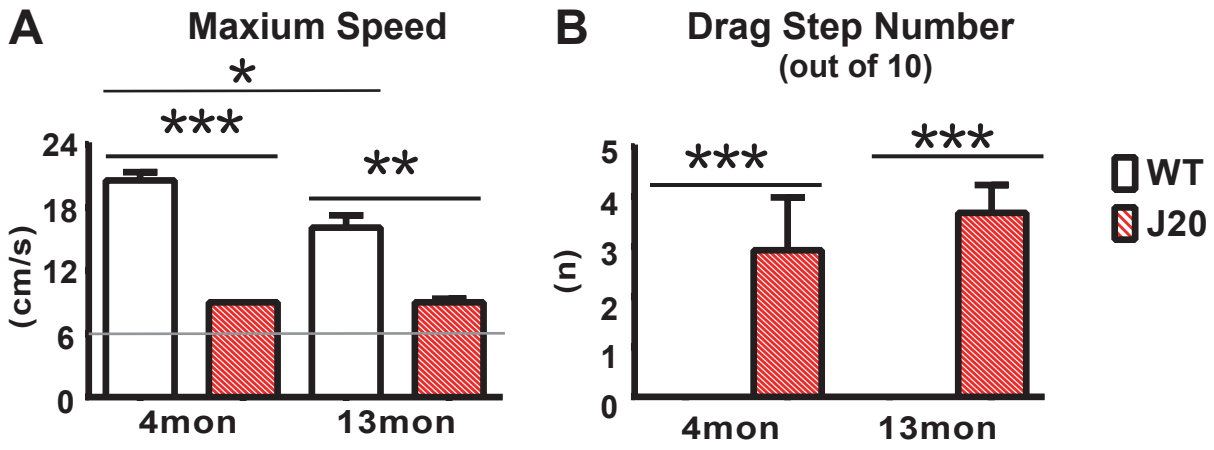

Figure 2- 1

Figure 2-1. The general kinematics analysis showed the maximum speed the animals can run and the drag step number among the tracked 10 steps were features separate J20 and WT treadmill step patterns. (A) The average of the maximum speed that the WT animal can run on treadmill were significantly higher than that of the J20 animal in both 4mon and 13mon. The maximum speed of the 4mon mice is slightly higher than that of the 13mon mice while no significant difference detected in J20 4mon and 13mon group. The gray line indicates all the tested animal can run at treadmill speed 6cm/s. (B) Among the 10

tracked consecutive steps, steps with drag were observed in both 4mon and 13mon J20 mice. Treadmill speed the mice stepped was 6cm/s, 31 animals in total (4mon WT, n=7; 4mon J20, n=8; 13mon WT, n=8; 13mon J20, n=8) were tested. *, p<0.05, **, p<0.01; ***, p<0.005.

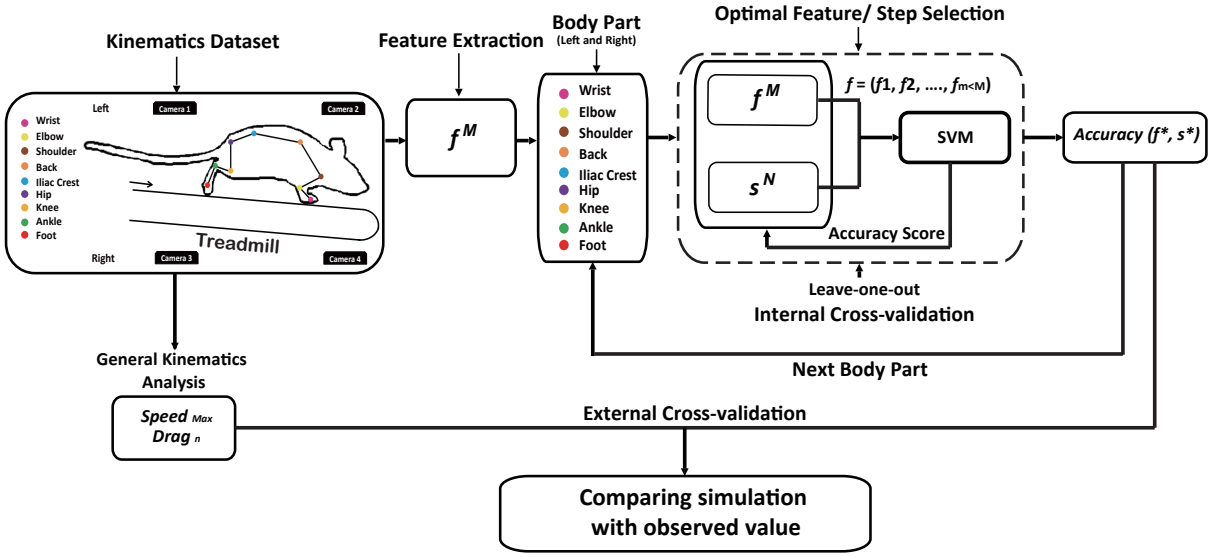

Figure 2- 2

Figure 2-2. The flow chart of SVM based kinematics analysis procedure. The whole procedure was divided into five modules: **1) Kinematics Dataset collection**: 9 body parts (indicated by different colors) were bilaterally marked by reflective tapes for all the tested animals and their movements were captured by high frequency cameras. The SIMI motion captured system analysis the videos and calculated the 3D coordinates for each body part and establish the kinematics dataset. **2) General Kinematics Analysis:** the maximum speed the animal could run on treadmill and the drag step number out of 10 tracked consecutive steps were counted and saved as an external validation standard. **3) Feature Extraction:** two types of features, Angles and Trajectories were calculated by their definition previously given by other published literatures (More detailed information is in the Section ***Feature Extraction***).

4) Optimal Feature/ Step Selection: the optimal feature and the optimal step pair among the 10 tracked steps of each individual body part were selected by SVM to generate the maximum accuracy function in classifying the J20 and WT kinematics patterns. The accuracy function was further validated through Leave-one-out Internal Cross-validation. **5) External Cross-validation.** The optimal feature/step based accuracy function was further validated through a correlation analysis with the observations from **General Kinematics Analysis** (Maximum Speed and drag step) to confirm the SVM output.

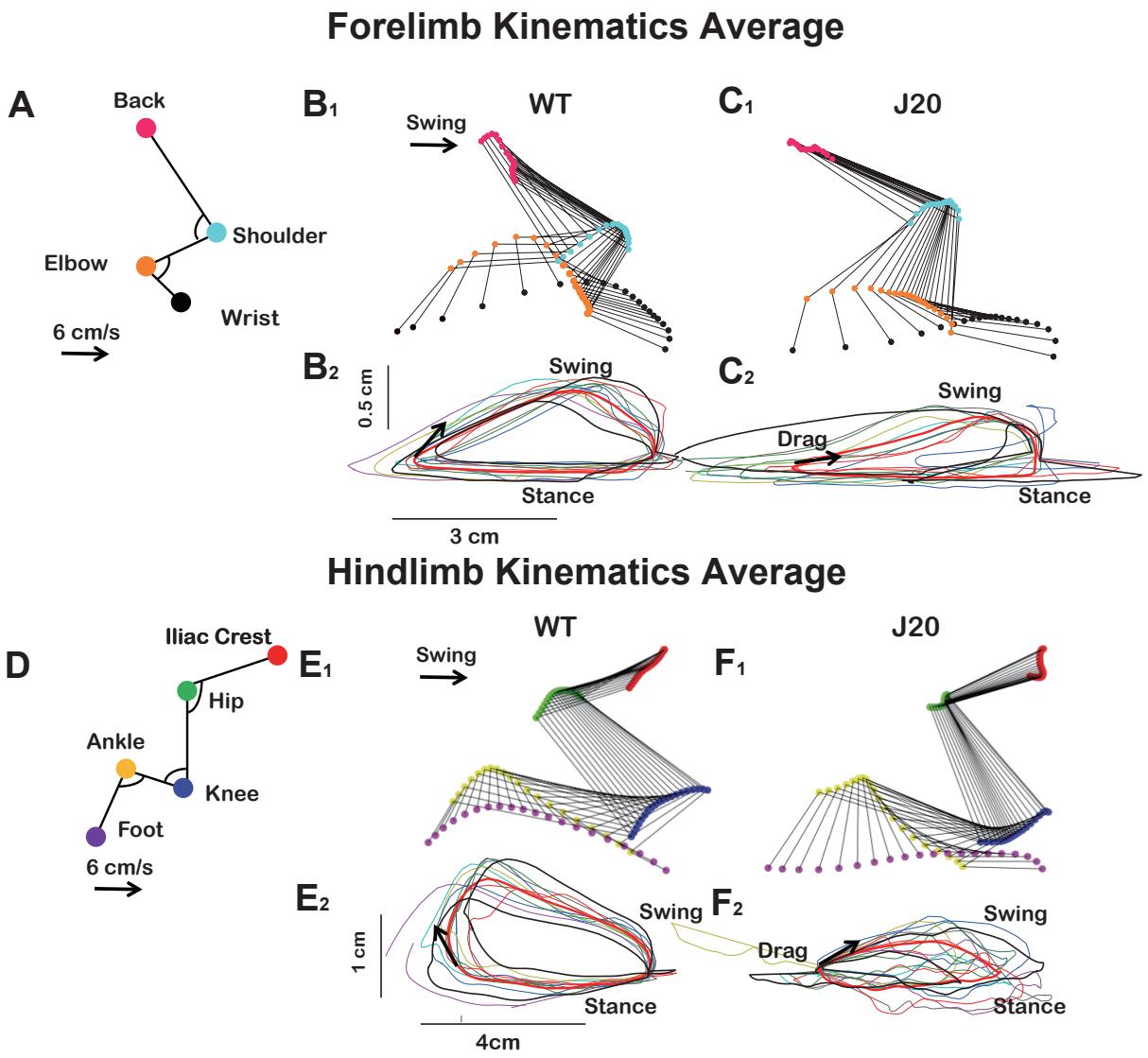

Figure 2- 3

Figure 2-3. The illustration of the Angles and Trajectory features for forelimb and hindlimb kinematics. For the forelimbs (A, $B_{1\text{-}2}$, $C_{1\text{-}2}$), the features related with angle changes of shoulder and elbow were calculated (A), while the features related with the movement trajectory were tracked for both WT (B_1, C_1) and J20 mice (B_2, C_2). And for the hindlimbs (D, $E_{1\text{-}2}$, $F_{1\text{-}2}$), the features related with angle changes of hip, knee and ankle were calculated (D), while the features related with the movement trajectory were tracked for both WT (E_1, F_1) and J20 mice (F_2, F_2). Hence, there were 5 body parts analyzed for features of

the Angles (shoulder, elbow, hip, knee and ankle) and 9 body parts analyzed for features of the Trajectories for each side.

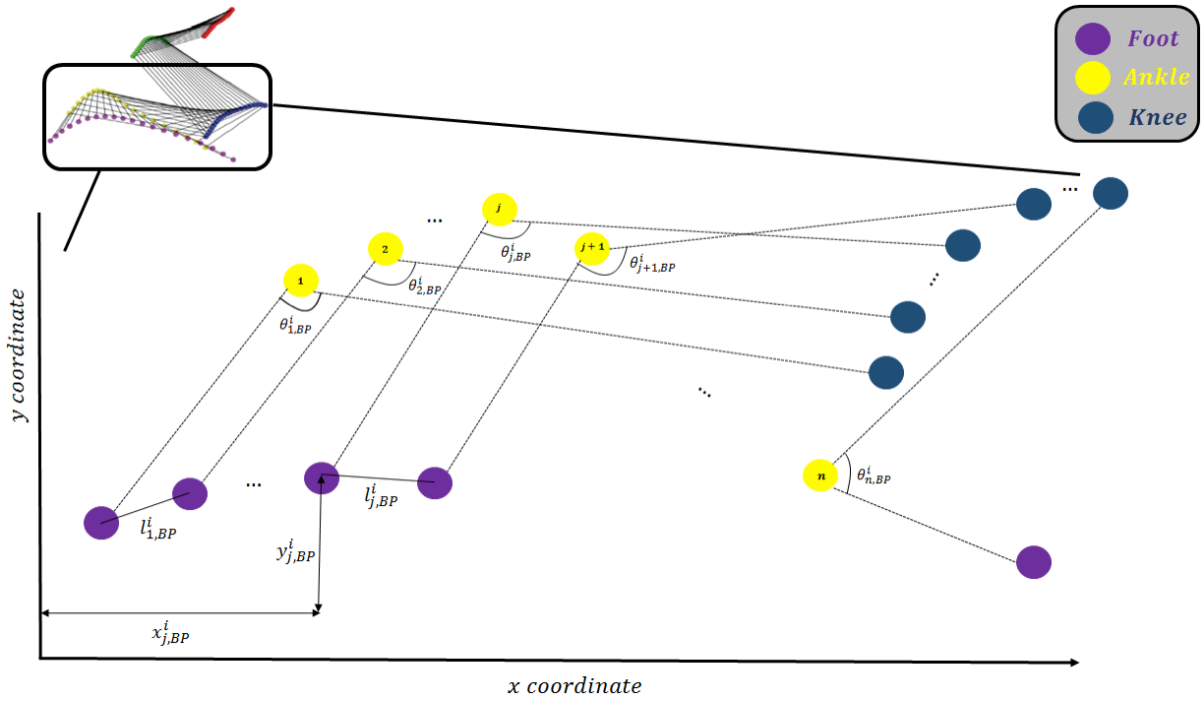

Figure 2- 4

Figure 2-4. The illustration of Angle and Trajectory analysis for Ankle and Foot. For each gait cycle, the x and y coordinates of 800 sample points were collected to calculate the $l^i_{j,BP}$ for calculate Trajectory path length ($l_{j,BP}$) and Average time velocity, $x^i_{j,BP}$ for Step Length, $y^i_{j,BP}$ for calculate Step Height, and both for Length/Height Ratio (ρ^i_{BP}), which the detailed equation information is listed in **Table. 1.** Meanwhile, the elements $\theta^i_{j,BP}$ for Angle Analysis were also extracted. i indicates the number of step out of the 10 tracked steps ($1 \leq i \leq 10$), while j indicates the number of sample point out of 800 samples extracted from each step cycle for step i ($1 \leq j \leq 800$)

List of features used in Trajectory Analysis		
Feature name	Symbol	Feature definition
Step Length	sl^i_{BP}	$\max_{1\leq j\leq N}(x^i_{j,BP}) - \min_{1\leq j\leq N}(x^i_{j,BP})$
Step Height	sh^i_{BP}	$\max_{1\leq j\leq N}(y^i_{j,BP}) - \min_{1\leq j\leq N}(y^i_{j,BP})$
Length/Height Ratio	ρ^i_{BP}	sl^i_{BP}/sh^i_{BP}
Trajectory path	L^i_{BP}	$\sum_{j=1}^{N} l^i_{j,BP}$
Average time velocity	v^i_{BP}	$\frac{L^i_{BP}}{N}$

Table 2- 1

Table 2-1. The summary table of features extracted for the Trajectory analysis. These features were extracted and analyzed for 9 body parts (All the body parts in the Body part block, **Fig 2-2**)

List of features used in Angle Analysis		
Feature name	Symbol	Feature definition
Maximum Angle	$\theta^i_{max,BP}$	$\theta^i_{max,BP} = \max_{1\leq j\leq N} \theta^i_{j,BP}$
Minimum Angle	$\theta^i_{min,BP}$	$\theta^i_{min,BP} = \min_{1\leq j\leq N} \theta^i_{j,BP}$
Angle Average	$\theta^i_{avg,BP}$	$\theta^i_{avg,BP} = \frac{\sum_{j=1}^{N} \theta^i_{j,BP}}{N}$
Angle Standard Deviation	$\theta^i_{std,BP}$	$\theta^i_{std,BP} = \frac{\sum_{j=1}^{N} (\theta^i_{j,BP} - \theta^i_{avg,BP})}{N}$
Maximum Rate	$r^i_{max,BP}$	$r^i_{max,BP} = \max_{1\leq i\leq N} r^i_{BP}$
Minimum Rate	$r^i_{min,BP}$	$r^i_{min,BP} = \min_{1\leq j\leq N} r^i_{j,BP}$
Rate Average	$r^i_{avg,BP}$	$r^i_{avg,BP} = \frac{\sum_{j=1}^{N} r^i_{j,BP}}{N}$
Rate Standard Deviation	$r^i_{std,BP}$	$r^i_{std,BP} = \frac{\sum_{j=1}^{N} (r^i_{j,BP} - r^i_{avg,BP})}{N}$

Table 2- 2

Table 2-2. The summary table of features extracted for the Angle analysis. These features were extracted and analyzed for 5 body parts (All the body parts in the Body part block, Fig 2-2, except for wrist, foot, and 2 fixed body parts, **Back** and **Iliac Crest**).

Percentage of Classification Accuracy from Trajectory Analysis			
Body Part	**Optimal Step** *(s*)*	**Optimal Feature Subset** *(f*)*	**Accuracy %** *(s*, f*)*
Wrist	3	*sl, ρ*	74.19
Elbow	10	*sl, L*	74.19
Shoulder	1	*sh, ρ, L, v*	77.42
Back	10	*sl, L*	70.97
Iliac Crest	7	*L*	77.42
Hip	7	*sl, sh, ρ, L*	70.97
Knee	4	*sh, v*	80.65
Ankle	3	*sl, sh, v*	74.19
Foot	0	*sh, L, v*	70.97

Table 2- 3

Table 2-3. The optimal Feature and Step for the maximum classification accuracy from Trajectory Analysis. The **Knee** Step Height and Trajectory Line Speed combination generated the highest classification accuracy of 80.65% (highlighted in yellow), while the second highest classification accuracy of 77.42% (highlighted in blue) was generated from the bilateral **Shoulder** and **Iliac Crest** to separate J20 and WT kinematics patterns.

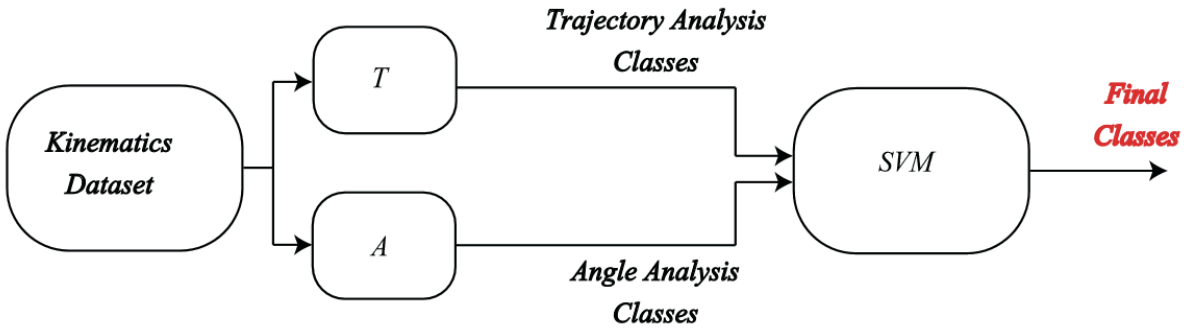

Figure 2- 5

Figure 2-5. Final classes obtained by injecting the classes determined by Trajectory and Angle Analyses as two features and apply support vector machine to distinguish between J20 and WT animals. Each of T and A are one classifier module shown in Figure 2, where in Trajectory Analysis we uses the kinematics features from all of the nine body parts and in Angle Analysis we used the features from 5 body pars which are locomotor unit joints.

Percentage of Classification Accuracy from Angle Analysis			
Body Part	**Optimal Step** *(s*)*	**Optimal Feature Subset** *(f*)*	**Accuracy %** *(s*, f*)*
Elbow	3	*θmin, r'min, r'avg*	80.65
Shoulder	1	*θmax, θmin, θavg, r'max, r'min*	74.19
Hip	2	*θmax, θstd, r'max, r'avg*	87.10
Knee	5	*θmin, r'min*	70.97
Ankle	7	*θstd, r'min, r'avg*	83.87

Table 2- 4

Table 2-4. The optimal Feature and Step for the maximum classification accuracy from Angle Analysis. The Angle Analysis showed the Maximum Angle (θ_{max}), Angle Standard Deviation (θ_{std}), Angle Change Rate Maximum (r_{max}), and Angle Change Rate Average (r_{avg}) of Hip generated the highest maximum classification accuracy 87.10% for separate J20 and WT Angle kinematics pattern (highlighted in yellow). The second highest classification

accuracy of 83.87% (highlighted in blue) was generated from the bilateral **Ankle** feature subset and the **Elbow** angle feature subset can separate J20 and WT kinematics patterns with the third highest classification accuracy rate of 80.65% (highlighted in green).

ID	Month	Type	Trajectory Analysis Prediction	Angle Analysis Prediction	Final Class
1	13	AD	AD	AD	AD
2	13	AD	AD	AD	AD
3	13	AD	AD	WT	WT
4	13	AD	AD	AD	AD
5	13	WT	AD	WT	WT
6	13	AD	AD	AD	AD
7	13	AD	AD	AD	AD
8	13	AD	AD	AD	AD
9	13	WT	AD	WT	WT
10	13	WT	AD	WT	WT
11	13	WT	WT	WT	WT
12	13	WT	WT	WT	WT
13	13	WT	WT	WT	WT
14	4	AD	AD	AD	AD
15	4	AD	AD	WT	WT
16	4	AD	AD	AD	AD
17	4	WT	AD	WT	WT
18	4	WT	AD	WT	WT
19	4	WT	WT	WT	WT
20	4	WT	WT	WT	WT
21	4	AD	AD	AD	AD
22	4	WT	AD	WT	WT
23	4	AD	AD	AD	AD
24	4	WT	WT	WT	WT
25	4	WT	WT	WT	WT
26	4	WT	WT	WT	WT
27	4	WT	WT	WT	WT
28	4	WT	WT	WT	WT
29	4	WT	WT	WT	WT
30	4	AD	AD	WT	WT
31	4	AD	AD	WT	WT

Table 2- 5

Table 2-5. The classification result for all 31 animal entries. The Trajectory Analysis (column 4), the Angle Analysis prediction results (column 5) and the final classification result from the validation SVM analysis (column 6) were compared to the actual genotype classes of the animal entries (column 3). When the prediction result is consistent with the animal actual genotype, the cell will be highlighted in green and the mismatched cells will be marked in red. The pink cells showed the animal entries whose final classification result mismatches it actual genotype.

Occurrence Frequency of Features in the optimal feature subset with an accuracy >75%			
	Feature	Frequency	Corresponding Body Part (in order of accuracy rate)
Trajectory	sl	0	- -
	sh	2	Knee > Shoulder
	ρ	1	Shoulder
	L	2	Shoulder = Illiac Crest
	v	2	Knee > Shoulder
Angle	θmax	1	Hip
	θmin	1	Elbow
	θavg	0	- -
	θstd	2	Hip > Ankle
	$r max$	1	Hip
	$r min$	2	Ankle > Elbow
	$r avg$	3	Hip > Ankle > Elbow
	$r std$	0	- -

Table 2- 6

Table 2-6. The Occurrence Frequency of Trajectory and Angles Features detected in the feature subsets with classification accuracy rates larger than 75%. The trajectory feature subsets of three body parts (**Shoulder**, **Iliac Crest**, and **Knee**) and the angle feature subsets of three body parts (**Elbow**, **Hip**, and **Ankle**) generated classification accuracy rates larger than 75%. The **Hip** angle average is the angle feature detected in all top three body

parts that generated high classification accuracy from the Angle Analysis (highlighted in yellow).

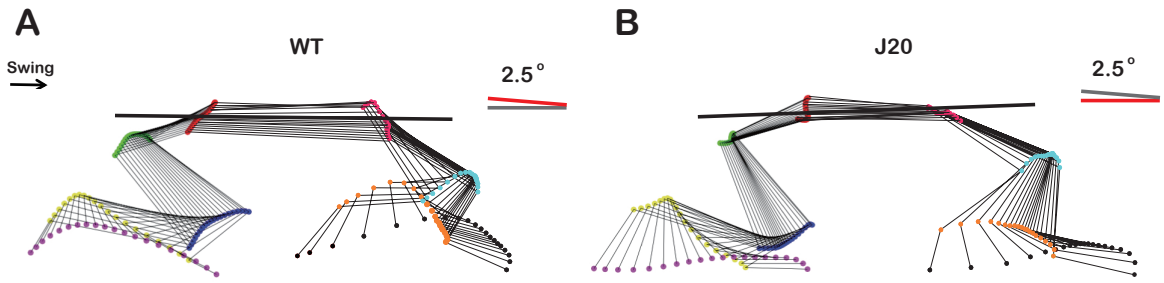

Figure 2- 6

Figure 2-6. J20 mice demonstrate Trunk and Pelvis tilting. By calculating the **Shoulder-Back-Iliac Crest** Angle and The **Hip-Iliac Crest – Back** Angle showed a 2.5^{o} tilting of the Trunk towards hindlimb direction in J20 animals (Fig. 6A) when compared to WT ones (Fig. 6B).

$\mu \pm \sigma$ of optimal features of Trajectory analysis.			
Feature Name	AD or WT	Month	$\mu \pm \sigma$
sh	AD	13	1.0334 ± 0.4049
sh	AD	4	0.9023 ± 0.1666
l	AD	13	0.8436 ± 0.2441
l	AD	4	0.8362 ± 0.1997
sh	WT	13	0.9568 ± 0.1938
sh	WT	4	1.0994 ± 0.5816
l	WT	13	1.1537 ± 0.3518
l	WT	4	1.8011 ± 1.7505

Supplementary Table 2- 1

Supplementary Table 2-1. The mean and standard deviation of the optimal **Knee** Trajectory feature subset.

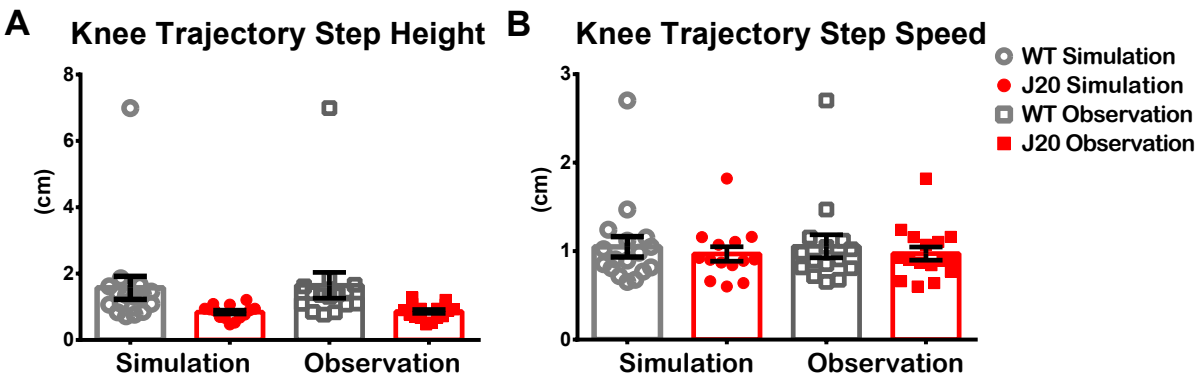

Supplementary Figure 2- 1

Supplementary Figure 2-1. The comparison of Knee(*sh*) and Knee(*v*) from the estimated classes and the actual classes (Observation). The estimated animal classes and the actual animal classes (Observation) J20 and WT **Knee** step height (**Supplementary Fig. 2-1A**) and trajectory line speed (**Supplementary Fig. 2-1B**) comparison showed no significant

difference. Furthermore, no statistic significance was detected between J20 and WT groups actual *sh* and *v* values.

$\mu \pm \sigma$ of optimal features of Angle analysis.			
Feature Name	AD or WT	Month	$\mu \pm \sigma$
θ_{max}	AD	13	1.0011 ± 0.4548
θ_{max}	AD	4	1.0179 ± 0.3767
θ_{std}	AD	13	1.2358 ± 0.8057
θ_{std}	AD	4	1.8410 ± 2.0180
r_{max}	AD	13	2.0414 ± 1.6026
r_{max}	AD	4	1.4066 ± 0.9965
r_{avg}	AD	13	1.1760 ± 0.7083
r_{avg}	AD	4	1.4244 ± 1.0965
θ_{max}	WT	13	0.9353 ± 0.1199
θ_{max}	WT	4	0.9211 ± 0.1389
θ_{std}	WT	13	0.9483 ± 0.5080
θ_{std}	WT	4	0.9778 ± 0.9076
r_{max}	WT	13	0.9356 ± 0.3097
r_{max}	WT	4	1.2020 ± 0.8930
r_{avg}	WT	13	1.0709 ± 0.2965
r_{avg}	WT	4	1.4470 ± 1.1391

Supplementary Table 2- 2

Supplementary Table 2-2. The mean and standard deviation of the optimal **Hip** Angle feature subset.

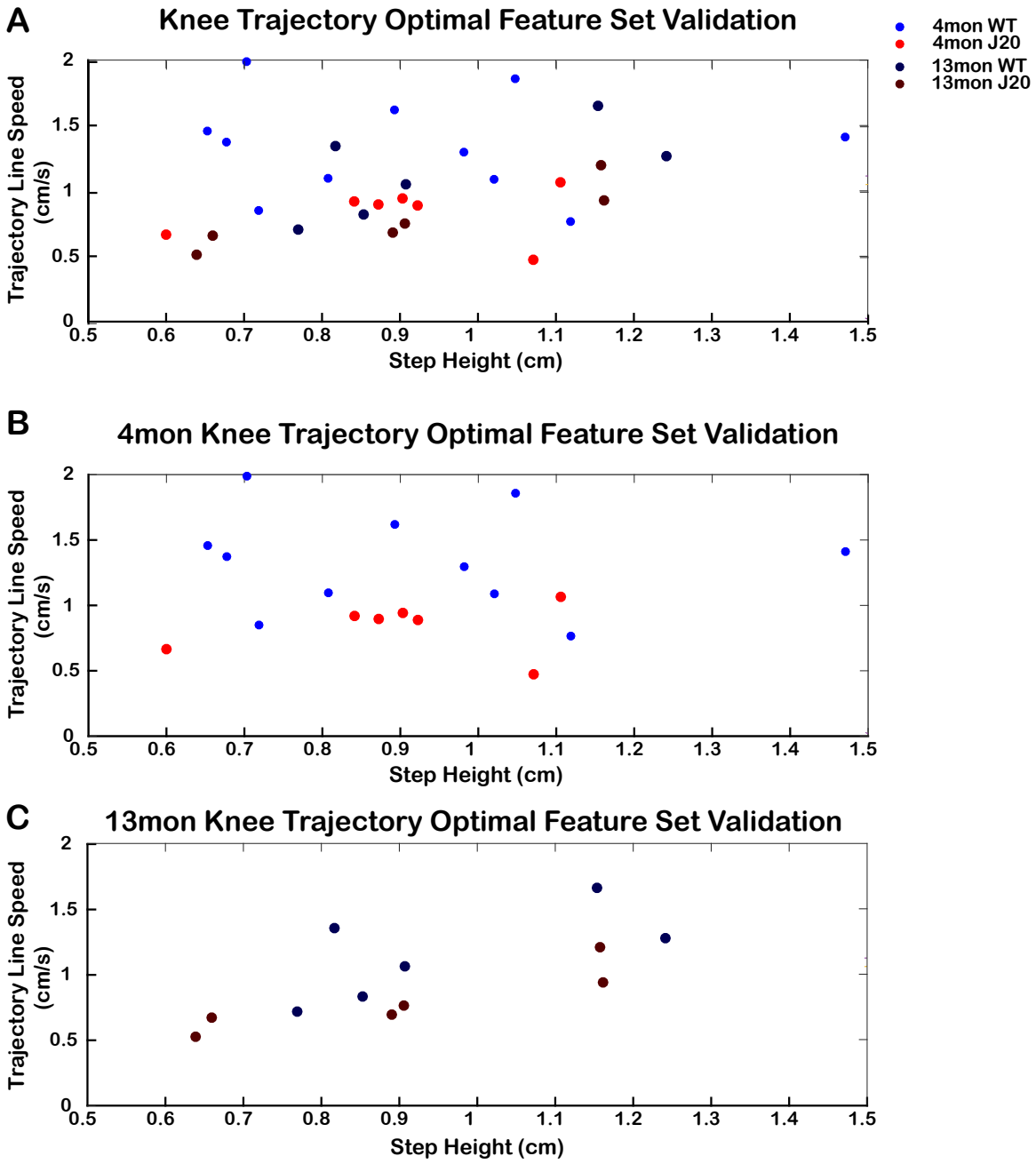

Supplementary Figure 2- 2

Supplementary Figure 2-2. The Knee (*sh, v*) trajectory feature subset validation. The scatter plot of **Knee** (*sh, v*) with the step height as x axis and trajectory line speed as y axis showed that though **Knee** (*sh, v*) can separate the kinematics pattern of J20 and WT animals (**Supplementary Fig. 2-2A**), this trajectory feature subset could not distinguish the

kinematics patterns from different age groups. The 13mon WT (dark blue dots) and 4mon J20 (red dots) scattered in a similar area that makes it difficult to separate the two groups (**Supplementary Fig. 2-2A**). **Supplementary Fig. 2-2B** and **Supplementary Fig. 2-2C** show the **Knee**(*sh, v*) of 4mon and 13mon animals respectively.

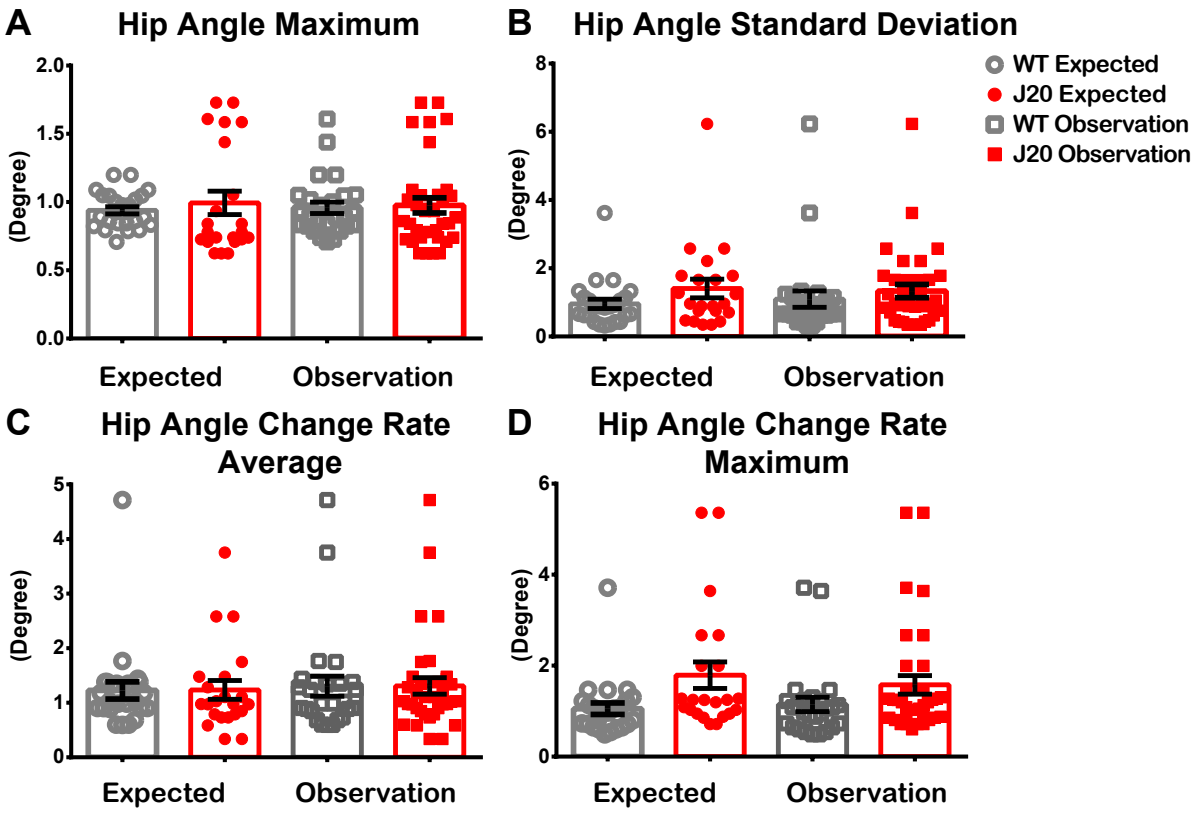

Supplementary Figure 2- 3

Supplementary Figure 2-3. The comparison of θ_{max} , θ_{std}, r_{max}, r_{avg} of Hip from the estimated classes and the actual classes (Observation). The estimated animal classes and the actual animal classes (Observation) J20 and WT **Hip** maximum angle (**Supplementary Fig. 2-3A**), angle standard deviation (**Supplementary Fig. 2-3B**), angle change rate average (**Supplementary Fig. 2-3C**), and angle change maximum rate (**Supplementary Fig. 2-3D**) comparison showed no significant difference. Furthermore, no statistic significance was detected between J20 and WT groups actual θ_{max} , θ_{std}, r_{max}, r_{avg} values.

Frequency of the Occurrence of Trajectory Features in the Optimal Feature Subset										
Feature	Frequency	Corresponding Body Part								
sl	5	Wrist	Elbow	Shoulder	Back	Iliac Crest	Hip	Knee	Ankle	Foot
sh	5	Wrist	Elbow	Shoulder	Back	Iliac Crest	Hip	Knee	Ankle	Foot
ρ	3	Wrist	Elbow	Shoulder	Back	Iliac Crest	Hip	Knee	Ankle	Foot
L	6	Wrist	Elbow	Shoulder	Back	Iliac Crest	Hip	Knee	Ankle	Foot
v	4	Wrist	Elbow	Shoulder	Back	Iliac Crest	Hip	Knee	Ankle	Foot

Supplementary Table 2- 3

Supplementary Table 2-3. The Occurrence Frequency of Trajectory Features detected in the optimal Trajectory feature subsets from the Trajectory Analysis.

Frequency of the Occurrence of Angle Features in the Optimal Feature Subset										
Feature	Frequency	Corresponding Body Part								
$\theta\ max$	2	Wrist	Elbow	Shoulder	Back	Iliac Crest	Hip	Knee	Ankle	Foot
$\theta\ min$	3	Wrist	Elbow	Shoulder	Back	Iliac Crest	Hip	Knee	Ankle	Foot
$\theta\ avg$	1	Wrist	Elbow	Shoulder	Back	Iliac Crest	Hip	Knee	Ankle	Foot
$\theta\ std$	2	Wrist	Elbow	Shoulder	Back	Iliac Crest	Hip	Knee	Ankle	Foot
$r\ max$	2	Wrist	Elbow	Shoulder	Back	Iliac Crest	Hip	Knee	Ankle	Foot
$r\ min$	4	Wrist	Elbow	Shoulder	Back	Iliac Crest	Hip	Knee	Ankle	Foot
$r\ avg$	3	Wrist	Elbow	Shoulder	Back	Iliac Crest	Hip	Knee	Ankle	Foot
$r\ std$	0	Wrist	Elbow	Shoulder	Back	Iliac Crest	Hip	Knee	Ankle	Foot

Supplementary Table 2- 4

Supplementary Table 2-4. The Occurrence Frequency of Angle Features detected in the optimal angle feature subsets from the Angle Analysis.

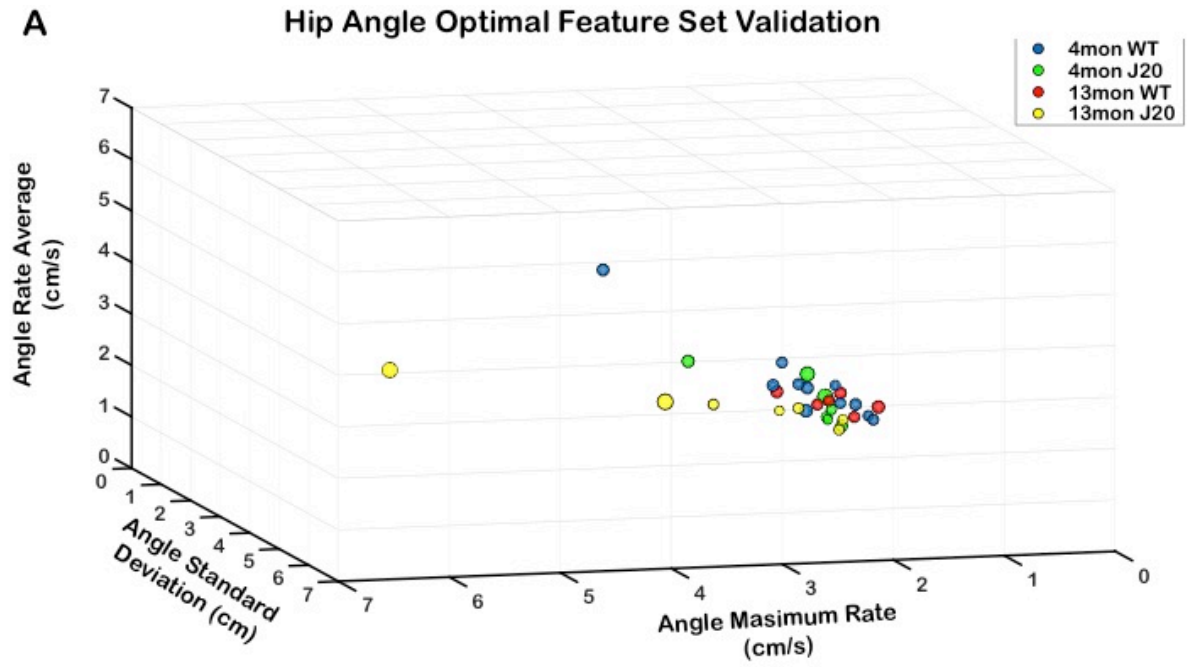
A
Hip Angle Optimal Feature Set Validation
4mon WT
4mon J20
13mon WT
13mon J20
Angle Rate Average (cm/s)
Angle Standard Deviation (cm)
Angle Masimum Rate (cm/s)

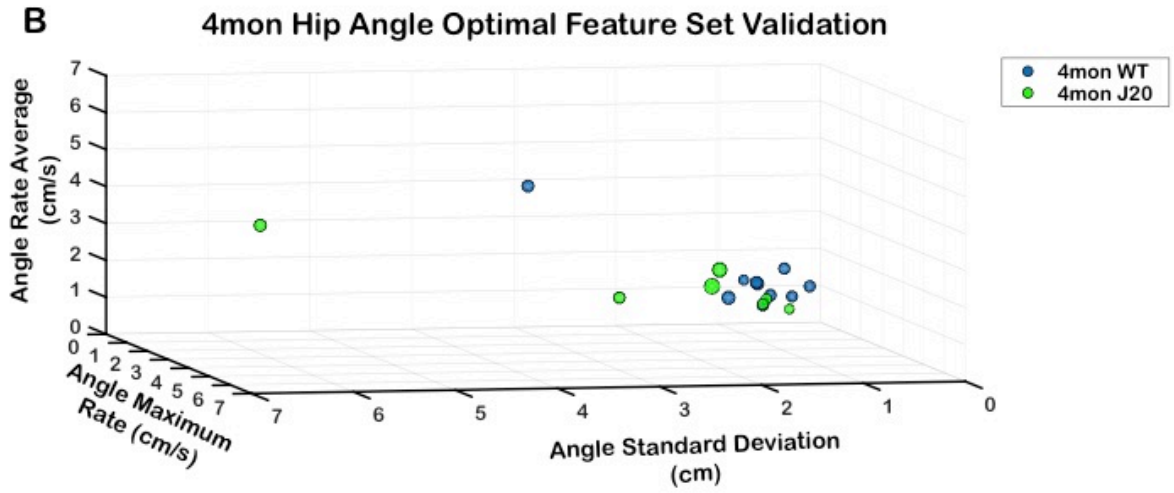
B
4mon Hip Angle Optimal Feature Set Validation
4mon WT
4mon J20
Angle Rate Average (cm/s)
Angle Maximum Rate (cm/s)
Angle Standard Deviation (cm)

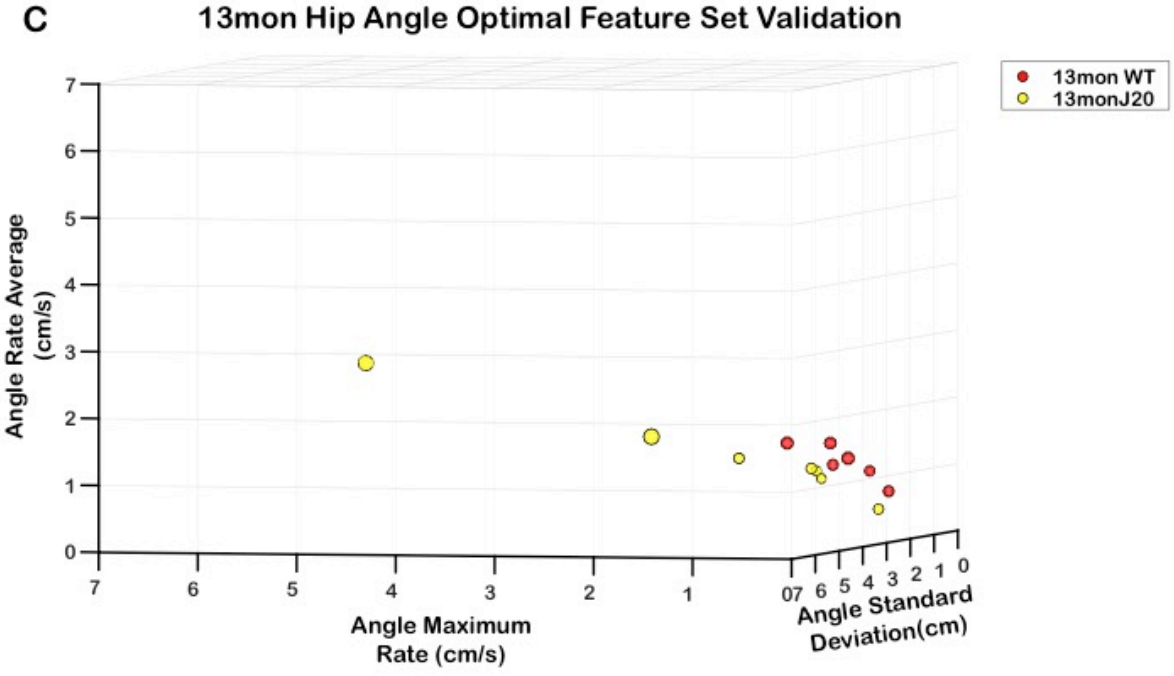
C
13mon Hip Angle Optimal Feature Set Validation
13mon WT
13monJ20
Angle Rate Average (cm/s)
Angle Maximum Rate (cm/s)
Angle Standard Deviation(cm)

Supplementary Figure 2- 4

Supplementary Figure 2-4. The Hip (θ_{max} , θ_{std}, r_{max}, r_{avg}) angle feature subset validation. The 3D scatter plot of **Hip** (θ_{max} , θ_{std}, r_{max}, r_{avg}) with the hip angle maximum rate as x axis, angle standard deviation as y axis, angle rate average as z axis and maximum angle as data circle size. The 3D scatter plot of **Hip** (θ_{max} , θ_{std}, r_{max}, r_{avg}) showed that **Hip** (θ_{max} , θ_{std}, r_{max}, r_{avg}) can separate the kinematics pattern of J20 and WT animals (**Supplementary Fig. 2-4A**), this angle feature subset could also distinguish the kinematics patterns from different age groups (**Supplementary Fig. 2-4A**). The 13mon WT (red dots) and 4mon J20 (green dots) clusters showed different distribution patterns. **Fig. 2-4B** and Supplementary Fig. 2-4C show the Hip (θ_{max} , θ_{std}, r_{max}, r_{avg}) of 4mon and 13mon animals respectively.

CHAPTER3: APP/ Aβ overexpression correlates to spinal cord based locomotion and posture control

INTRODUCTION

The results from **Chapter 2** showed that locomotion deficits exist in both 4mon and 13mon J20 mice. J20 mice demonstrated a decrease in maximum speed during quardrupedal treadmill running, an increase in drag steps number when ran at the same speed (6cm/s) and altered trunk and pelvis posture. These locomotion deficits are consistent with the clinical observation in AD patients[140–142]. Nevertheless, there is evidence showing that motor deficits including posture changes and the decrease in locomotion speed are detected in the preclinical phase of AD[140]. Understanding the mechanism of AD locomotion impairments may help to identify the at-risk people 10 or 15 years before they are clinically diagnosed with AD. However, the underlying mechanism of AD locomotion impairments is still not clear. Most of the previous studies attribute the motor deficits in AD patients to cortical pathological changes and cognition failures[143]. However, the neurophysiology of locomotion involves more components other than cortex and cognitive control. Locomotion involves the integration of sensory inputs locally at the spinal cord and in brain for complex tasks, with supraspinal inputs of descending and ascending tracts of reticulospinal, vestibulospinal, rubrospinal, and corticospinal tracts. Two levels of control of locomotion were proposed by Grigori N. Orlovsky and Mark L. Shik[144]. The first level embodies the local tonic output from the mesencephalic that activates spinal interneurons and eventually to motoneurons generating a cyclic activity of many motor pools in a manner that results in stepping. The second level involves the cortical integration of all afferent sensory inputs from the

proprioceptive position of the head, neck, torso, and limbs. In addition, the visual and auditory inputs direct and fine tune motor control from the cerebellum via the descending tracts[144] (**Fig. 3-1**). Although spinal cord is an important part of CNS, whether spinal cord is affected by AD pathology is still largely unknown.

In **Chapter 2,** all the tests for kinematics pattern detection were performed in intact naïve J20 and WT mice, the pathological changes from the brain and the spinal cord could both contribute to the observed deficits. In this chapter, my aim is to answer the following two questions:

1) Do neuropathological changes happen in the spinal cord of the J20 mouse?
2) Is spinal cord circuit involved in the locomotion kinematics changes of the J20 mouse?

To answer the first question, the expression level and the localization of hAPP, hAPPα, hAPPβ and β-Amyloid were investigated through immunohistochemistry (IHC)/ immunofluorescent (IF) staining, Western Blot (WB) and Enzyme Linked-Immuno-Sorbent Assay (ELISA) in cervical, thoracic, and lumbosacral spinal cord segments respectively.

To answer the second question, which is to determine whether spinal locomotive circuit is involved in the locomotive kinematics changes in J20 mice, I performed the complete spinal cord transection (ST) at vertebrate T7-9 (spinal cord level T10-T12) to completely cut off the ascending and descending tracts between the lumbosacral spinal cord and supraspinal structures. Because there is no ascending nor descending communication between the lumbosacral spinal cord and other CNS structures, all the sensory and motor function of the spinal mouse's hind limbs are only controlled by the lumbosacral spinal cord and the neuromuscular system connected to it.

Previous studies in the complete spinal cord transected animals (spinal animals) showed that the spinal cord is capable of an extensive level of automaticity in controlling and coordinating the locomotive activity at the spinal level independent of supraspinal inputs, e.g. bipedal treadmill stepping[97,145–147]. This automaticity or rhythmogenic capacity of the spinal cord is thought to be mediated through a network of neurons named central pattern generators (CPG). The vertebrate locomotive CPG comprises a distributed network of interneurons and motor neurons, which upon appropriate stimulation generates an organized motor rhythm that replicates the patterns of motor activity seen during repetitive locomotive tasks such as walking and running. The central organizing feature of the motor circuitry is the grouping of motor neurons into discrete operational units, called motor pools, each of which innervates a single muscle. The graded recruitment and activation of motor neurons within a pool underlies the variable changes in muscle tension that are necessary for fine muscle movement and postural control. Motor neurons integrate a range of convergent inputs, although it is likely that much of the integration that generates coordinated motor activity takes place upstream in the locomotive interneuron network. Thus, the hind limb movements' coordination and postural control can reflect fast synaptic and slower modulatory interactions between locomotive interneurons sculpt the patterns of motor neuron activity in the lumbosacral spinal circuit in spinal mice. This allows us to investigate the lumbosacral spinal circuit changes through analyzing the hind limb locomotive pattern changes of spinal mice.

Previous studies from our lab indicated that the spontaneous recovery of hind limb locomotion capability in complete spinal cord transected C57BL/6J mice could be evaluated by bipedal treadmill stepping test[145,147]. Because the genetics background of the J20 mice is C57BL/6J, the spontaneous hind limb locomotion recovery differences in the bipedal

treadmill stepping test between J20 and the WT C57BL/6J spinal mice can reflect the lumbosacral spinal cord changes due to the PDGF-driven hAPP overexpression.

MATERIALS AND METHODS

Human Tissue Sample Collection Criteria

Fresh AD subject autopsy tissues (hippocampus and spinal cord) were obtained from the UCLA Department of Pathology and laboratory medicine clinical autopsy program. The tissues used in this study were obtained after informed consented was obtained from five subjects. The subjects had no other known neurological diseases, chronic respiratory impairment, lung infections, or spinal cord or brainstem pathology. All the tissues were collected and processed according to the policy of the UCLA Department of Pathology and laboratory medicine clinical autopsy program.

Human Tissue Processing and Antibody Labeling (immunohistochemical labeling, IHC)

Human autopsy tissue was obtained from the autopsy program fixed in 10% buffered formalin and processed through a standard automatic tissue processor (Sakura VIP, Torrance, CA), embedded in paraffin, cut at 6 μm thick sections and placed on charged glass slides. Antigen retrieval was required following formalin fixation, and the antigens were retrieved using Target Retrieval Solution (TRS – Dako, Carpentaria, CA) in a pressure cooker (Cell Marque, Inc. Rocklin, CA) for 3 min. according to the manufacturer's protocol.

Optimization of the primary and secondary antibody dilutions was conducted for the following antibodies: Anti-Beta-Amyloid 1-42 (rabbit anti-human monoclonal, AB5078P, Millipore, MA), Ani-Amyloid Precursor Protein antibody (Y188, rabbit monoclonal, ab32136, Abcam, MA), Anti-beta Amyloid antibody (MOAB-2, mouse monoclonal antibody to amyloid beta peptide, Abeta 40/42, M-1586-100, Biosensis, CA) and purified anti-β-

Amyloid, 1-16 Antibody (6E10, mouse monoclonal, 803001, Biolegend, CA) (**Fig. 3-2**). Endogenous biotin was blocked with a biotin blocking kit (Dako). The primary antibody was applied at 0.4 μg/ml overnight at 4°C. The primary antibody was diluted in 5% normal horse serum in phosphate buffered saline with 0.1% Tween 20 (PBST). After 12 hours, the slides were rinsed in PBST. For immunohistochemical staining, biotinylated secondary antibody (ABC elite kit, Vector Labs, Burlingame, CA) was applied for 20 min, and signal amplification was conducted using the protocol suggested by the vendor. The peroxidase substrate (DAB peroxidase substrate kit, Vector Labs, Burlingame, CA) was applied for 1 min to visualize the immunoreaction. All washes between the various steps were done with PBS/T. Negative controls for all antibodies were performed using isotype matches for each antibody, which were placed on a duplicate slide, and processed as described above. Hematoxylin (Poly Scientific, Bay Shore, NY) was used as the counterstain. As a final step, slides were washed in water and mounted with Permount aqueous mounting medium (Fisher Scientific, Hampton, NH).

Image analysis

All the images were examined using a Leica fluorescence microscope (DM6B, Leica Biosystem, Nussloch, Germany) with Axon software (Molecular Devices, Sunnyvale, CA). For human spinal cord stainings, at least 4 pictures were taken from each subject for each specific region of interest (ROI) at each spinal cord level that we tested in the stimulation studies. After pictures were taken, all the pictures from 5 subjects were imported into ImageJ for semi-manual cell counting. Only the cells with a nucleolated nucleus (Hematoxylin counter staining positive) will be counted. A 2-D mapping matrix in which each cell in the matrix had an area of 200 X 200 um^2 was superimposed on the image, and the number of positively stained cells in each matrix element was counted. The individual cell counts from

each matrix element of repeated images taken from the same spinal cord level from the same subject were averaged, and any matrix element with more than 5 positively stained cells was marked as a positive cell of the 2-D mapping matrix. The positive 2-D matrix cell number in the grey matter and white matter of each individual subject was then counted separately for statistic analysis.

Animal Groups

All animal studies were performed according to protocols examined and approved by the Animal Use and Care Committee of University of California, Los Angeles. The J20 transgenic mouse and their littermate C57BL/6 WT control mice were further separated into two groups by 4mon (4mon J20 n=7, 4mon WT n=8) and 10-13 month age (10-13mon J20 n=13, 10-13mon WT n=10), of ~26-45g body weight were used for bipedal treadmill stepping.

Western blot analysis in the J20 mouse tissues.

Fresh-frozen spinal cords and hippocampus were harvested from Naïve J20. The tissue samples were homogenized in 110 mgml-1 in 2% w/v sodium dodecyl sulphate (SDS) in water with protease inhibitors (Roche) to recover soluble amyloid. To obtain the soluble amyloid fraction and protein for western blotting, frozen tissue samples were homogenized in cell lysis buffer (Cell Signaling), sonicated briefly and centrifuged at 14,000 r.p.m. for 10 min. The total protein concentrations of samples were measured by BCA protein assay (Thermo Fisher Scientific, Waltham, MA). The samples were then loaded to 4-12% Bis-Tris gel (Thermo Fisher Scientific, Waltham, MA), ran at 150V for 10min and then ran at 100V for 35min in Mini Gel Tank. The protein was transferred from the gel to 0.45μm nitrocellulose membrane (Bio Rad, Hercules, CA) through a 60min, 20V transfer process in Mini Gel Blot (Thermo Fisher Scientific, Waltham, MA). Immunoblotting was then

performed using the following antibodies: Anti-Beta-Amyloid 1-42 (rabbit anti-human monoclonal, AB5078P, Millipore, MA), Ani-Amyloid Precursor Protein antibody (Y188, rabbit monoclonal, ab32136, Abcam, MA), Anti-beta Amyloid antibody (MOAB-2, mouse monoclonal antibody to amyloid beta peptide, Abeta 40/42, M-1586-100, Biosensis, CA) and purified anti-β-Amyloid, 1-16 Antibody (6E10, mouse monoclonal, 803001, Biolegend, CA).

Complete mid-thoracic spinal cord transection Surgery

The spinal cord was completely transected at the T7–T9 vertebral level in all mice as described previously. Briefly, under 2% isoflurane anesthesia, a dorsal midline skin incision was made from T6 to T9 and the musculature covering the dorsal vertebral column was retracted to expose the spinal lamina. A partial laminectomy of the T7 and T8 vertebrae was performed to expose the spinal cord. The spinal cord, including the dura matter, was transected completely using microscissors. The completeness of the lesion was verified by separating the cut ends of the spinal cord with small cotton pellets and by passing a fine glass probe through the lesion site. The skin incision was closed using small surgical staples.

After surgery, the wound sites were treated with triple antibiotic ointment (Bacitracin) and the mice were given lactated Ringer's solution (1.5 ml/30 g body weight, s.c.). Buprenorphine (0.1mg/kg) will be given to the animals as analgesia. The analgesia will be given every 12 hours for at least 48 hours after the transection.

Bipedal treadmill stepping

All mice were tested hind limb stepping on a treadmill once a week from the 1st week to the 8th week after the spinal cord transection[148]. Mice were placed in a harness, which was secured to the body weight support system (Velcro). All animals were tested from 3cm s^{-1} to 15cm s^{-1} forward and reversely with a 3cm s^{-1} step while the body weight support system

supported 85% of the mouse's body weight. During testing, the animal was tested 20s for each speed before move to the next one. After being tested at all speeds, all the mice were given serotonin agonist, Quipazine (0.3mg/kg body weight, Sigma) i.p. and tested again on treadmill at all speeds forward and reverse 20min after injection. Between tests, all mice were placed in the harness 20-25min/day for acclimation. All the locomotion tests were recorded and analyzed by SIMI motion capture system.

Immunofluorescent staining (IF)

Immunolabeling was done on 30um spinal cord sections from all the groups. Staining was done using the following two primary antibodies: Ani-Amyloid Precursor Protein antibody (Y188, rabbit monoclonal, ab32136, Abcam, MA), Anti-beta Amyloid antibody (MOAB-2, mouse monoclonal antibody to amyloid beta peptide, Abeta 40/42, M-1586-100, Biosensis, CA). Plaque load were quantified using ImageJ. Total plaque area was expressed as a percentage of the total spinal cord grey matter or the total hippocampal area. For immunofluorescent staining, the procedure for primary antibody or isotype primary antibody match incubation was the same as described before, and fluorescent conjugated secondary antibodies (488 antimouse, Cy3 antirabbit, Jackson Laboratory, Bar Harbor, ME) were incubated at room temperature for 2 hours with the tissue instead of biotinylated secondary antibodies. After washes, the slides are mounted in Vector DAPI mounting solution (Vector Labs, Burlingame, CA) and examined using fluorescence microscopy.

Statistics Data analysis

All variables are presented as the mean ± the standard error mean (SEM). To analyze and compare the APP/Aβ expressing in human spinal cord slices from cervical (C5), thoracic (T12) and lumbar (L4), Bonferroni t-test and Sidak's multiple comparisons test was applied

to compare the number of APP/Aβ positive matrix cells (**Chapter 3 Image process**) in the grey matter or white matter of C5/T12/L4 spinal cord slices. The APP/Aβ positive matrix cells in the white matter or the grey matter were analyzed separately. The stats were performed in R (Ver. 3.3.3) and validated by GraphPad 6.0 (GraphPad Software Inc. San Diego, CA). The level of significance was selected as $P<0.05$ for all comparisons.

One-way ANOVA and post hoc Sidak's multiple comparisons test were applied to compare the Y188+ or MOAB2+ cell percentage in J20 L4 spinal cord before and after mid-thoracic complete spinal cord transection. The Y188+ or MOAB2+ cell number percentages in the white matter or the grey matter were analyzed separately. The stats were performed in R (Ver. 3.3.3) and validated by GraphPad 6.0 (GraphPad Software Inc. San Diego, CA). The level of significance was selected as $P<0.05$ for all comparisons.

RESULTS

Extracellular amyloid plaques and intracellular APP/Amyloid-beta overexpression was detected in the hippocampus of AD subjects.

Dense core amyloid plaques were detected in all the regions of the AD subject hippocampus, including the dentate gyrus, CA1-CA4 regions and the sucbiculum (**Fig. 3-3**). Besides the amyloid plaque formation, the increase of Aβ was also detected intracellularly in the AD patient hippocampus by the $Aβ_{1-42}$ specific antibody AB5078P. As indicated by **Fig. 3-3D**, the intracellular Aβs were detected in the granule cell layer of the dentate gyrus as well as the CA2 and CA3 pyramidal cell layers in the hippocampal slices from all tested AD patients (n=5). This result indicates that extracellular amyloid plaques and intracellular APP/Aβ increase are both important features of the changes in AD patient tissue.

Intracellular APP/Aβ overexpression but not amyloid plaques was detected in the spinal cord of AD subjects.

The same IHC staining procedure was applied to the AD patient spinal cord slices. The IHC staining showed that the intracellular Aβ also increased in AD patient lumbar spinal cord slices (L4) when compared to the non-AD patient tissue samples (**Fig. 3-4,** AD L4 slice n=30, non-AD L4 slice n=30). The intracellular Aβ increase was detected in all lamina layers of the L4 spinal cord grey matter, including the dorsal horn (**Fig. 3-4F$_1$**), the intermedial area (**lamina VII, Fig. 3-4F$_2$**) and the ventral horn (**Fig. 3-4F$_3$**). Although AD hippocampus and L4 spinal cord both showed intracellular Aβ increases, unlike the AD hippocampus which also had heavy amyloid plaques loading in all the regions (**Fig. 3-4B, Fig. 3-4C$_{1-3}$**), no amyloid plaque was detected in the L4 spinal cord slides (**Fig. 3-4E, Fig. 3-4F$_{1-3}$**).

The intracellular APP/ Aβ increase was detected in both the grey matter and white matter of the cervical, thoracic and lumbar spinal cord.

To investigate whether the APP/Aβ increase exists in all spinal cord levels, slices from the cervical (C5), thoracic (T12) and lumbar (L4) spinal cord levels were also studied by IHC staining. To better analyze the APP/Aβ increasing cell number and distribution pattern, a 2D-map matrix consists of 200X200μm^2 matrix cells was generated for each spinal cord level of each individual patient. For each spinal cord level, 6 consecutive coronal section slices (6μm) were taken from the rostral end of the tissue segment block, and the immunoreactive cell number was averaged among the 6 slices from the same spinal cord level of each individual subject. When the averaged APP/Aβ+ cell number from all 6 slices from the same spinal cord level of the same patient larger than 5 within a 200X200μm^2 matrix cell (**Fig. 3-5B**), the matrix cell will be marked as positive. The APP/Aβ+ matrix cell in the grey matter was

labeled yellow while the APP/Aβ+ matrix cell in the white matter was labeled grey. The APP/Aβ+ 2D maps of C5, T12 and L4 were then generated based on the cell count method described above (The representative 2D maps of C5, T12 and L4 were shown in **Fig. 3-5A**, patient number n= 1). The positive matrix cell count in the white matter and grey matter was performed and analyzed separately in all 5 tested AD individuals. The matrix cell number of the white matter is significantly higher than that of the grey matter in both the cervical (C5) and thoracic (T12) level ($P_{C5\ White\text{-}Grey\ matter}$ = 0.000793, $P_{T12\ White\text{-}Grey\ matter}$ = 0.00616). However, no significant difference was detected between the white and grey matter matrix cell numbers of the lumbar level (L4) (**Fig. 3-5C**). This result indicates that the APP/Aβ+ increase exists both in the cell body as well as the axons in the white matter tracts.

The complete spinal cord transection in J20 mice decreased the Aβ expression in the white matter and most grey matter regions significantly but did not change the lamina VI APP/Aβs in L4.

The results from **Fig. 3-5** indicate that there could be two source of spinal cord APP/Aβs: 1) APP/Aβs are locally generated by neural cells in the spinal cord; 2) APP/Aβs are expressed and generated by the neural cells whose cell bodies reside in the supraspinal structures (e.g., cortex) and APP/Aβs are transported down to the spinal cord through the descending tracts (e.g., corticospinal tract) (**Fig. 3-6**). To further investigate the exact source of the spinal APP/Aβs in lumbar spinal cord, a mid thoracic complete spinal cord transection was performed in J20 mice to cut off all the tracts connecting the lumbar spinal cord to the supraspinal structures. APP/Aβs overexpression was also detected in J20 L4 spinal cord slices when compared to those of their WT littermates (**Fig. 3-7**). After 8 weeks post the spinal cord complete transection, APP/Aβs+ signals decreased significantly in L4 slices (**Fig. 3-8A**). Because among all the tested antibodies, Y188 showed that it was specific to detect

the full length APP or the C-terminus fragment (CTF) of the cleaved APP; MOAB2 was specific to Aβs, the Y188+ and MOAB2+ signals indicated the distribution of the total APPs (both processed or non-processed) and total Aβs respectively. The analysis of Y188+ and MOAB2+ signal distribution was performed in different spinal lamina layers as well as the corticospinal tracts. The analysis showed that after the complete transection, total APPs decreased in all the lamina layers and the corticospinal tracts except in the lamina I, III and VI. The total Aβ+ signals also showed a similar decrease after the spinal complete transection, however, the signals intensity from the lamina I-II, V-VIII remained largely unchanged (**Fig. 3-8B**). These results together suggest that the majority of spinal cord hAPP expressions is correlated with supraspinal innervations but the hAPP expressions in lamina I, III and VI are locally expressed in the spinal cord.

The spontaneous bipedal locomotion recovery was delayed in spinal J20 mice when compared to WT littermates.

In order to completely block the supraspinal inputs for hindlimb locomotive control, the complete spinal cord transection (ST) at mid-thoracic vertebrate level (vertebrate T7-9, corresponding to spinal level T11-12) was performed to separate the lumbosacral spinal cord from its superior CNS structures. The natural spinal locomotive function recovery in spinal mice was assessed through bipedal treadmill stepping paradigm (**Fig. 3-9A**). It has been proven by previous studies that with the body support harness, spinal animals were able to have higher degree of freedom of hindlimb movement. The sensory input from treadmill belt movement will stimulate the lumbar locomotive spinal circuit to generate steps. The researches also suggested that the rehabilitation curve with spinal plasticity. Since hAPP/hAβ increase impairs the cortical and hippocampal neural plasticity in cultured cells, cultured tissues slices, as well as when hAPP/hAβ injected into the animal brain, the hypothesis here

is that the hAPP/hAβ overexpression in J20 spinal cord will delay the spontaneous bipedal stepping rehabilitation after complete ST.

This hypothesis was supported by the decrease of bipedal step numbers after ST in J20 animals compared to WT (**Fig. 3-9B**). The 4mon WT mice bipedal step number increased fastest and also most significantly after ST, while the average consecutive step number 4mon WT mice were able to perform within the 20s analysis bin is 5.75 for the 7 weeks after ST, while 13mon WT mice group showed a slow recovery of step number. Both 4mon and 13mon WT ended in having an average for 6.61 consecutive bipedal stepping at the end of 7 weeks testing. However, both 4mon and 13mon J20 animals bipedal treadmill step number average of the 7 weeks were below 4 and ended in having 2.39 average bipedal step number at the 7th week post-ST. A closer look at the bipedal kinematics of J20 at week 1(W1) post-ST and week 7(W7) post-ST (**Fig 3-9 E_{1-4}, G_{1-4}**) showed that though spontaneous bipedal stepping rehabilitation happened in J20, there were the decrease in stability in executing step cycles, limitations in movement range and the incoordination in left and right step trajectory in J20 bipedal stepping pattern when compared to WT littermates (**Fig 3-9 D_{1-4}, F_{1-4}**).

All the J20 and WT animals were also subjected to a pre-ST bipedal treadmill step baseline testing, in which intact J20 and WT animal were also put into harness and step with the body weight support system to measure the bipedal stepping number. Both 4mon and 13mon J20 mice had a significant decrease in bipedal step number pre-ST surgery as well, suggesting that the decrease in bipedal step number was not due to hind limb muscle strength decrease because the animal body weight was all adjusted to 30% of the total body weight.

The delay in bipedal step number recovery and the instability of bipedal step execution in J20 compared to WT mice indicated that the spinal locomotive circuit of J20 cannot adapt the motor outputs to sensory inputs as effectively as that of WT mice. Therefore, the next hypothesis is that the spinal plasticity and learning ability is compromised in J20 spinal cord.

DISCUSSION

The APP/ Aβ overexpression in the spinal cord indicates that the amyloid cascade also exist in the spinal cord.

In most of previous neuropathological studies of AD, the spinal cord has been considered as a CNS structure unaffected by amyloid cascade because the typical amyloid-related AD pathological biomarker, amyloid plaques, was not found in the AD spinal cord. However, as more and more researches indicate that APP overexpression as well as soluble Aβs plays an important role in AD pathogenesis than Aβ plaques, we need to reconsider whether the spinal cord is truly "spared" by the influence of APP and its cleavage products. In this study, the IHC results in the human spinal cord slices are consistent with the previous researches. No obvious Aβ plaque formation was detected in the AD spinal cord when compared to that of non-AD subjects (**Fig. 3-4, Fig. 3-5**). However, intracellular APP/Aβ increase was detected in both the hippocampus and the spinal cord of AD patients, indicating that the APP/Aβ overexpression as well as the elevation of amyloidogenesis in the hippocampus may also happen locally in the spinal cord circuit.

However, there are more possible sources of spinal APP/Aβ other than local APP/Aβ overexpression and processing in the spinal neural cells (**Fig. 3-6**). The overexpressed APP bound to the membrane of supraspinal neurons can be also detected in the spinal cord by

being expressed on the membrane of axons or synaptic terminals in the descending tracts. Furthermore, the soluble Aβs in the circulating cerebral spinal fluid (CSF) can be uptake by neurons through lipid rafts and endocytosis. Some studies even suggested that the intracellular Aβs could self-propagate across cells and tissues. The spinal APP/Aβ expression increase can be due to any of the mechanisms described above as well as a mixed effect of APP/Aβ expression increase from different sources. Then these possibilities lead to two questions:

1) Does spinal cord overexpress and process APP locally?

2) If spinal APP/Aβ increase is a mixed effect of different mechanisms, how much does individual mechanism contribute to the overall spinal APP/Aβ increase?

The local spinal APP/Aβ overexpression and processing is suggested to happen in the lamina III and VI layers.

One direct way to investigate the contribution of local APP/Aβ expression and amyloidogenesis to the spinal APP/Aβ expression levels is to cut off all the supraspinal inputs to the spinal cord by complete spinal cord transection. I hypothesized that the local spinal APP overexpression and processing levels will not be affected by the complete spinal cord transection. However, the APP/Aβ overexpressed or processed originally in supraspinal structures, will decrease significantly after cutting off the supraspinal inputs. The APP/Aβ expression levels were studied after 8 weeks post the complete spinal transection to ensure the degradation of the supraspinal-origin APP in the lumbar spinal cord.

Notably, because Aβs could also be uptake by spinal neural cells from the circulating CSF, the spinal cord complete transection may not affect the lumbar Aβ expression significantly.

This hypothesis is supported by the test results from **Fig. 3-8B.** In **Fig. 3-8B**, the Y188+ signals, representing the total processed and non-processed hAPP, significantly decreased in most spinal lamina layers except 3 layers (lamina I, III and VI), while the MOAB2+ signals, representing the total soluble and non-soluble hAβs, only significantly decreased in 4 out of 10 spinal lamina layers (lamina III, IV, IX and X). There are 4 lamina layers (lamina II, V, VII and VIII) exhibited a decrease in total hAPP but no significant change in total Aβs after the complete spinal cord transection. This result suggest that in these 4 lamina layers, the spinal hAPP expression levels are significantly affected by supraspinal connections but the hAβ expressions in these 4 lamina layers are not closely related to supraspinal inputs. Other mechanisms, e.g. the circulating hAβ uptakes and the hAβ generated locally by neural cells from other lamina layers, might contribute more to the hAβ expressions in lamina II, V, VII and VIII.

Furthermore, interestingly, among the three lamina layers (lamina I, III, and VI) that didn't show significant decreases in the spinal hAPP, the hAβ expression levels in lamina I and VI still remained unchanged after the complete spinal transection. However, the hAβ expression level in lamina III decreased significantly after the transection. There could be two possible explanations for this phenomenon:

1) Before the transection, lamina III uptake hAβ from the supraspinal neuronal innervations. The spinal transection didn't affect the basal expression and processing of the local hAPP in the lamina III but decreased the supraspinal-origin hAβ level.
2) When the total hAPP expression level in lamina III still remains unaffected after the spinal transection, the hAPP processing level decreases and generates fewer hAβs. For the 2nd possible explanation, the mechanism of hAPP processing level decrease in lamina III is still

unknown. It could because of the lack of supraspinal inputs. It could also be caused by the lack of peripheral sensory inputs after the complete spinal transection since the animal is paralyzed. The detailed underlying mechanism still needs further investigation, however, the results above suggest that the neural component in lamina I, VI and III could play special roles in the AD spinal cord and contribute to lumbar spinal cord related locomotion deficits observed in J20 mice (**Fig. 3-9**).

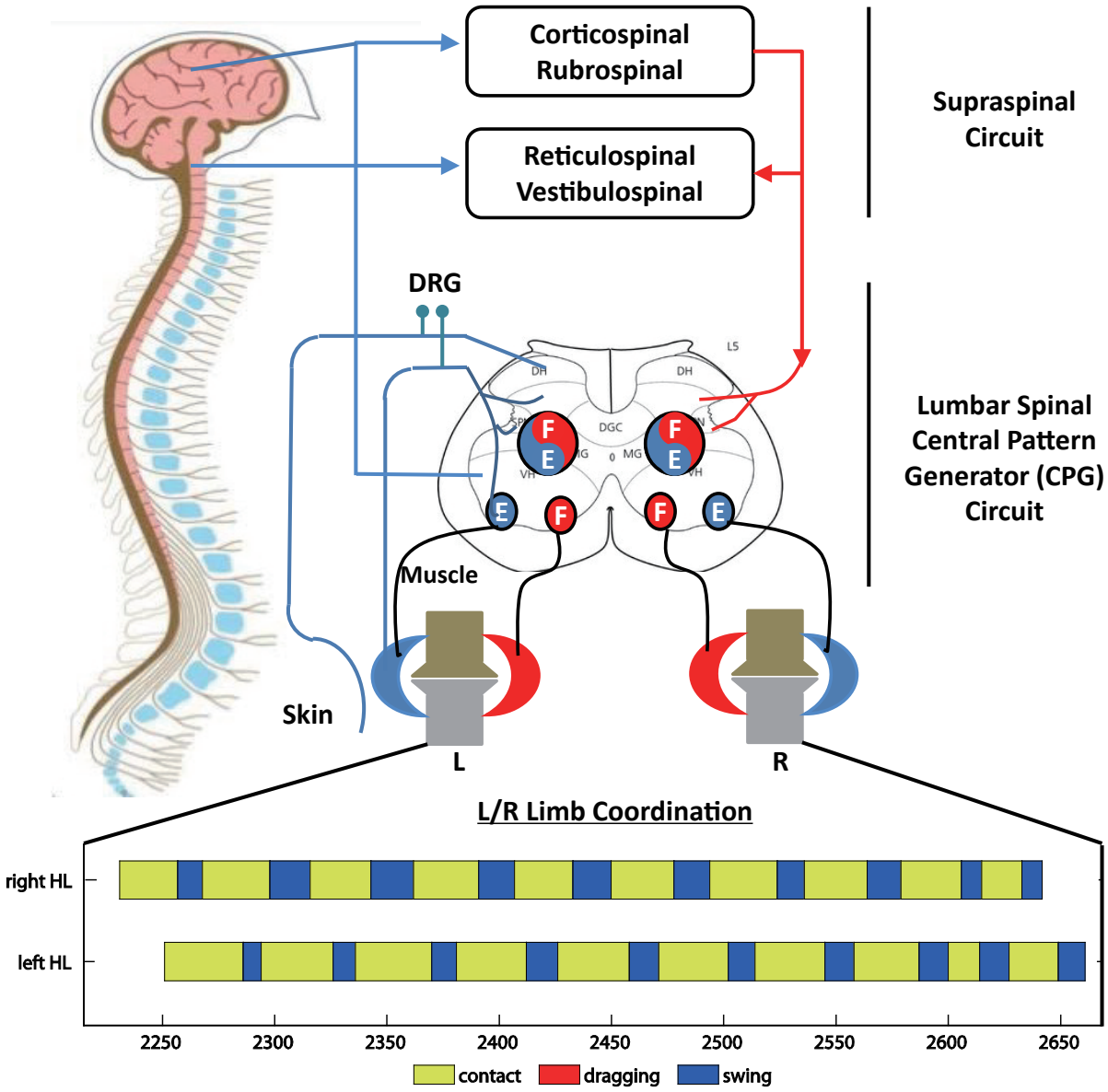

Figure 3- 1

Figure 3-1 The schematic illustration of hind limb locomotion control. The hind limb movements and left/right limb coordination (L/R limb coordination) are controlled and regulated by both supraspinal controls and the lumbar central pattern generator (CPG). The supraspinal controls including the corticospinal tract that projects from cortex, rubrospinal tract that projects from the red nucleus, cerebellospinal tract that projects from cerebellum, and vestibulospinal as well as reticulospinal tracts that project from the medulla. The spinal CPG consists the muscle-innervating motor neurons and the interneuron network. When the

sensory inputs from skin or from tendons/muscle spindles enter the spinal cord, they will be either processed by spinal CPG or be relay to the supraspinal structures for further processing.

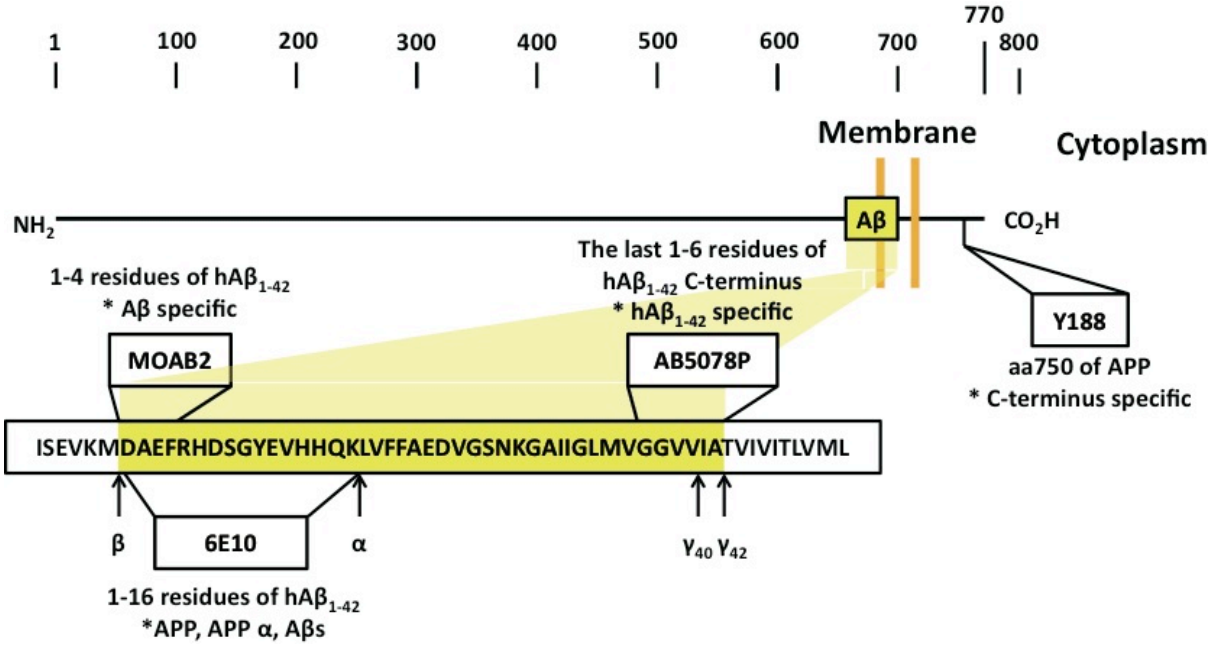

Figure 3- 2

Figure 3-2 The antibody epitope mapping of the APP/Aβ antibodies used for APP/Aβ detection. Aβ sequence locates in the transmembrane domain of APP protein. The antigen location of MOAB2 maps to residues 1-4 of human amyloid beta peptide 40/42; the epitope of 6E10 maps to the first 1-16 residues of human amyloid beta peptide 42; AB5078P epitope maps to the C-terminus 1-6 residues of human amyloid 1-42; and Y188 is specific to the 750th amino acid of APP, which maps to the intracellular C-terminus of APP.

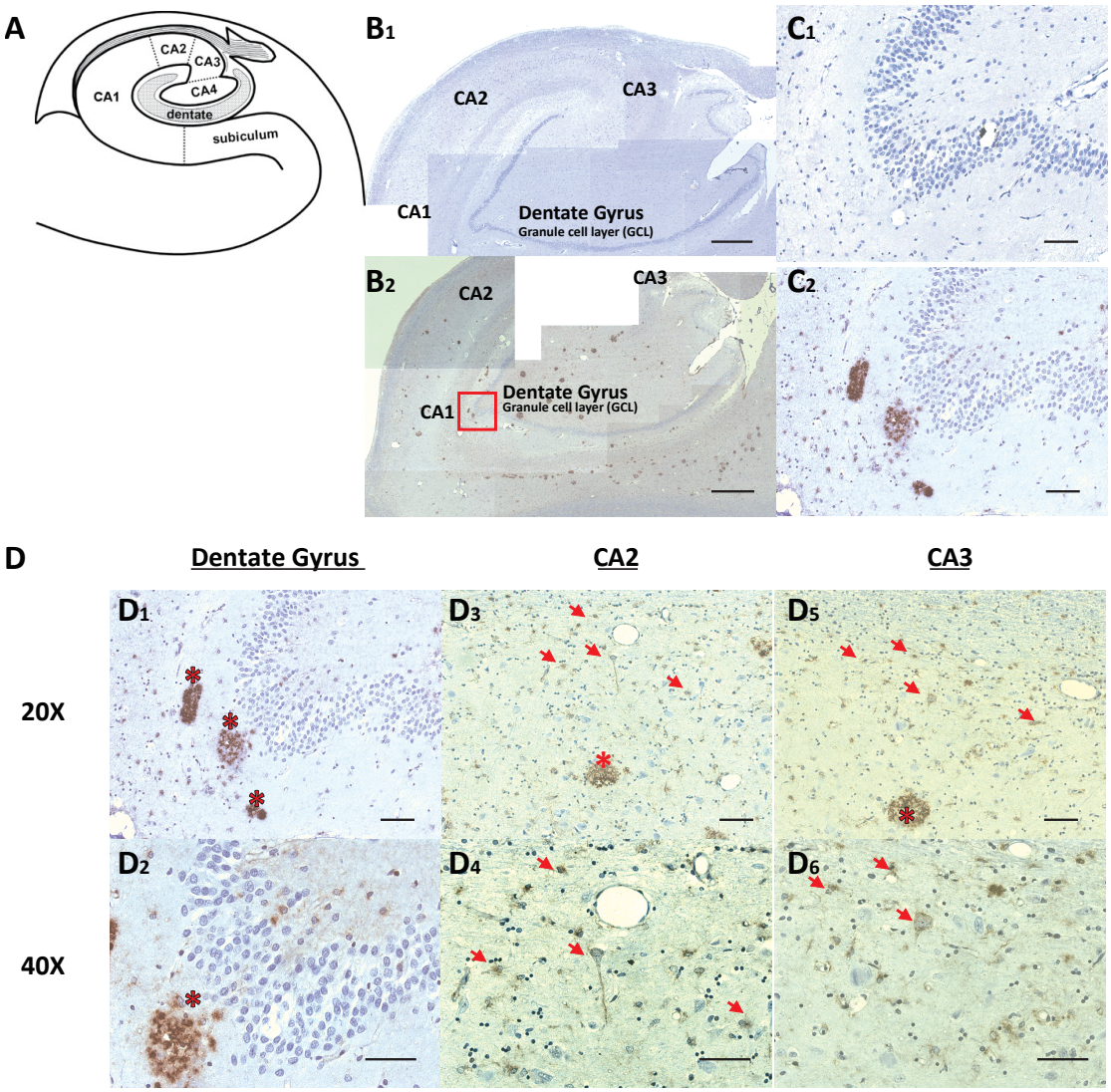

Figure 3- 3

Figure 3-3 Intracellular APP/Aβ elevation as well as amyloid plaques were detected in the AD patient hippocampus.

A) The illustration of hippocampus structure. Amyloid Plaques do not form in the hippocampus of the non-AD patient (**B_1**: x5, scale bar: 100μm; **C_1**: x20, scale bar: 50μm) but exist in all the regions of hippocampus of AD patients (**B_2:** x5, scale bar: 100μm; **C_2:** x20, scale bar: 50μm). **D)** Intracellular APP/Aβ increases and extracellular amyloid plaques were detected in AD patient hippocampus, scale bar: 50μm. The arrow indicates the cells with APP/Aβ increase and the asterisk marker indicates amyloid plaques. The thickness of the hippocampus and spinal cord slices is 6μm.

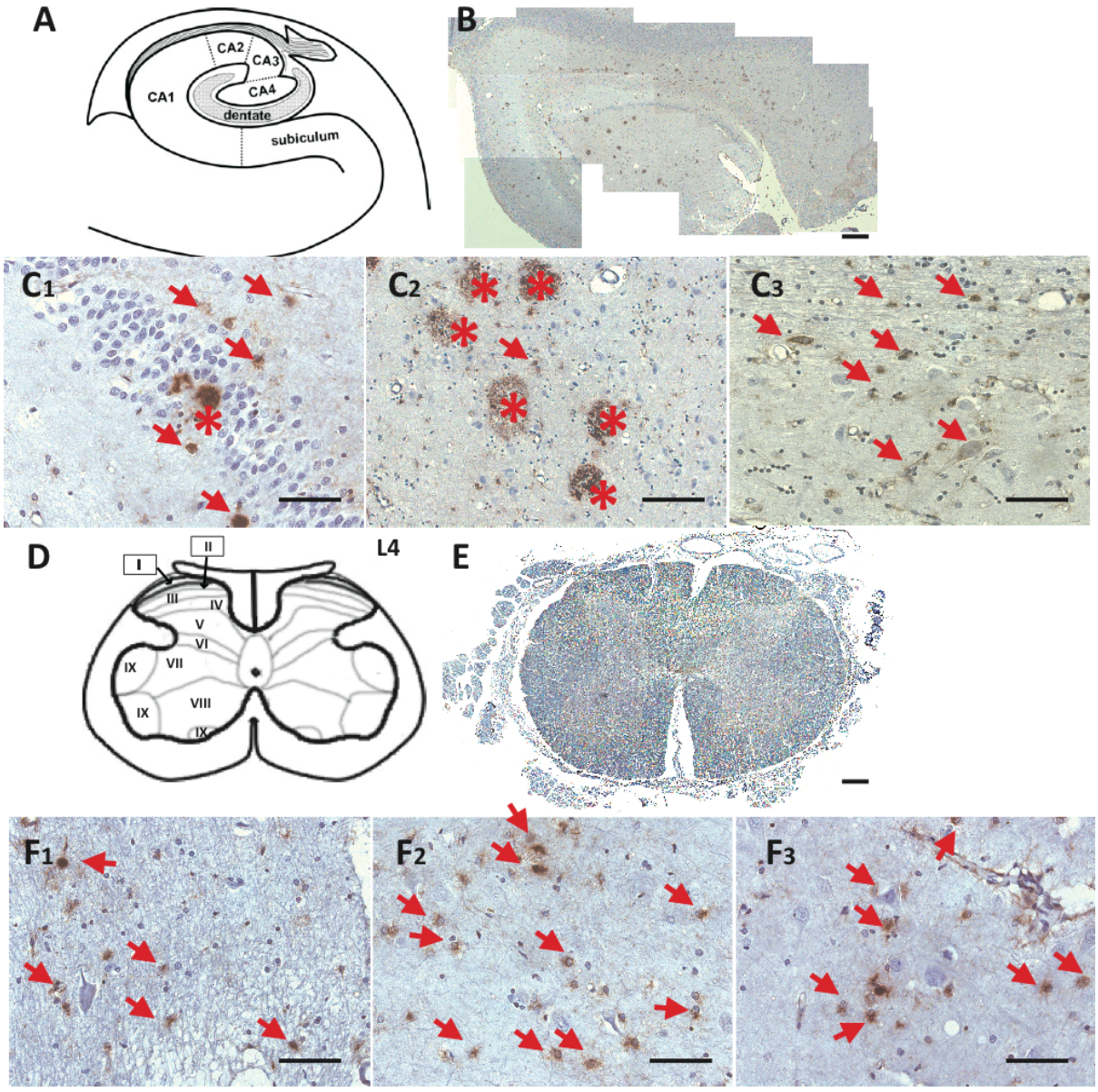

Figure 3- 4

Figure 3-4 Intracellular APP/Aβ elevation was detected in human lumbar spinal cord.

Both extracellular amyloid plaques and intracellular APP/Aβ elevation were detected in all the regions in the human hippocampus (**A, B, C$_{1-3}$**). In the human spinal cord, no amyloid plaques were found in the lumbar spinal cord (L4). Only intracellular APP/Aβ increase was detected in the spinal cord. A) The illustration of hippocampus structure. **B)** The x5 view of human hippocampus, scale bar: 100μm. **C$_{1-3}$**) The x40 view of the dentate gyrus, CA2 and

CA3 region in the human hippocampus, scale bar: 50μm. **D)** The illustration of L4 spinal cord and the grey matter lamina layout. **E)** The x5 view of human spinal cord slice, scale bar: 100μm. **F_{1-3}**) The x40 view of the dorsal horn $_1$, lamina VII $_2$ and ventral horn region $_3$ in the human L4 spinal cord, scale bar: 50μm. The arrow indicates the cells with APP/Aβ increase and the asterisk marker indicates amyloid plaques. The thickness of the hippocampus and spinal cord slices is 6μm.

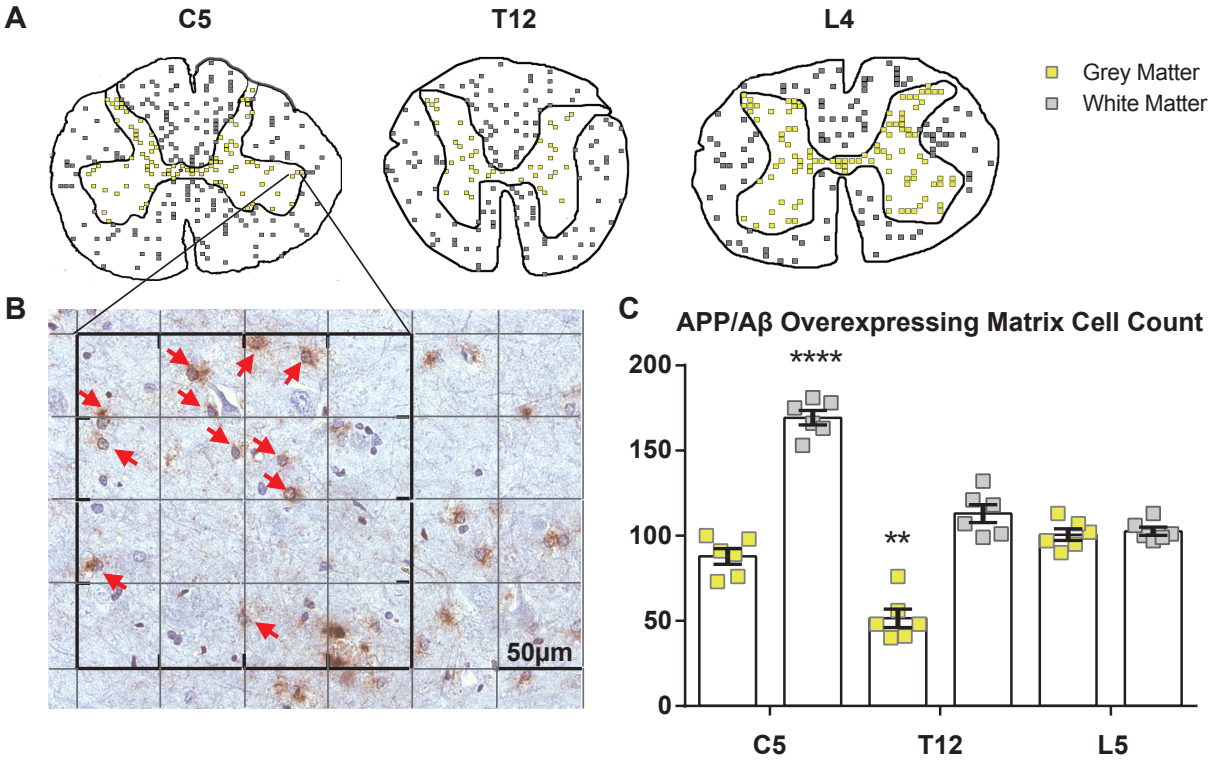

Figure 3- 5

Figure 3-5 The representative 2D-map matrix shows APP/Aβ expression distribution patterns are different among different human spinal cord levels. A) The 2D APP/Aβ expressing pattern maps of cervical level (C5), thoracic (T12), and lumbar (L4). Each individual map shows the averaged information of the corresponding spinal cord segment from one individual AD patient. The analysis spinal cord segment thickness is 36μm (6 consecutive spinal cord slices, with a slice thickness equal to 6μm) and collected from the rostral end of the segment block. **B)** A 2D matrix made by 200x 200 μm^2 matrix cells is superimposed upon the IHC staining pictures. The APP/Aβ expressing cell number in each matrix cell is counted and then averaged within the same subject. **C)** The 2D map matrix cell counts from the grey and white matter from C5, T12 and L4 from 5 AD patients. The APP/Aβ positive matrix cell numbers of the white matter from C5 and T12 are significantly higher than those of the grey matter. No significant difference in APP/Aβ positive matrix

number is detected between L4 grey and white matter. The arrow indicates APP/Aβ expressing cells. **: P<0.01, ****: P<0.0001.

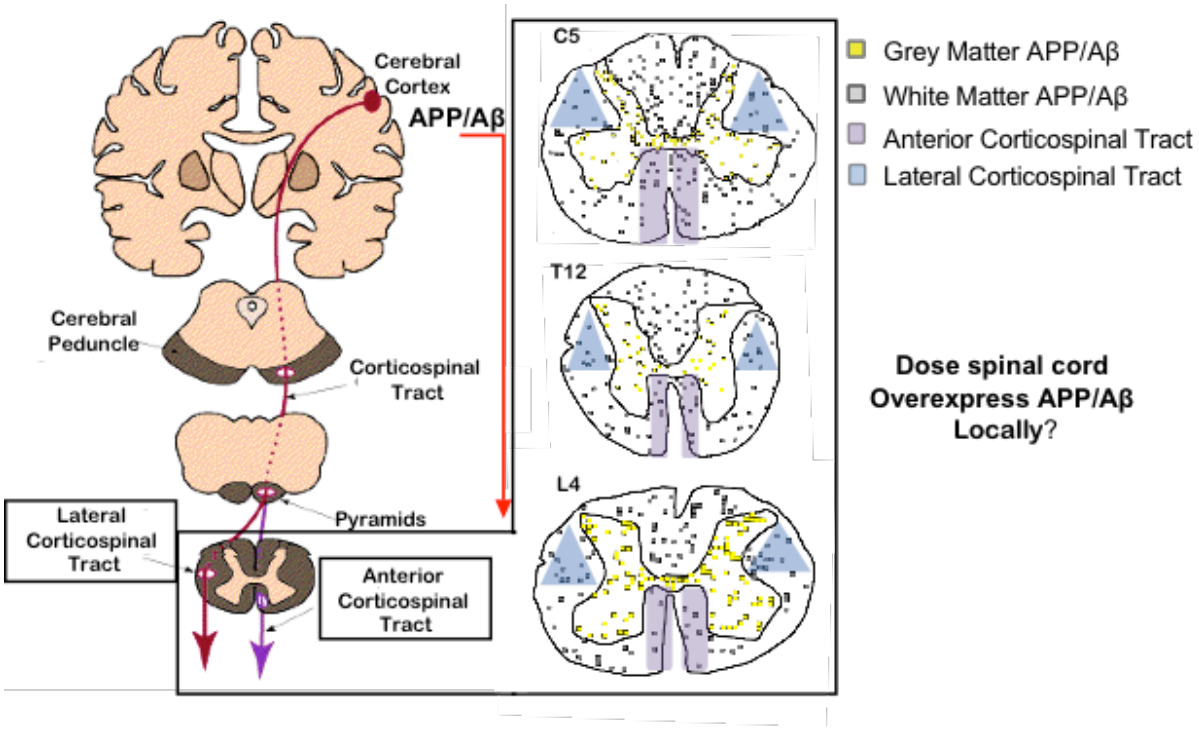

Figure 3- 6

Figure 3-6 The proposed hypothesis of spinal cord APP/Aβ sources.

The spinal cord APP/Aβ is generated through two paths. The first path is through the corticospinal tracts projected from the cerebral cortex. The cortical neuron overexpressing APP/Aβ sends axons into the spinal cord through the anterior (purple) or lateral (blue) corticospinal tracts by overexpressing the membrane-bound APP on axon membrane and synaptic terminal membrane. Soluble Aβ can also be trafficked down the axons in corticospinal tracts in vesicles. The second path is through the local processing of the APP expressed by spinal cord neurons.

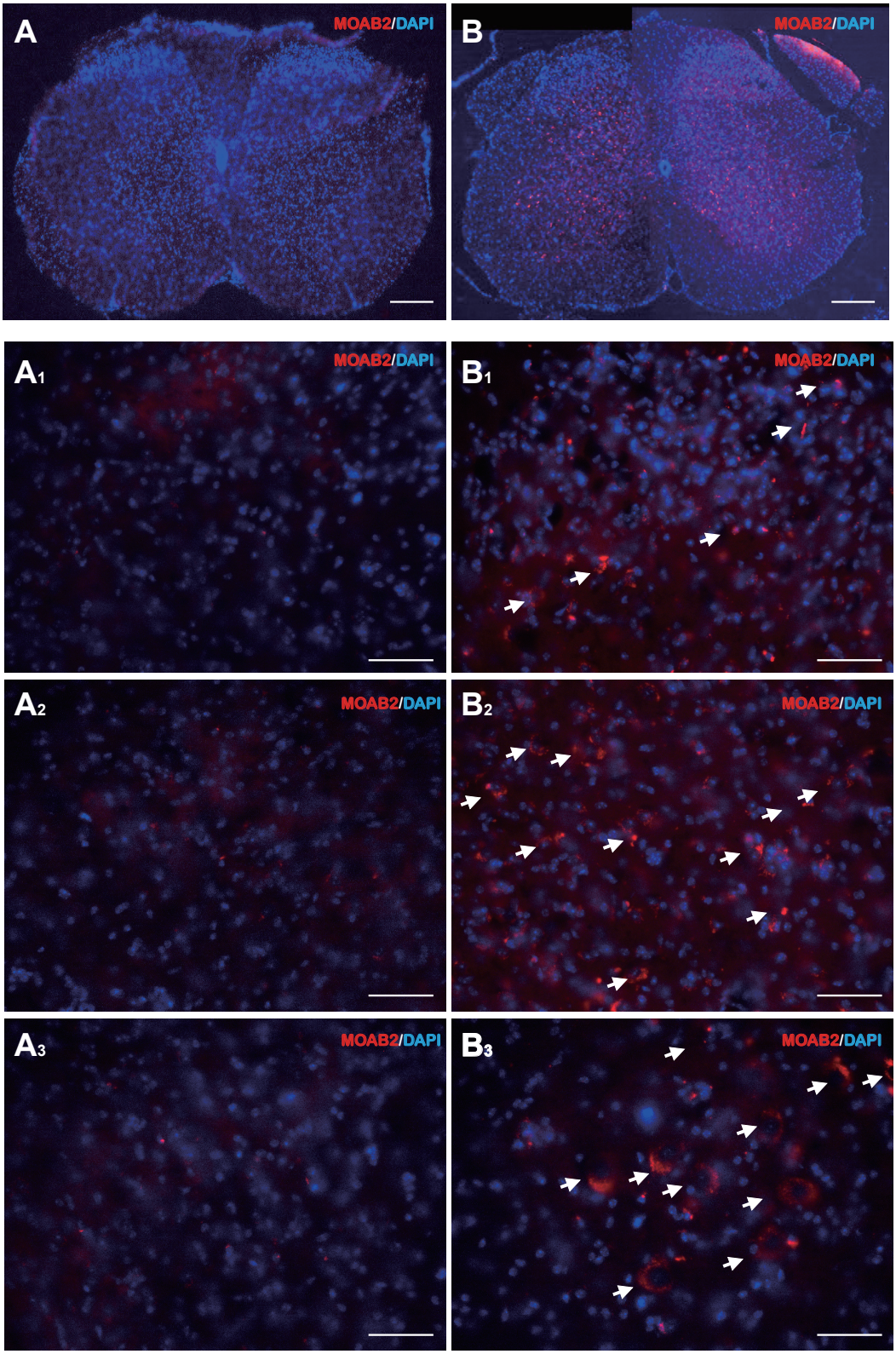
A
MOAB2/DAPI
B
MOAB2/DAPI
A1
MOAB2/DAPI
B1
MOAB2/DAPI
A2
MOAB2/DAPI
B2
MOAB2/DAPI
A3
MOAB2/DAPI
B3
MOAB2/DAPI

Figure 3- 7

Figure 3-7 Staining of MOAB2 in L4 spinal cord slice showed hAβ overexpression in the entire grey matter area. Since MOAB2 antibody is only specific to hAβ but not hAPP, hAβ positive signals were only detected in J20 spinal L4 cord slices **(B, B_{1-3})** but not the WT L4 **(A, A_{1-3}).** The pictures of 5X WT (A) and J20 (B) L4 spinal cord and the representative 40X picture of cells in different grey matter regions (A_1, B_1: Dorsal Horn; A_2, B_2: Medial ventral area, laminar VII; A_3, B_3: Ventral Horn). The arrows indicate positive signals of MOAB2 staining, for panels A and B, the scale bar= 200um, and for panels A_{1-3} and B_{1-3}, the scale bar= 35um.

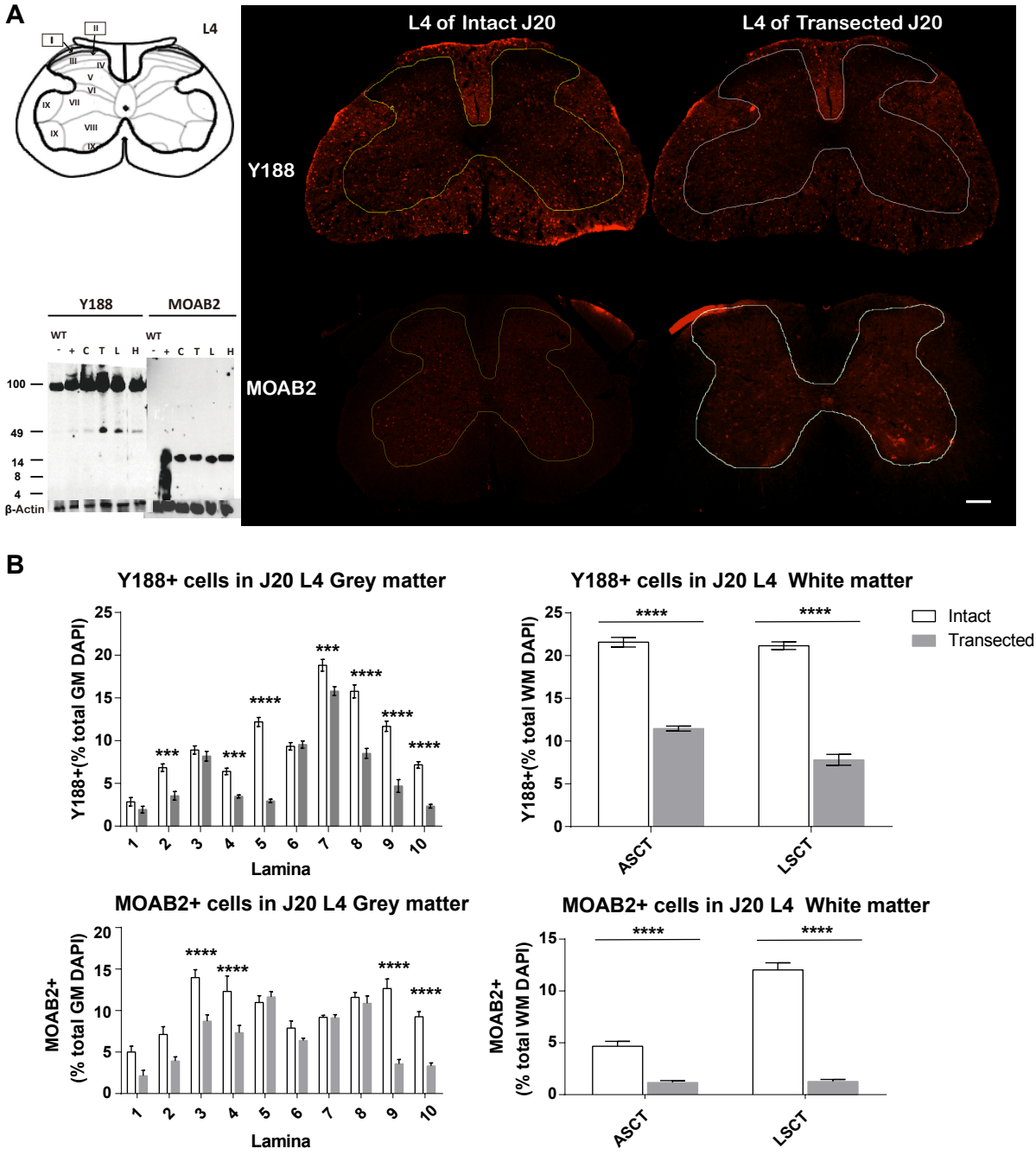

Figure 3- 8

Figure 3-8 The APP/Aβ positive cell number changes before and after the complete mid-thoracic spinal cord transection.

A) Antibody Y188 shows a specificity to the full length APP and C-terminus of APP but is not able to detect Aβs. MOAB2, on the contrast, is specific to Aβs but not immunoreactive with APP or APP C-terminus fragments (APP-CTF). The western blot result shows that Aβs

and APP/APP-CTF are increased in cervical(C), thoracic (T) and lumbar (L) spinal cord segments (WT -: protein extraction from WT hippocampus; +: purified hAPP or synthesized hAβ_{1-42}; H: protein extraction from J20 hippocampus). The distribution and number of Y188+ and MOAB2+ cells both change after the complete transection. **B)** The percentage of Y188+ cells out of the total DAPI+ cells decreased significantly in lamina II, IV, V, VII-X and corticospinal tracts. No significant change in Y188+ cell number percentage after the complete transection is detected in the lamina I and VI. For MOAB2+ cell number percentage out of the total DAPI+ cells, no significant decrease was detected in lamina I, II, V, VI, VII and VIII layer. The MOAB2+ cells also decrease significantly in the corticospinal tracts after the transection. (***: $P<0.005$, ****: $P<0.001$).

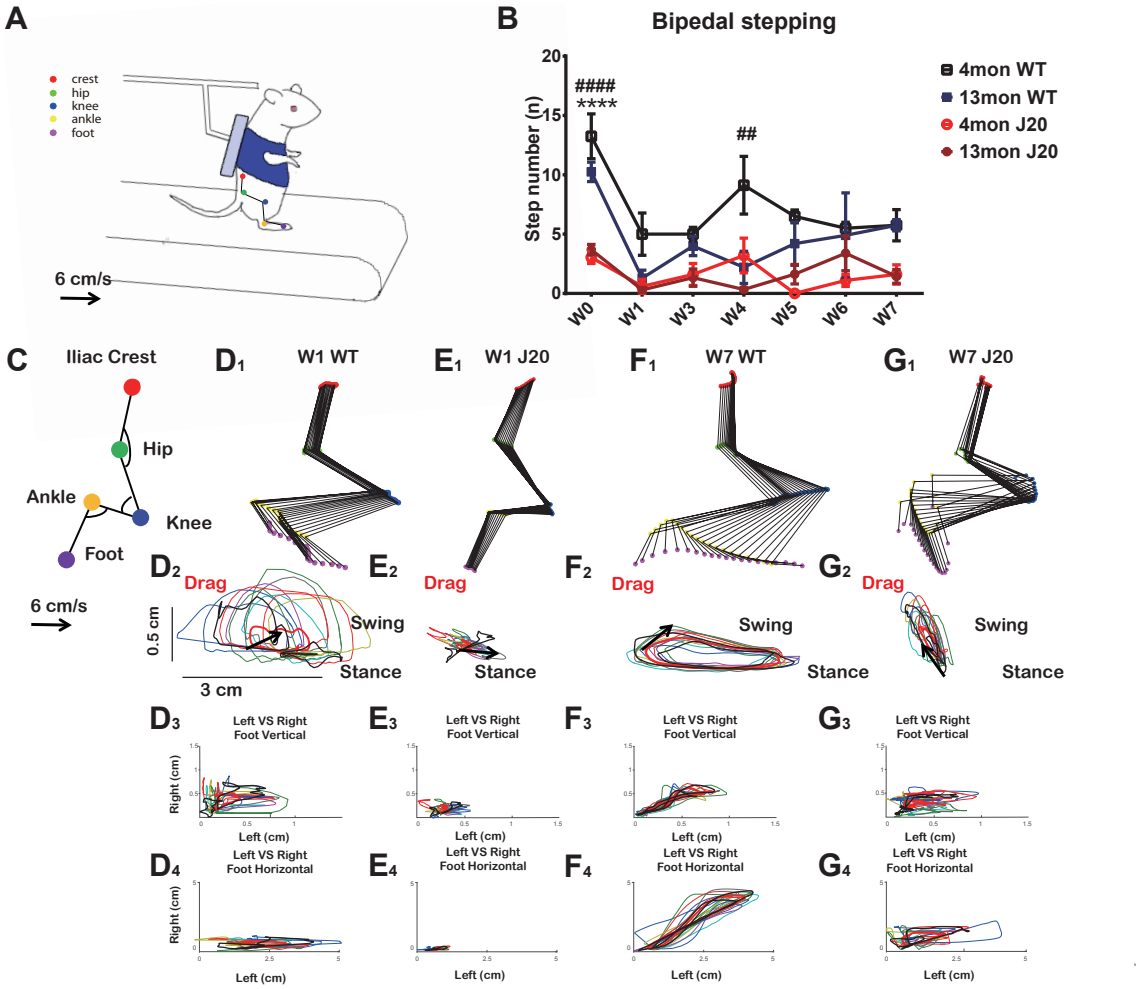

Figure 3- 9

Figure 3-9 The locomotion capability and locomotive rehabilitation were impaired in J20 mice compared to WT. (A) Schematic diagram illustrates the bipedal treadmill stepping setup. The animal was put into harness body weight support system that hindlimbs of the animal didn't need to support body weight and only respond to the sensory inputs from treadmill movements. **(B) Bipedal step capability rehabilitation curve.** The animal was tested weekly after complete spinal cord transection surgery for 7 weeks post-operation. W0 indicates the pre-operation bipedal stepping baseline. The number of coordinate bipedal step pair was counted at 5 different treadmill speeds (3cm/s, 6cm/s, 9cm/s, 12cm/s, and 15cm/s, 20s testing time bin for each speed) and the average step pair number of these 5 speeds was plotted in B. The difference between 4mon J20 and WT is indicated by # and the difference

between 13mon animal groups is indicated by * . ##: p<0.01; ****/####: p<0.001. **(C) The stick plot of hindlimb. 5 body parts were tracked bilaterally for bipedal treadmill stepping kinematics analysis. (D_{1-4}, E_{1-4}, F_{1-4}, G_{1-4}) The spontaneous bipedal locomotive function recovery in J20 was delayed compared to the recovery of WT mice.** At week-1 (W1) after ST, WT mice were able to complete several unilateral treadmill step cycles (D_{1-2}), though the left-right coordination was still impaired (D_{3-4}), J20 could not fulfill any step cycles in response to treadmill movements (E_{3-4}). At week-7(W7) after ST, WT spinal mice were able to complete consecutive bipedal treadmill steps (F_{1-2}), with left-right coordination also partially restored (F_{3-4}), while J20 could only perform unstable (G_{1-2}) and uncoordinated (G_{3-4}) steps.

CHAPTER 4: The instrumental learning model, Paw Withdrawal spinal learning paradigm, shows that APP/ Aβ overexpression affects spinal cord based learning

INTRODUCTION

In **Chapter 3**, the spinal hAPP/Aβ expression increases in AD patients (Fig. 3-3, Fig. 3-4, Fig. 3-5). The overexpression of the hAPP/Aβ in the J20 mouse lumbar spinal cord is also detected. The hAPP/Aβ overexpression in the J20 mouse lumbar spinal circuit might be correlated to the bipedal treadmill stepping defects observed in the spinal J20 mouse. In order to further investigate the influence of spinal hAPP/Aβ overexpression on lumbar spinal locomotive circuit, in this chapter, I focus on studying the plasticity changes of the spinal locomotive circuit in J20 mice.

Locomotion rehabilitation after spinal cord injury

The spontaneous recovery of the bipedal treadmill stepping capability in both the J20 and WT mice from Chapter 3 (**Fig. 3-9**) is consistent with the locomotion rehabilitation researches from our lab and other groups. These results further validate that even in the absence of any supraspinal inputs (e.g. complete spinal cord transection), the adult spinal animal can partially regain locomotive capacity with spontaneously recovery[146]. This locomotive capacity recovery depends on spinal plasticity since with repetitive training, animals can acquire complex motor tasks such as standing, stepping and adapt to perturbation[149,15097,151,152]. For example, low thoracic spinal cord transected cats, trained daily to step executed greater number of consecutive plantar steps and also had the ability to support more weight-bearing, during the bipedal treadmill stepping[146,147]. Furthermore, in complete adult spinal cats and rats that were trained to bipedally step on a treadmill when

presented with an obstacle along the path of the treadmill as a trip perturbation, they were able to reprogram/adapt their step trajectory to avoid the object[145,146,153]. These imposed motor function recovery in complete spinal animals due to training indicates the spinal networks contain the capacity of learning and memory.

Spinal learning and plasticity

Early concepts of Spinal conditioning or plasticity

Spinal plasticity related research began with focus on examining habituation of spinal reflexes as a spinal-based event. Notably, Sherrington[11,154]described the fatigue of scratch and flexion reflexes in spinal cord transected dogs. He defined fatigue as the diminished spinal reflexes as a response to repeated cutaneous stimulation at the hind limb. Multiple researches also showed that the spinal cord can undergo classical conditioning[8] . Dykman and Shurrager showed that the spinal cord was capable of motor conditioning following complete spinal cord transection in cats[155]. The motor conditioning was achieved when a weak mechanical (Sable hair brush on the fur) or electrical stimulation to the tail (conditioned stimulus, CS) is combined with a strong electrical shock (unconditioned stimulus, US) to the ipsilateral medial semitendinosus (a hind paw flexor muscle), resulting in the flexion of the hind leg (conditioned response, CR). With ~2 hours of training, some animals learned to associate CS to CR. The extinction of the CR was also evident in all the animals that learned. The existence of extinction supported that the behavior was a learned response. In another study, chronic spinal kittens given a tail pinch (CS) and tow pinch (US), showed EMG increases over training sessions in the paired group with only response habituation in the unpaired group [156].

Patterson and Thompson studying Pavlovian conditioning in the spinal cord also showed modified response for the CS-US pairing was not an outcome of habituation or sensitization at the spinal cord [157]. In an intact or acutely spinal cat, habituation is a response to weak repeated cutaneous stimuli with a diminishing amplitude of hind limb flexion reflex response, whereas sensitization or windup occurs when given the repeated stimuli increases flexion amplitude response [158]. Thompson showed during classical conditioning of the hind limb flexion reflex in acute decerebrate spinal cats, when the animals are given a shock (CS) to the skin of the thigh skin paired with a shock (US) to the tow pads of the same leg, only the paired trials resulted in significant increases in the leg flexion (CR) response to the CS, but not to unpaired stimuli [157]. Furthermore, during the extinction trials, which were conducted with increasing CS intervals, the CRs decreased over time demonstrating that the learned CR is novel in the spinal cord and it is not a product of spinal sensitization. Patterson and Thompson developed an acute spinal cat preparation under anesthesia with Flzxedil to control body and leg movements during spinal conditioning [156]. Groves and Beggs utilized this preparation to study the neural mechanism underlying the spinal conditioning, and using microelectrodes placed in the afferent terminals area or near motoneurons, they showed that the increased CR amplitude with CS-US pairing was not taking place at the afferent terminals [156] or in the motoneurons [159], but in the interneuron fields of the cord [160]. In a later study, Durkovic showed that the spinal conditioning survives with grater interval of testing following CS-US training, suggesting that the spinal conditioning is due to modification of the neurons participating in a post-tetanic potentiation driven by a mechanism of long term potentiation [161]. Durkovic and Prokowich used an NMDA receptor antagonist, D-2-amino-5-phosphonovalerate (APV), to block the induction of associative long-term potentiation during the spinal conditioning that showed no signs of reflex potentiation in spinal cat [162]. These

results demonstrated the similarities in motor adoptive response in spinal cord classical conditioning and long-term potentiation in the hippocampus.

Instrumental learning/ conditioning in absence of supraspinal inputs

Horridge demonstrated that headless insects learn new leg positioning upon stimulation as described below[163]. Horridge inserted on electrode into a hind limb flexor muscle of a headless insect, and a second grounding electrode attached to the tarsus of the same leg positioned over a saline water bath kept at a critical point (threshold). When the electrode hanging from the insect's tarsus, made a contact with saline, the insect received shocks. During the training, one insect received shock contingent on the leg position (master), while a second insect that was paired electrically to the master, received the same stimulus, but non-contingently (yoked). Horridge concluded that although the yoked received higher frequency of stimulation similar to the master, only the master insect was capable of flexing the leg to avoid the shock [163].

Instrumental conditioning in adult spinal rat was modeled after the horridge learning paradigm by Buerger and Fennessy[164], Chopin and Buerger [165] and Grau [166] to show that spinal rats can also learn to acquire and maintain a new leg position in a Pavlovian conditioning protocol. In Horridge-like instrumental conditioning, the rats whose spinal cords were completely lesioned at mid thoracic level by cauterization, began the conditioning 24-48 hrs later. On electrode inserted into the anterior tibialis (TA) muscle and a second thick-electrode (ankle electrode) placed along the flat bottom of the ankle protruding ahead of the toes, were connected to a stimulator that is connected serially to a saline bath. The vertical threshold was imposed by placing the tip of the protruding ankle electrode 4mm below the surface of the saline solution. When the ankle electrode comes in contact with the saline

solution, the completed circuit generates a shock at the TA muscle. As the ankle begins to flex, it withdraws the ankle electrode out of the saline solution breaking the circuit and halts the electrical shocks at the TA muscle.

Both Chopin and Grau used the electrically paired master and yoked animals as in the insect model as described earlier [163]. Chopin and Buerger also used this paradigm to show that the master spinal rats acquired foot flexion from 4mm to 8mm vertical threshold, where the vertical threshold was raised by 1mm increments imposed 2min of sustained foot holding above the threshold. These results showed that the spinal cord is capable of learning a new task and there is a behavioral memory component during instrumental conditioning [165]. Grau and colleagues showed that the intensity of stimulation was also critical for the learned response-outcome relationship[167]. The current required to generate a force between 0.4N-0.6N was optimal to induce learning. A stimulation current that is too low or too high, producing a force (0.2N or 0.8N respectively), resulted in habituation. Crown and Grau[168] proposed that the yoked animal's inability to learn is not a consequence of poor performance but an acquired learning deficit due to the non-contingent shock inducing a greater habituation[167]. Furthermore, when the ipsilateral or contralateral hindlimb of previously trained master or yoked was retested under the contingent shock condition, only the master reacquired the learning task in either of the hindlimbs. Grau suggested that transference memory from prior exposure facilitated the learning in the master while the prior learning deficit inhibited the subsequent learning in the yoked group[169].

Mechanisms of in spinal cord instrumental learning

Grau and colleagues demonstrated through pharmacological studies that induction and maintenance of spinal learning under the master or controllable shock conditioning required

facilitation through the NMDA and AMPA receptors pathway [166]. For example, intrathecal delivery of the competitive NMDAR antagonist AP5 or competitive AMPAR antagonist CNQX (6-cyano-7-nitroquinoxaline-2,3-dione), into the spinal cord before or towards the end of the 30 min contingent shock learning, dose dependently blocked the induction and maintenance of hindlimb flexion, respectively.

Gomez-Pinilla in a collaboration with Grau's group [170,171] showed that instrumental learning in spinal master rats was impaired by AIP (a myristoylated form of Autocamtide-2-Related Inhibitory Peptide (AIP), a highly potent and specific substrate competitive inhibitor of CaMKII), demonstrating the CaMKII is also critical in spinal learning [168]. Furthermore, in the lumbar spinal cord segments of rats that were given contingent shocks (master condition), the levels of BDNF, CaMKII, CREB, and Synapsin I mRNA were significantly increased when compared to the rats that received uncontrollable shocks (Yoked) and in spinal rats that did not receive shocks (unshocked control). Blocking the BDNF pathway with TrkB IgG also inhibited the learning, further showing the importance of BDNF in this instrumental learning [171]. In a subsequent study, Huie et al demonstrated the rescue of spinal learning following intrathecally delivered BDNF protein in rats that were preconditioned with the uncontrollable shock [171]. In a maladaptive conditioning of the injured spinal cord, using the intermittent noxious tail stimulation in SCI rats showed reduction of DBNF, TrkB, CaMKII, ERK1/2 protein at 1hr, 24hr, and 7-day after stimulation in the dorsal horn [26]. The BDNF has been implicated in various roles such as glutamatergic signaling, NMDA receptor activity, GABAergic signaling, and in learning related synaptic transmission. In hippocampus and spinal cord, BDNF is upregulated due to activity and promotes learning and memory [172].

Paw withdrawal Learning Paradigm (PaWL): the instrumental learning paradigm in mouse

In an attempt to understand the synaptic mechanisms involved in the performance of motor tasks in J20 mice, we adopted a simple model of learning in the rat paw withdrawal learning (PaWL) to the hind limbs of mice[173] . As shown **in Fig. 4-1**, in PaWL paradigm, spinal mice dorsiflex the hind paw in response to position-dependent mild electric shocks to the anterior tibias muscle and learn to hold the paw to minimize the net exposure to shocks. Although anterior muscle and learn to hold the paw to minimize the net exposure to shocks. This simple *in vivo* learning model provides an opportunity to identify molecules and neural pathways that mediate spinal learning in the mouse spinal cord, utilizing genetic and molecular tools of key learning-associated signaling molecules in the brain[26] . A summary of the learning-associated markers in instrumental learning of adult spinal rodents is shown in **Table 4-1**.

Because research evidences support that APP and Aβ over-expression impair both neural plasticity and learning/memory in the cortical and hippocampal circuit, I hypothesize that the hAPP/ Aβ overexpression in J20 mice affects the spinal learning performance in PaWL by affecting the activation and expression of learning/plasticity related proteins. To test this hypothesis, I aim to answer the following 3 questions:

1) **Is the PaWL paradigm sensitive enough to evaluate the spinal circuit changes in J20 mice?**
2) **If the J20 and WT mice perform differently in PaWL paradigm, is the difference specific to spinal cord circuit alternation?**
3) **Is the lumbar hAPP/Aβ expression levels correlated to PaWL performance?**

Learning associated maker	Action	Pharmacological agent	Master	Yoked	Intermittent noxious shock	Reference
Protein Synthesis	inhibitor	Cycloheximide, Anisomycin	blocked learning	blocked yoked inhibition	blocked learning deficit	Patton et al., 2004, Baumbauer et al, 2006
NMDA	inhibitor	AP5, MK-801	blocked learning	N/A	blocked learning deficit	Ferguson et al, 2006; Joynes et al, 2004
PKC	inhibitor	PKC inhibitor	N/A	N/A	blocked learning deficit	Ferguson et al, 2008
CaMKII	inhibitor	AIP	blocked learning	N/A	blocked learning deficit	Baumbauer et al, 2006, 2004; Gomez-Pinilla et al 2007
BDNF	Inhibitor	TrkB IgG	blocked learning	N/A	blocked learning deficit	Gomez-Pinilla et al 2007, Huie et al, 2005, 2013
AMPA, mGluR1 blocker	inhibitor	Naspm trihydrochloride	blocked learning	blocked yoked inhibition	blocked learning deficit	Ferguson et al, 2008; Huie et al, 2015
AMPA	inhibitor	CNQX	blocked learning	N/A	blocked learning deficit	Hoy et al, 2013,
CaMKII level	Measured mRNA	RT-PCR	Increased	Decreased	N/A	Gomez-Pinilla 2007
BDNF	Protein	Western,	Increased	Decreased	Decreased	Huie, 2005, 2013, Gomez-Pinilla et al 2007; Garraway et al 2011
BDNF level	mRNA	RT-PCR	Increased	N/A	N/A	Gomez-Pinilla et al 2007, 2002

Table 4- 1

Table 4-1: Learning-associated molecular markers in instrumental learning in adult spinal rodents.

MATERIALS AND METHODS

Animal Groups

All animal studies were performed according to protocols examined and approved by the Animal Use and Care Committee of University of California, Los Angeles. The J20 transgenic mouse and their littermate C57BL/6 WT control mice were further separated into two groups by 4mon (4mon J20 n=7, 4mon WT n=8) and 10-13 month age (10-13mon J20 n=13, 10-13mon WT n=10), of ~26-45g body weight were used for PaWL experiment.

Complete mid-thoracic spinal cord transection surgery

The spinal cord was completely transected at the T7–T9 vertebral level in all mice as described previously. Briefly, under 2% isoflurane anesthesia, a dorsal midline skin incision was made from T6 to T9 and the musculature covering the dorsal vertebral column was retracted to expose the spinal lamina. A partial laminectomy of the T7 and T8 vertebrae was performed to expose the spinal cord. The spinal cord, including the dura, was transected completely using microscissors. The completeness of the lesion was verified by separating the cut ends of the spinal cord with small cotton pellets and by passing a fine glass probe through the lesion site. The skin incision was closed using small surgical staples.

After surgery, the wound sites were treated with triple antibiotic ointment (Bacitracin) and the mice were given lactated Ringer's solution (1.5 ml/30 g body weight, s.c.). Because preventing leg extension during recovery has been shown to facilitate subsequent learning in rats, both hindlegs were bound with the knee and ankle joints fully flexed until PaWL testing. The mice recovered in an incubator maintained at 37°C until fully awake and then were

returned to their home cages. The mice were allowed to recover for 24hr before PaWL testing. To minimize bias, the surgeons and testers were blind to the diet and exercise conditions during surgery and PaWL testing.

Paw Withdrawal Learning Paradigm (PaWL) Procedure

PaWL experimental setup

The PaWL test was conducted 24 h after the spinal cord transection surgery on mice. The details of the PaWL testing for mice have been described previously. Briefly, during testing the mice were restrained in a closed cloth harness with two slots cut at the end of the harness to allow for both hind legs to hang freely (**Figure 4-1A**). Two fine-wire hook electrodes were constructed by removing 1 mm of insulation at the end of nylon-coated single strand stainless steel wires (California Fine Wire Co., Grover City, CA). Each wire was passed through a 32-gauge needle: one electrode was inserted intramuscularly into the left TA muscle and the second electrode was inserted subcutaneously at the base of the lateral malleolus on the same side to serve as a ground. The electrodes were attached to a stimulator (S88, Grass Product Group; W. Warwick, RI), through a stimulus isolation unit (SIU5; Grass Product Group) and a constant current isolation unit (CCU1; Grass Product Group). A stimulus duration of 50msec followed by a 10msec delay between consecutive pulses was used throughout the PaWL test session as previously described.

The experimental (Master) and control (yoked) pairing in PaWL

Preparation of mice for PaWL began ~20-22 hrs after the spinal cord complete transection surgery (ST), while the PaWL procedure was conducted ~24hr as described before[171]. One hindpaw of the Experimental mouse (Master) is exposed to a contingent stimulus protocol,

where the mouse receives a stimulus whenever the fifth metatarsal-phalangeal (MTP) joint drops below the y-coordinate of the set threshold (**Fig 4-3. B**). When the paw falls below the determined vertical threshold, a constant current square wave monopolar electrical shock is delivered at ~20 Hz with the working cycle of 10% to the anterior tibialis muscle until the paw is dorsiflexed above threshold. A second mouse is electrically coupled (Yoked) to the Master mouse, and receives the shock irrespective of its paw position. The leg stimulus of the Master and Yoked mouse are described as contingent (controllable stimuli), and non-contingent (uncontrollable stimuli), respectively.

Determination of stimulus intensity

For each animal, the force generated at the ankle dorsiflexion following electrical stimulation was measured through a series of increasing currents (0.10mA), until the maximum and supramaximal force was realized. From each force curve the optimal current producing a submaximal contraction was determined by taking the 2/3 the maximal force and its correlated current. To do so, a #4 surgical Silk tread was tied across the paw on the hindlimb with implanted stimulating electrodes. The #4 sild thread was then attached to the force transducer (Dual Mode Muscle Lever 300BLR, Aurora Scientific Inc., Aurora, Ontario, Canada). Force resulting from a series of single 50ms square-pulse stimuli from 0 to 3.0mA, increments of 0.10mA, with a 30 sec delay between each stimulus, were recorded and displayed by a custom written LabVIEW program. When the stimulus series was completed, the thread was removed from the foot. Force was recorded for each increment step of the current. The force curve was generated via delivery of a single 50 ms stimulus every 30sec to the TA muscle (**Fig. 4-2**). In majority of the experiments, a current of 0.20-0.30 mA generated 0.6N of force at the ankle during paw dorsiflexion for both J20 and WT mice.

Digitizing the foot position

Acquisition of the two-dimensional foot position was accomplished by digitizing the white mark placed on the MTP with a video-based point tracking system (CMUCam2; Carnegie Mello University). The CMUCam2 performs automatic, hardware-based point tracking of region fitting user-specified color and size criteria and reports the centroid of the region to the computer. The LabVIEW (National Instruments, Inc., Austin, TX) software was used to control the CMUCam2 and collect tracking data streaming from the camera. The software then calculated the range of color associated with the marker and because of the hight-contrast (white on a black background), resulted in accurate tracking points. Once the desired parameters were established, they were used to configure the point tracking by the CMUCam2 and the LabVIEW software. The camera has a field of view of 15mmX15mm, or a resolution of 8 pixels/mm, positioned 40mm away from the foot. Following the stimulation parameters (Force curve) was set the acquisition of foot position and, a resting MTP position was determined after 3 priming stimulations. The vertical threshold was assigned based on the post-primed foot position. A threshold of 1.5mm above the resting position, was set for both the master and yoked mice with a threshold parameter in the LabVIEW program. The paw withdrawal test began with the initiation of the stimulator for 30min, set to the stimulus parameters consisting of a 50ms square wave pulse followed by a 10ms delay between consecutive impulses.

Response Duration

The spinal cord learning over the 30 min of the PaWL testing was measured as response duration (RD), calculated according to the equation below. The response duration takes into account the number shocks (measured as a foot flexion response) during the binned time.

Response Duration (min)

= (60sec-time the paw was below the threshold)/(number of responses+1)

The numberator represents the time the paw is above the imposed threshold. The number of paw flexion or responses are the results of shocks received when the paw was extended below the threshold. Given the length of stimulus pulse duration (50ms) followed by a 10ms built-in delay, the maximum possible stimulation frequency is 16.7Hz and minimum is zero during period of paw hold greater than 60sec. To eliminate the possibility of zero in the denominator, the total number of response for each minute binned is increase by 1. For example, during a one minute period where 1 response will yield RD =29.996min, for 2 responses RD = 19.967 min and for 5 response RD=9.967 min. To obtain a response duration curve, the calculated response duration for each binned min (y-axis) was plotted as a function of time (x-axis), over the length the 31 min experiment (**Figure 4-4. A**).

Tissue Preparation

To ensure time for maximal Fos levels in the spinal cord, the mice were returned to their cages and perfused 60 min after the PaWL test. Animals were anesthetized with pentobarbital (100mg/kg i.p.) approximately 5min before perfusion. The animals were perfused transcardially with cold 4% paraformaldehyde (PFA) in phosphate buffered saline (PBS, Sigma, St. Louis, MO) under deep anesthesia with approximately 150 to 200ml 4% PFA for 15-20 min. After the perfusion, the spinal cord and brain were dissected, rinsed with 1xPBS and placed in a 30% sucrose for cryoprotection for 4-5days. With the dorsal root ganglion of L5 as a landmark, the spinal cords were divided into T13-L2, L3-L5, and L6-S2 blocks. The tissue blocks were then embedded in Richad-Allan Neg50 frozen section medium (Thermo Scientific, Hudson, NH), and stored at -80^{o}C until ready to cut. The spinal cord blocks were

cryosectioned serially at 35μm thickness and collected in sequence as free floating sections in 1XTBS with 0.02% sodium azide (Sigma). The sections were stored at 4 ^{o}C.

Immunofluorescent staining (IF)

IF staining with anti-c-Fos (1:400, SC7202, Santa Cruz Inc., CA) and CaMKII (1:500, 6G9 clone, Millipore, CA) was used to identify acitivated CaMKII neurons (CaMKII+/Fos+) in the spinal cord. For the analysis of segmental distribution of activated spinal neurons, we used 5-8 sections each from L1-S2 lumbar segments. We counted Fos+, CaMKII+/Fos+ neurons in 8-12 sections in all lamina of L5 segments to provide an adequate sampling of activated spinal neurons. The secondary antibodies, anti-rabbit Dylight 594 1:500 and anti-goat FITC 1:500 (Jackson ImmunoResearch Laboratories, Inc., West Grove, PA) were used for staining visualization. All the stained slices were mounted on Fisher Superfrost slides (Fisher Scientific, Pittsburg, PA) and cover slipped with VectorShield mounting media with DAPI (Vector Labs, Burlingame, CA).

Image analysis

Spinal cord sections processed for fluorescent staining were examined by Zeiss (Axiophot) microscope under the appropriate fluorescent filter sets. Digital images of neurons labeled with Fos, Dapi, and CaMKII were acquired by using a Spot RT CCD Slider monocolor camera (Zeiss) and the Axio image analysis program (Zeiss). Composite images of Fos, DAPI and CaMKII were created through the Axio imaging program. Lamina borders were drawn onto spinal cord sections with tagged neurons according to the spinal cord atlas of the adult mice (Watson et al., 2009) and the numbers of activated neurons in individual spinal cord lamina were counted. The number of activated CaMKII+ neurons in lamina IV-VI was calculated as a percent of the total activated (Fos+) cell number.

Analysis of CaMKII immunoreactivity in the dorsal horn in L3-L6 lumbar segments

In L3-L6 lumbar segments, five spinal cord sections from each segment stained with CaMKII antibody were selected for optical density measurements. The region of interest (ROI: dorsal horn) was outlined manually on the saved images and the surface area of objects identified above background threshold was measured. The optical density of CaMKII immunoreactive signal was presented as the percentage of the total object area divided by corresponding area of the ROI.

Generation of heat maps

Fos+ nuclei and CaMKII+ cells were manually tagged using manual tag feature of the Axio program. The tagged coordinate points were imported to Excel that translate the coordinate points into a spreadsheet grid that represented the distribution of Fos+ and CaMKII+ cells. The spinal cord section was then divided into a 80X50 grid matrix. Grid values indicate the number of nuclei counted in the particular frame. A color gradient was applied based on the value in each grid frame. A heat map color gradient was adjusted according to the value range. A diagram of the cell distribution in different lamina of each individual spinal cord segment was superimposed on each heat map to quantify the number of Fos+ and CaMKII+ found in each lamina. A macro for heat map was generated by Kevin Truong in Reggie Edgerton's lab. To calculate the % of total Fos+ and CaMKII+ cell number in each lamina on ipsi- and contralateral side of the PaWL stimulation, the number of Fos+ and CaMKII+ in each lamina was presented as the percentage of the total number of Fos+ or CaMKII+ in ipsi and contralateral sides respectively.

ELISA and Western Blot

Fresh-frozen spinal cords were homogenized in 110 mgml-1 in 2% w/v sodium dodecyl sulphate (SDS) in water with protease inhibitors (Roche) to recover soluble amyloid. The sample was then centrifuged and the pellet homogenized in 70% formic acid in water to obtain the insoluble amyloid fraction. Homogenates were spun at 100,000g for 1h. Supernates were diluted in buffer EC (0.02M sodium phosphate, pH 7.0, 0.2 mM EDTA, 0.4M NaCl, 0.2% bovine serum albumin, 0.05% CHAPS) on ice. To obtain the soluble amyloid fraction and protein for western blotting, frozen spinal cord were homogenized in cell lysis buffer (Cell Signaling), sonicated briefly and centrifuged at 14,000 r.p.m. for 10 min. Aβ42 was measured by ELISA (Covance) following the manufacturers protocol. Immunoblotting was performed using the following polyclonal antibodies C-terminal APP (Calbiochem).

Statistics Data analysis

Data analyses were performed with two-way analysis of variance with age and genotype as independent variables. In all cases, $P < 0.05$ was considered to be statistically significant. Statistical comparisons of learning between groups across time (binned min) during PaWL test and interaction between group affect over time were determined using a Repeated Measure two-way ANOVA. Sadik multiple group post-test was conducted to show statistically significant differences between Master and Yoked group over time (**Fig. 4-4 A, C**). Total response duration between Master and Yoked were compared using the paired Wilcoxon Test (**Fig. 4-4 B, D**). To quantify the rate of learning in the master group, Boltzmann Curve fit analysis was performed. The confidence bands (dotted lines) indicate the likely location of the true fit cure (**Fig. 4-4 A, C**). The maximum response duration of the curve fit is reported and the rate of learning was determined by taking the time at half-the

maximum (T_{50RD}) of the response duration curve. All analyses were performed using GraphPad 6.0 (GraphPad Software Inc. San Diego, CA). The level of significance was selected as $P<0.05$ for all comparisons. Data are reported as the mean values ± standard error of the mean (SEM)

RESULT

No significant difference was detected between the force-stimulation current curve between J20 and WT TA muscle.

The force-stimulation current curve was tested before each PaWL to obtain the optimal stimulation current intensity, which induces submaximal TA contraction force (**Fig. 4-2**) to avoid the occurrence of muscle fatigue in PaWL test. The force-stimulation current curve also allowed us to compare the muscle contraction strength under the same stimulation current intensity. The force-current curves of J20 and WT mice were compared to investigate whether the muscle strength of TA muscle in J20 is different from that in WT mice (**Fig. 4-3**). No significant difference between the two force-current curves was detected under any tested stimulation current intensity. This result indicated that the contraction strength of TA muscle in J20 and WT mice did not show significant difference when compared to each other.

Successful instrumental learning was induced in 4mon J20 and WT master mice through PaWL Paradigm. The PaWL response duration curve of 4mon J20 indicated a delay in spinal learning when compared to WT mice.

The 4mon WT Master mice were able to acquire the new paw position while the yoked paw remained extended. The repeated measure two-way ANOVA comparison showed significant difference in response duration between Master the Yoked group ($F(1,6)=21.19$, $P<0.01$),

with significance temporal differences over 30min test period ($F(29,174)=2.689$, $P<0.0001$) and interaction of Master vs. yoked group difference over time of the test ($F=(29, 174) = 3.672$, $P<0.0001$). The Sidak post-hoc test between group and over time showed, that the first significant difference of the response duration between the Master vs Yoked began at the 8-9 min and then continued from 11 to the 30 min (**Fig. 4-4 C**). The comparison between mean total response duration between matched pairs of Master and Yoked animals showed the Master group with significantly greater mean then that of the Yoked group (**Fig. 4-4D**, Wilcoxon Test $P<0.05$).

The 4mon J20 mice in the master group also learned to hold the paw above the 1.5mm threshold line while the paired yoked group did not (**Fig. 4-4A, Fig. 4-4B**). A repeated Measure two-way ANOVA analysis showed that master J20 mice significantly differed from the yoked group ($F(1,6)= 19.45$, $P=0.0045$), with significant differences over time ($F(29, 174)=4.213$, $P<0.0001$) and the interaction between the master and yoked 4mon J20 groups over time ($F(29, 174)=3.69$, $P<0.0001$). The Sidak post-hoc test showed that the first significant difference between master and yoked 4mon J20 began at the 15^{th} min and the continued to the 30^{th} min (**Fig. 4-4A**). The total response duration between matched pairs of master and yoked J20 mice was also significantly different (Fig. 4-4 B. Wilcoxon Test, $P<0.05$).

To compare the rate of spinal learning, the Boltzmann's curve fit analysis was performed to identify the time at which half-the-max (T_{50RD}) response duration for 4mon J20 and WT mice. With the curve fit, the Top RD (maximum curve fit response duration value) for 4mon J20 and WT mice, were 51.89 sec (**Fig. 4-4A**) and 53.61 sec (**Fig. 4-4C**), while T_{50RD} was 15.67

and 4.98 min, respectively. These results showed that the 4mon WT mice learned paw holding task faster than the 4mon J20 mice.

Both 4mon and 13mon J20 mice groups demonstrated instrumental learning deficits in PaWL paradigm.

When the 4mon and 13mon WT Master group mice showed significantly greater response duration mean and smaller T_{50RD}, compared to the their coupled Yoked groups, 4mon and 13mon J20 mice didn't show significant difference when compared to their coupled Yoked groups. Both 4mon and 13mon J20 Master mice showed significant decreases in PaWL response duration compared to 4mon and 13mon WT groups ($F(1,7)=24.41$, $P<0.01$) at the 14-31min during the testing (**Fig. 4-5 B**). Moreover, both 4mon and 13mon WT mice reach their half-the maximum response duration earlier than J20 mice from both groups, while in both genotypes, the 4mon mice reach half-the maximum response duration slightly earlier than the 13mon mice. (13mon J20, n=12, T_{50RD}=22.01min; 4mon J20, n=7 T_{50RD}=19.68min; 13mon WT, n=8, T_{50RD}=15.28 min; 4mon WT, n=8 T_{50RD}=6.16min). This prolonged T_{50RD} as well as the decreased Response Duration value amplitude both suggested the instrumental learning in PaWL was impaired in J20 Master mice group.

Negative correlation detected between the Response Duration percentage and lumbar spinal hAβ expression levels.

To investigate if the spinal hAβ contributes to the previously observed instrumental learning in PaWL, the lumbar L2-L5 spinal cord were harvested from 4mon and 10mon J20 as well as WT mice groups after PaWL test. The expression level of lumbar spinal hAβ42, the main component of amyloid plaques, results from ELISA analysis was negatively correlated with the PaWL response duration percentage. The lumbar spinal hAβ42 amount and PaWL

response duration from J20 Master group showed a strong negative correlation (r=-0.72314) (**Fig. 4-5C**). Furthermore, the contingency analysis showed the lumbar hAβ – Response Duration Percentage correlation scatter points of WT Master group and J20 Master fell into different cluster (Chi-square, $P<0.01$). These results showed that the high L3-L6 hAβ42 amount correlated with the PaWL response duration decrease.

The PaWL activated cells number was the highest in the lamina V and was also directly correlated with the degree of PaWL in the master WT mice.

As shown in **Fig. 4-4**, only the master group animals, J20 or WT, successfully learned to maintain the shocked leg in a flexed position to minimize the net shock exposure. The spinal cord tissues of mice terminated 60min after PaWL were subjected to c-fos staining, in order to identify the activated cells expressing the neuronal-early-activity marker, c-fos (**Fig. 4-6A**). The number of activated neurons (Fos+) was significantly higher in the ipsilateral compared to the contralateral spinal cord, in both the master and yoked mice (**Fig. 4-6B, C**). L4 level, where the motor units of TA muscle are located, had the highest Fos+ cells when compared to any other lumbar spinal segments (data not shown). Taken together, the total Fos+ cells number in all lamina of the ipsilateral half of the master and yoked spinal cord was similar, but the master mice showed a trong negative correlation between the total Fos+ and the response duration of PaWL (**Fig. 4-6D**). Although the Fos+ in the ipsilateral individual lamina showed similar distribution between respective spinal lamina in both master and yoked mice (**Fig. 4-7A**), the Fos+ in lamina II (**Fig. 4-7B**) and IX (Fig. 4-7C), were negatively correlated while the lamina V (**Fig.4-7D**), showed a strong positive correlation with degree of learning in master mice only. Lamina V contained the highest Fos+ cell number in all spinal lamina in the stimulated side of the spinal cord from both the master and

yoked animals (**Fig. 4-7A**). Combination of lamina IV-VI also showed a strong positive correlation (R=0.87) with the response duration of learning.

CaMKII expression was elevated in ipsilateral IV-VI lamina layers in the master WT mice

CaMKII immunoreactive terminals were the most highly detected in the ipsilateral lamina layers I-III (**Fig. 4-8A**), with many strongly labeled CaMKII+ cell bodies in medial IV-VI (**Fig. 4-8B, C**). Comparison of CaMKII+ staining in the L3-L6 segments showed that in both master and yoked mice, CaMKII+ staining in the ipsilateral DH is stronger than the contralateral side (**Fig. 4-8D**). Of all the lumbar segments, the master WT mice contained significantly higher levels of CaMKII immunoreactivity in L4 dorsal horn (**Fig. 4-8D**).

DISCUSSION

PaWL is a simple and robust model for spinal learning and spinal circuit plasticity measurement.

The biggest advantage of PaWL paradigm is that this behavioral model enables us to semi-quantitatively evaluate the lumbar spinal circuit specific plasticity and spinal learning *in vivo*. As shown in Fig. 4-4, instead of simply defining the learning results into the binary catalogs "learned" or "not learned", analyzing the PaWL paradigm response duration curve allows us to further evaluate the spinal learning quality in a more linear manner. PaWL features, such as the earliest time point that the tested animal shows sign of learning, how fast the test animal learn to hold its paw position, how many times the animal fail and the percentage of successful response during the 30min test durations can all be measured to reflect different

spinal circuit changes, which might contribute to spinal learning and plasticity. This advantage also makes the PaWL paradigm a very powerful tool for detecting the subtle and gradual changes in the spinal cord of AD model animal (J20 in this study) as well as in other neurodegenerative disease animal models (e.g. ALS, MS, etc.)

Furthermore, because PaWL paradigm tested the spinal circuit, which only controls one TA muscle contraction (The stimulated side TA). This simple model of spinal learning allows us to dissect the neural circuit and investigate the underlying mechanisms associated with locomotion control with a simpler and clear scope before we move onto investigate the network with more neural components in more complicated motor tasks.

Number of activated neurons in the master WT mice correlates with the degree of learning.

While the total number of Fos+ cells were similar between the master and yoked WT mice, differences in distribution patterns of Fos+ cells in specific spinal lamina, as well as the correlation between the distribution patterns and the degree of learning were observed between master and yoked WT mice. The negative correlation of total Fos+ cells number with the PaWL learning quality suggests that cells in more lamina layers are activated when the animal doesn't learn well. When the cell activation is more focused, the better animals learn. The further analysis of the correlation between cell activation in different lamina layers with the PaWL quality shows that lamina II and IX are negatively correlated to PaWL quality. The activation of lamina II cells indicates an increase in nociceptive stimuli through pain-related afferents, which is caused by the increased number of shocks in PaWL. Unlike lamina II and IX, number of Fos+ cells in lamina V was positively correlated with degree of PaWL, only in master WT mice. These lamina V cells may be responding to proprioceptive cues of

the paw position. Since CaMKII is an important learning marker in cortical/ hippocampal based learning, CaMKII has also been shown to be important in PaWL in rats, the CaMKII expression was also examined in these Fos+ cells.

Activated CaMKII terminals in lamina I-III and CaMKII+ cell bodies in lamina IV-VI

The ipsilateral CaMKII immunoreactivity was highest in the L4 segment when compared to the other segments of the lumbosacral spinal cord. L4 is where the majority of the TA motorneurons and interneurons are located, suggesting that the L4 CaMKII expression level changes might related to the PaWL learning-associated changes. We found cell bodies with strong CaMKII expression are located in lamina IV-VI region in L4, and the master WT mice showed significant increase in CaMKII+ cell number in IV-VI in L4 sections compared to the yoked ones.

Interestingly, in **Chapter 3**, we showed that the complete spinal cord transection did not affect the intracellular hAβ expression in the lamina I-II, V-VIII layers. Moreover, high hAβ expression was detected in lamina V and VIII regions after the complete transection (**Fig. 3-7**). This overlap of the PaWL learning-related CaMKII+ cells distribution pattern in WT master mice and the potential spinal hAβ but not hAPP distribution pattern in J20 mice suggested that it is the hAβ but not hAPP that affects the CaMKII based spinal learning. The negative correlation between L3-L6 lumbar hAβ expression level and the PaWL learning quality (**Fig. 4-5C**) provides further support to this hypothesis.

Thus, in **Chapter 5**, I delivered the gamma-secretase inhibitor, LY411575, to acutely block the generation of hAβ and evaluate the qualities of quadrapedal treadmill stepping, bipedal treadmill stepping and PaWL learning after lumbar hAβ expression level is down regulated.

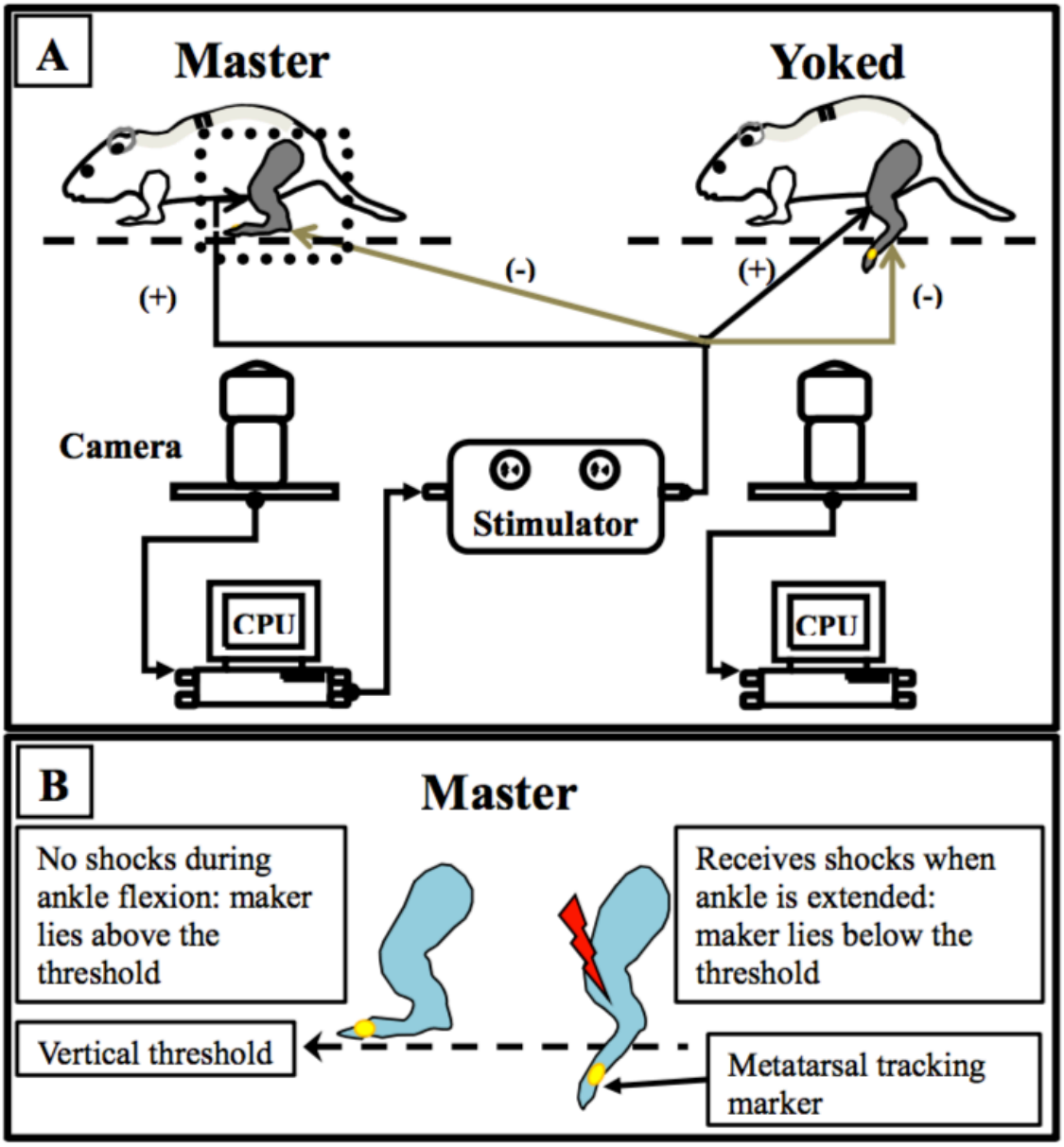
A
Master
Yoked
(+)
(-)
(+)
(-)
Camera
Stimulator
CPU
CPU
B
Master
No shocks during ankle flexion: maker lies above the threshold
Receives shocks when ankle is extended: maker lies below the threshold
Vertical threshold
Metatarsal tracking marker

Figure 4- 1

Figure 4-1: Schematic diagram illustrating the PaWL setup. (A) The setting of coupled Master and Yoke mouse. The stimulator is connected to both master and yoked animals in parallel. Both the master and yoked computers record the paw position in real time for subsequent analysis but only the Master mouse receives shocks dependent on the paw position. The Yoke animal receives shocks whenever the Master mouse receives shocks, regardless of Yoke animal's paw position**. (B) The setting of the Master mouse.** High frequency camera capture the paw position for the LabVIEW software to track the metatarsal marker and generate a signal to the stimulator when the paw position is below the threshold line y-coordinate, which is set at 12mm higher than the natural hanging position y-coordinate.

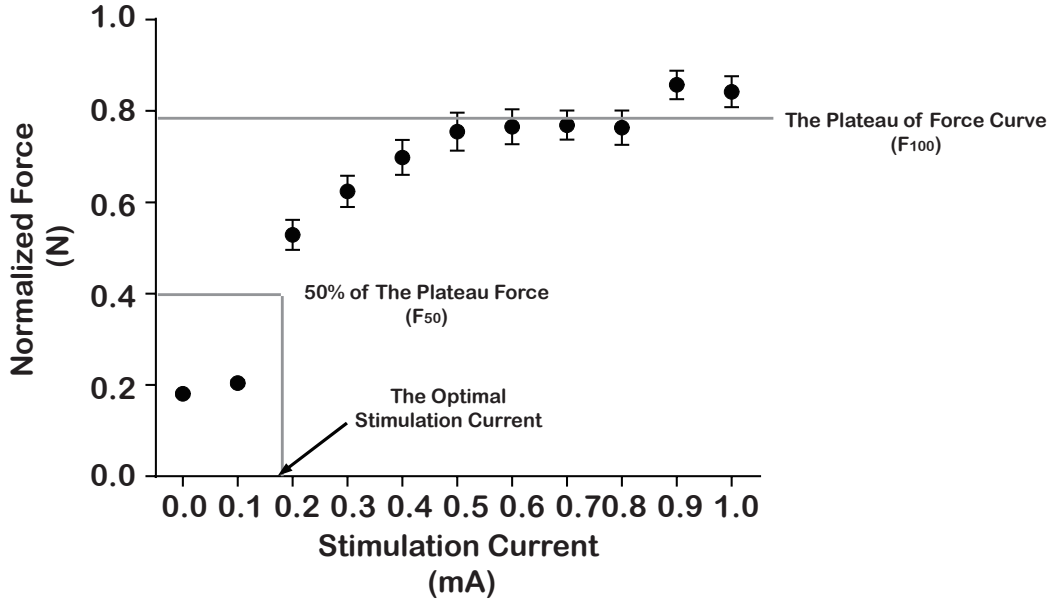

Figure 4- 2

Figure 4-2 Force – current curve for optimal stimulation current intensity identification.

A force-current curve was generated before PaWL to determine the optimal stimulation current intensity to obtain a submaximal force. The forces induced by the same stimulation current intensity were pool together, normalized, and averaged among all the tested, same genotype animals. The normalized Force-current curves for J20 and WT mice were generated separately. The optimal stimulation current was calculated as the current that induced 50% of the plateau force (maximum force). The optimal stimulation current of WT was defined as 0.2mA, which induced approximately 0.4N of force.

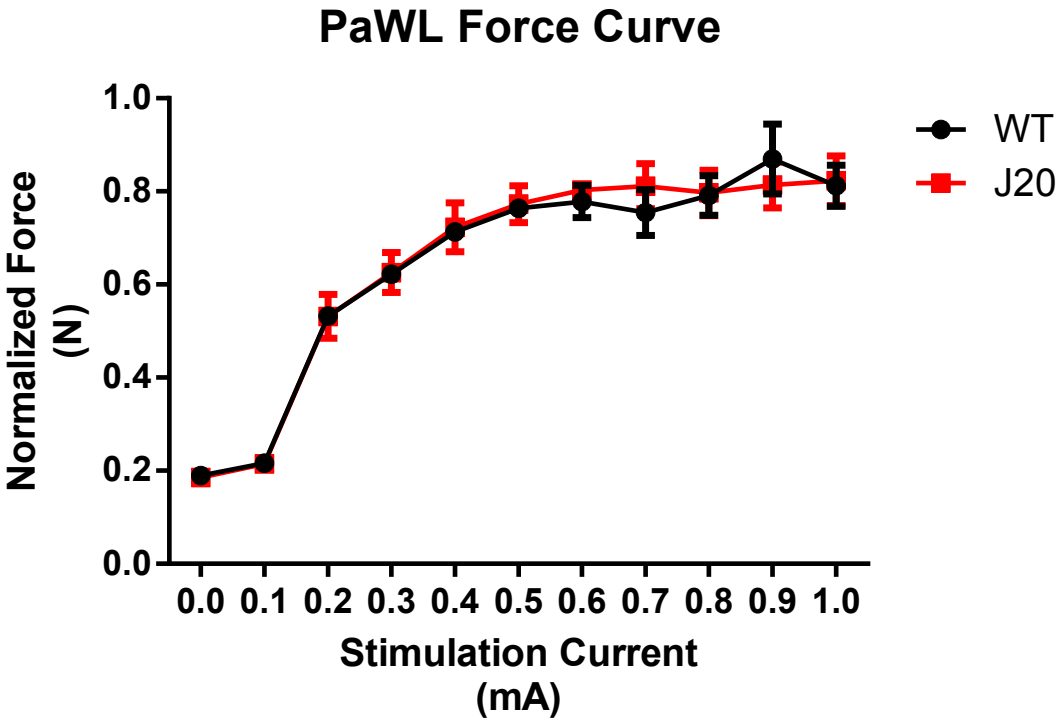

Figure 4- 3

Figure 4-3 The force-current curve for J20 and WT mice

No significant difference was detected between force-current curve of the J20 (n= 36) and their WT littermates (n=33). The optimal stimulation intensity of J20 and WT groups were both set at 0.2mA.

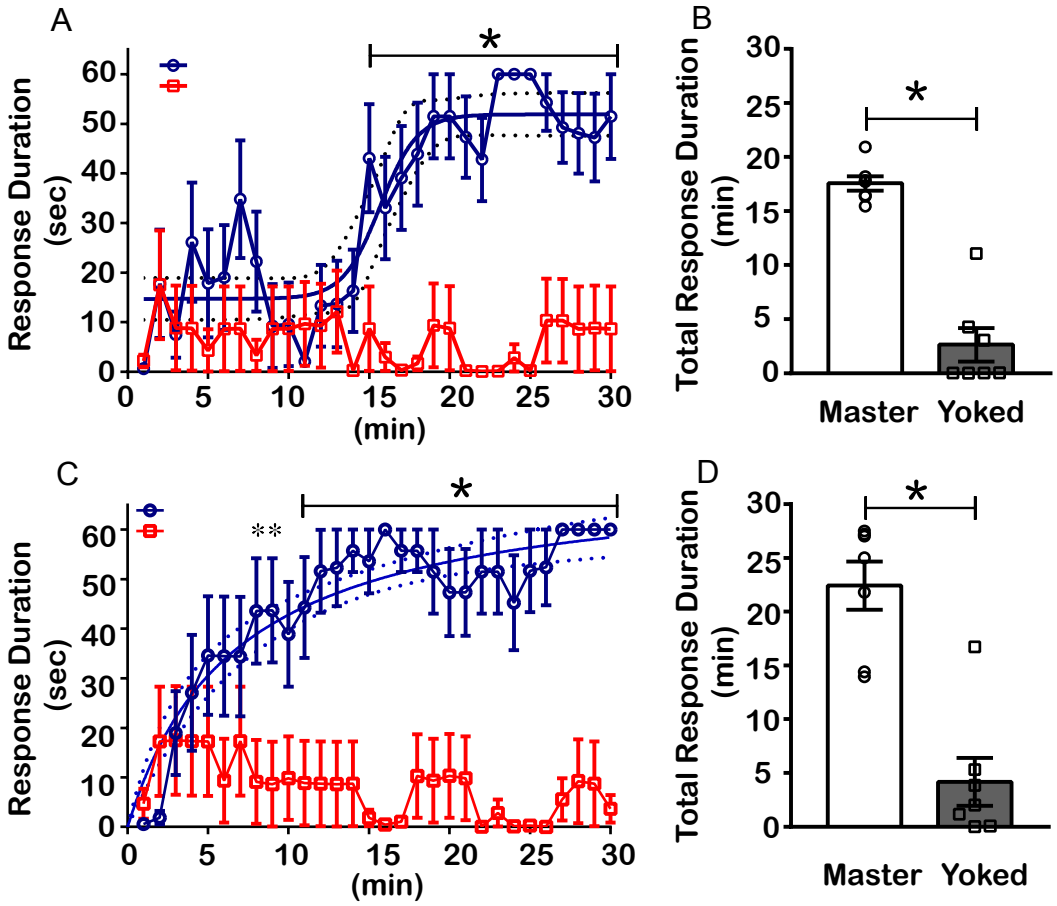

Figure 4- 4

Figure 4-4 PaWL response duration curves in J20 and WT mice.

A) The master group of 4mon J20 mice (J20 4mon, n=8) showed significant increase in response duration compared to the yoked group from 15th-30th minute out of the 30min testing session. B) Total response duration in the 4mon J20 master group was also significantly greater than the yoked. C) The master group of 4mon WT mice (WT 4mon, n=7) showed significant increase in response duration at the 8-9, and 11-30 min in the 30min test. D) The total duration in 4mon WT master group was significantly higher than that in the yoked WT mice. From the curve fit analysis, the master 4mon WT mice reached half-the maximum response duration faster (T_{50}= 4.982min) than master 4mon J20 mice (T_{50}= 15.91min). Confidence bands show the range or likely location of the true curve. *: P<0.05; **: P<0.01.

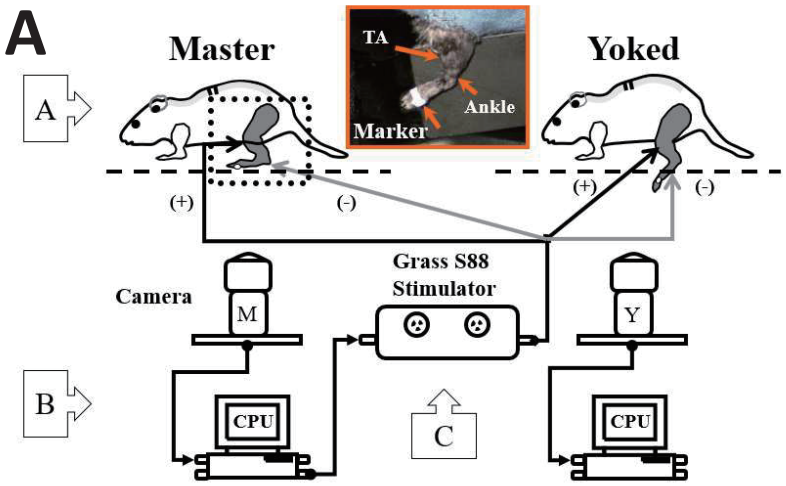
A
Master
Yoked
TA
Ankle
Marker
A
(+)
(-)
(+)
(-)
Camera
Grass S88
Stimulator
M
Y
B
CPU
C
CPU

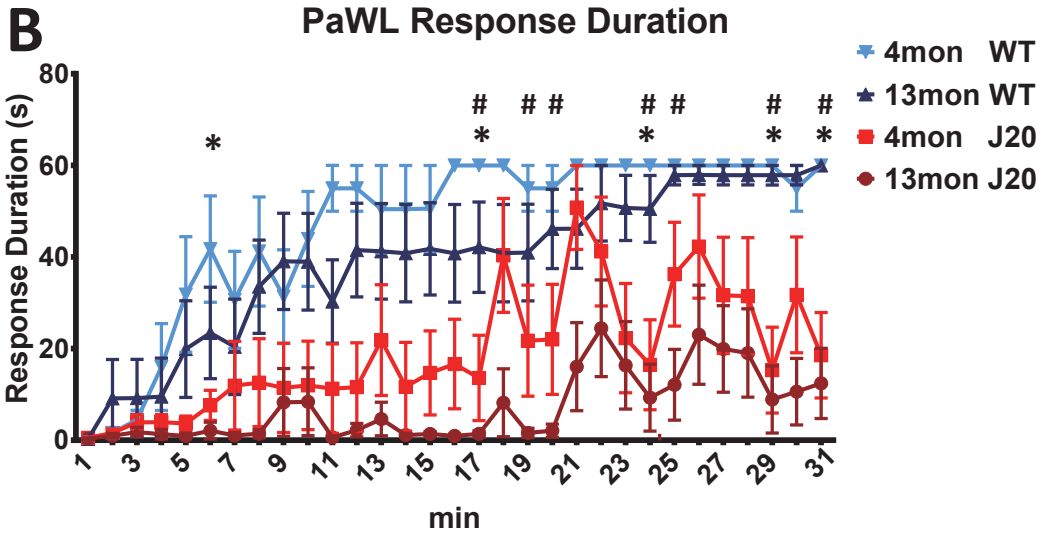
B
PaWL Response Duration
4mon WT
13mon WT
4mon J20
13mon J20
Response Duration (s)
80
60
40
20
0
1
3
5
7
9
11
13
15
17
19
21
23
25
27
29
31
min

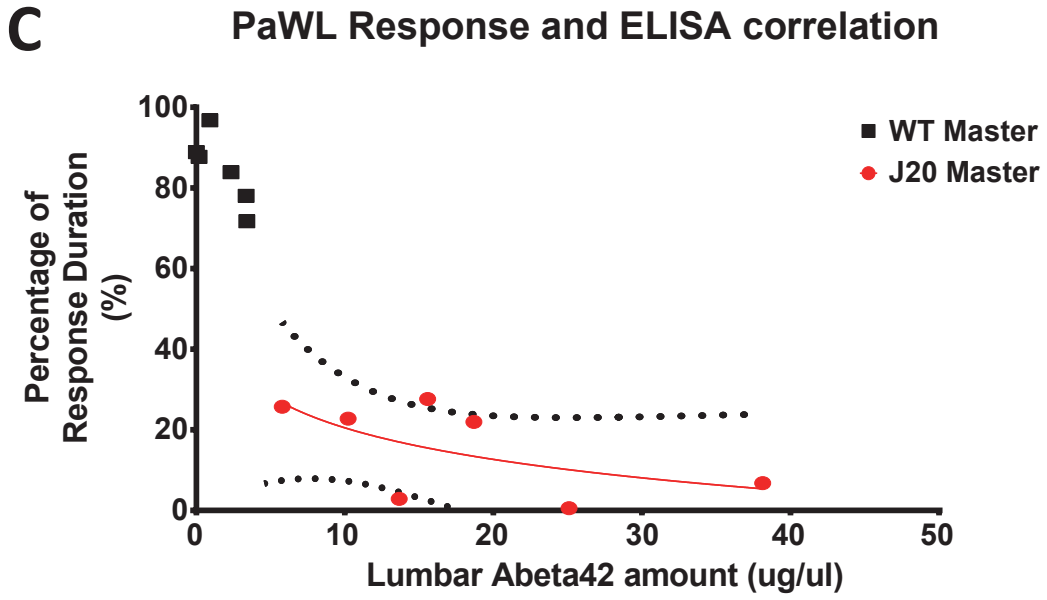
C
PaWL Response and ELISA correlation
WT Master
J20 Master
Percentage of Response Duration (%)
100
80
60
40
20
0
0
10
20
30
40
50
Lumbar Abeta42 amount (ug/ul)

Figure 4- 5

Figure 4-5 The PaWL response duration was correlated with lumbar spinal Aβ42 expression level. (A) The setup of PaWL in Master and Yoked mice. Only Master mice will be conditioned to hold up the dorxiflexion of the tested hind paw. **(B) The PaWL Response Duration changing curves of J20 and WT mice at 4month and 13month age.** Both 4mon and 13mon J20 mice showed significant decreases in PaWL response duration compared to 4mon and 13mon WT groups at the 17-31min during the testing. Moreover, both 4mon and 13mon WT mice reach their half-the maximum response duration earlier than J20 mice from both groups, while in both genotypes, the 4mon mice reach half-the maximum response duration slightly earlier than the 13mon mice. (13mon J20, n=12, T_{50RD}=22.01min; 4mon J20, n=7 T_{50RD}=19.68min; 13mon WT, n=8, T_{50RD}=15.28 min; 4mon WT, n=8 T_{50RD}=6.16min). **(C) The PaWL correlation scatter plot of PaWL Response Duration and lumbar hAβ42 ELISA measurement in J20 and WT mice at a mixed age (J20 n=7, WT n=6).** Consistent with the observations from B, The J20 mice have a smaller response duration average compared to the WT mice. All the WT mice demonstrated a low hAβ42 expression in lumbar spinal level (<3.24 ug/ul), while J20 mice lumbar hAβ42 expression levels were all above 5.16ug/ul. The regression trend line of hAβ42 expression levels and the PaWL response duration showed a negative correlation.

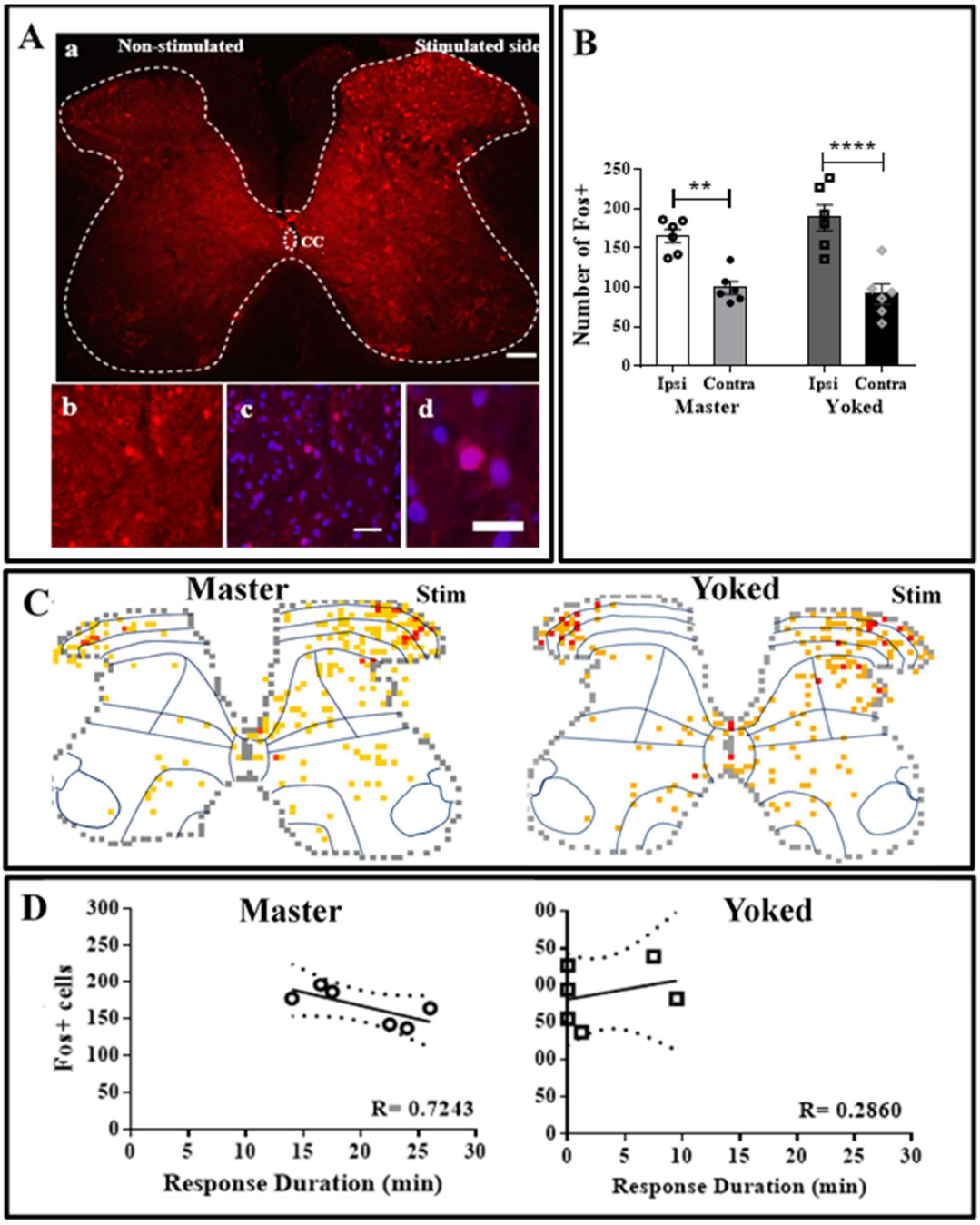

Figure 4- 6

Figure 4-6 Number of activated neurons in the WT master mice is correlated with the degree of learning.

c-Fos antibody was used in IF stianings to identify the cell activation pattern in PaWL. **A)** shows the Fos+ neuclei in a lumbar 4 (L4) spinal cord section of a WT master mouse. **Aa)** Fos+ imunostaining at x5, scale bar = 100µm; **Ab), Ac)** shows the Fos+ only and

Fos+/DAPI+ nuclei at x20, scale bar=20μm; **Ad)** shows the Fos+/DAPI+ nuclei at x40, scale bar=20μm. **B)** shows the total Fos+ in ipsilateral and contralateral spinal cord. **C)** The representative sections for WT master and yoked mice tagged with Fos+ cell distribution. Total Ipsi Fos+ cell number in master **(D)** and yoked **(E)** WT mice were correlated with the response duration (PaWL). Master/yoked pairs, N=6, 10 cornal sections in L4 segment per animal.

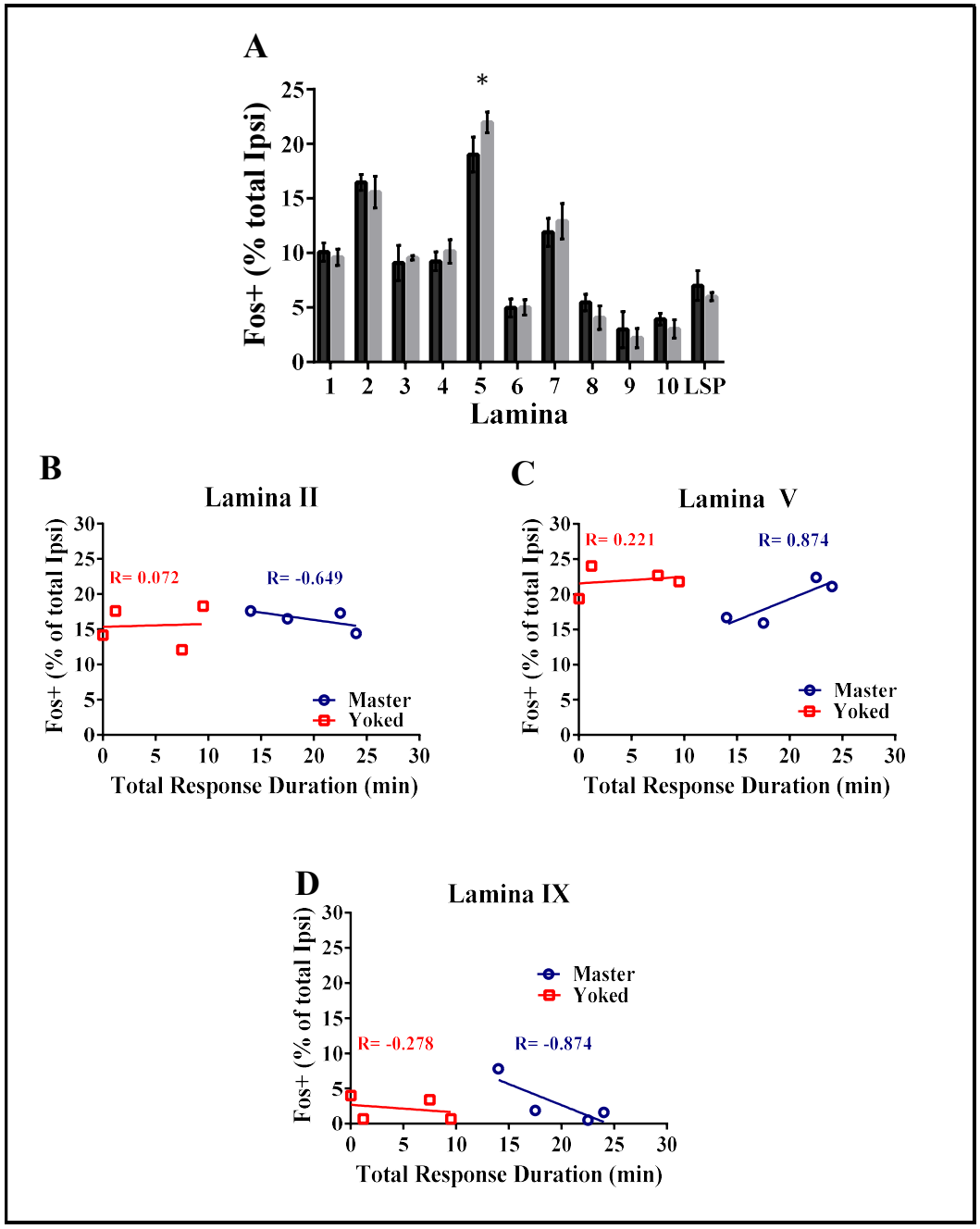

Figure 4- 7

Figure 4-7. Fos+ in lamina V shows a positive correlation with PaWL quality.

A) The distribution of Fos+ in different ipsilateral spinal cord lamina layers of master and yoked mice. Correlation of response duration with Fos+ in lamina II **(B),** lamina IX **(C)** and lamina V **(D)** are shown with the Person correlation coefficient R. LSP, lateral spinal nucleus, master/yoked pairs, n=4, 10 L4 sections per animal).

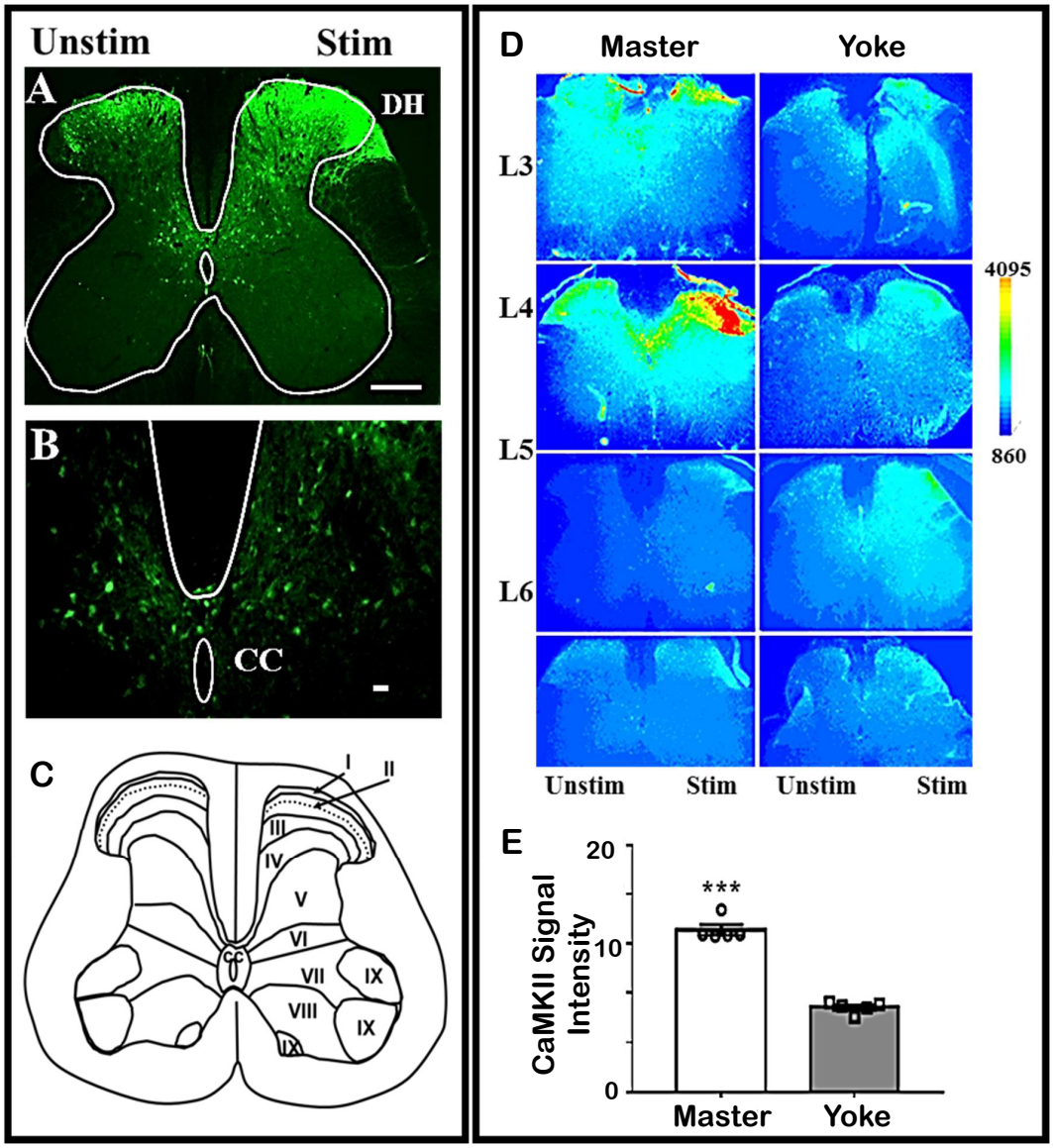

Figure 4- 8

Figure 4-8. CaMKII immunoreactivity is increased in the dorsal horn (DH) in master, but not in yoked mice after PaWL test.

Spinal cord sections from L3-L6 from master and yoked mice were processed for CaMKII immunoreactivity. L4 section of a master mous showing strong CaMKII+ staining (cell body and terminals) in lamina I-III **(A)** and IV-V **(B)** on the ipsilateral side. **C)** The schematic illustration of a L4 section shows lamina borders. **D)** Comparison of CaMKII+ staining in the

L3-L6 segments of master/yoked pairs showed that the CaMKII staining in the ipsilateral DH was stronger than that of the contralateral side. Pseudo color images of staining were generated using the Axio software and matlab for better visualization, where red is the most intense in the color bar. **E)** The immunoreactivity intensities in concurrently processed sections were quantified at a selected threshold above the background. Master animals contained significantly higher levels of CaMKII in L4 dorsal horn than the yoked mice ($p<0.05$, N=5, master/yoked pairs, 5 sections per animal per spinal cord segment). The scale bars in A) and B) = 100μm, C)= 20 μm. CC: lamina X, central canal.

CHAPTER 5: Blocking the lumbospinal Aβ overexpression with acute gamma secretase inhibitor (GSI) delivery partially restored the locomotive function in both intact and spinal J20 mice

INTRODUCTION

Soluble Aβ oligomers might matter more in AD.

In recent years, the leading amyloid leading AD pathogenic hypothesis has been challenged. In the amyloid hypothesis, the cytotoxic effect of extracellular insoluble fibrils in AD brain is the primary influence that triggers the cascade of AD pathogenic changes. However, the relevance of these plaques to AD pathogenesis is still unclear and frequently questioned by many investigators. Multiple clinicopathologic studies have been unable to confirm a relationship between amyloid plaque burden and dementia severity or loss of neurons and synapses. Moreover, numerous amyloid plaques that match the brain regional pattern of distribution seen in demented AD patients may also be present in many non-demented individuals. Last but not the least, clinical trials with drugs aiming at increasing the plaque clearance rate all failed.

The results from this study also show that the function changes in J20 are not correlated with the amyloid plaque loadings. In **Chapter 3**, **Fig. 3-9** showed that the function of the locomotive lumbar spinal circuit was significantly impaired in J20 mice, but no amyloid plaque is detected in J20 spinal cord.

On the other hand, our result from **Chapter 4**, **Fig 4-5C** suggests that soluble oligomeric forms of hAβ might play a larger role than the insoluble components in causing neuronal damage and functional deficits in AD. In this study, lumbar soluble hAβ expression levels are negatively correlated with the quality of PaWL spinal learning performance. The results from man other groups are also in support of this alternate hypothesis. It has been shown that stable Aβ oligomers decrease cell surface expression of NMDA receptors, inhibit induction of long-term potentiation, facilitate long-term depression, alter dendritic spine density and affect hippocampal synaptic plasticity. Together, these studies suggest that oligomeric forms of Aβ are potentially responsible for loss of connectivity and disrupted learning-related synaptic plasticity in AD.

γ secretase inhibitor

To test whether soluble hAβ oligomers are the cause of the locomotion and spinal learning deficits we previously observed in both intact and spinal J20 mice, γ secretase inhibitor (GSI, LY411575) was given to J20 mouse for 4 days right before the behavioral tests. Because it usually takes about 3weeks to a month to break down and significantly decrease amyloid plaques burden, 4-day acute GSI application will not significantly affect the existing amyloid plaque loading but will block new Aβ generation. Because the average soluble Aβ

degradation duration is 2~2.5 day, a 4-day GSI delivery will significantly decrease the soluble Aβ expression levels.

Notably, GSI also inhibits Notch signaling pathway. LY411575 has been reported as a powerful blocker of Notch activity. Because Notch influences synaptic plasticity and learning, it is also possible that the GSI application might impair the learning and plasticity through Notch signaling but not through the amyloid cascade. Therefore, controlling the dosage of GSI is very important. In this study, the GSI delivery will be stopped for at least 3 days to prevent the Notch pathway related side effects induced by GSI.

MATERIALS AND METHODS

Animal Groups

All animal studies were performed according to protocols examined and approved by the Animal Use and Care Committee of University of California, Los Angeles. The J20 transgenic mouse line expresses a mutated human APP (hAPP: K670/M671L and V717F) under the control of the platelet-derived growth factor promoter (Mucke). In our studies, we have used a J20 mouse line crossed to a C57BL/6 background. In order to study the progression of the pathology, we further separate our animals by their age into 4 month (4mon) and 13 month (13mon) group. Because the cognitive deficits of the J20 animal start to be prominent after 5 month old, 4mon J20 mice are equivalent to pre-clinical phase animals. Our model dataset consists of thirty-one animals (15 4-month old, 16 13 month old) labeled as either WT or J20.

Drug delivery through oral gavage.

The animal was first restrained by scruffing by a dorsal neck fold. The gavage needle measured externally from the tip of the nose to the last rib to clarify the length of tube insertion. Then the gavage needle will be lubricated lightly with KY (jelly). The gavage tube will be positioned into the mouth to the right or left of the incisor teeth. With aid of the tube, the animal's head was gently repositioned upward and back to the almost 90^{o} angle in order to straighten the neck and esophagus. The tube was slowly advanced down the oral cavity and into the esophagus watching for the swallowing reflex. The tube should pass freely into the esophagus without being forced. When the desired length of insertion was archived, the solution was administered. The volume could not exceed the 1-2% of body weight for mice about 30-35g, dose had been calculated based on these ranges. The mouse was observed for no less than 15 min after a procedure for sighs of pain or distress, such as gasping, bleeding or frothing at the mouth.

18-20G X1.5" bulb-tipped needles were used.

γ-secretase inhibitor (GSI) treatment

For all the animal groups studied in this chapter, GSI LY411575 (Millipore-Sigma, Billerica, MA) was delivered once a day at a dosage of 50mg/kg body weight for 4 days to block enzyme activity. This dosage and drug delivery duration has previously been shown to reduce Aβ levels in vivo. Each animal will receive the initial dose 15 min after CCI or SCI or sham surgery and then twice daily for 3 days: at 2, 24 and 72 hrs after surgery. We implement this dosing regime because Aβ levels are known to drop after γ-secretase inhibition before recovering over several hours.

Quadrapedal treadmill stepping

Animals of all groups are tested according to protocols established in Edgerton lab (Courtine et al., 2008). In brief, treadmill stepping was measured utilizing video motion capture analysis tools. Retroreflective markers were placed on the wrist, shoulder, back, lliac crest, hip, knee, ankle, and foot bilaterally. Video was collected through the SIMI system while the mice stepped quadrapedally on a treadmill. In order to obtain stable and representative gait pattern, the speed of the treadmill was increased by 3 cm/s once the animal was able to complete at least 10 consecutive steps. Speeds ranging from 3 to 30 cm/s (or until the mouse could not keep up with the treadmill) were tested. The 3D-coordinates (x, y, z) of all the tracked body parts were extracted by SIMI 2/3D analysis software for further feature extraction.

Complete mid-thoracic spinal cord transection Surgery

The spinal cord was completely transected at the T7–T9 vertebral level in all mice as described previously. Briefly, under 2% isoflurane anesthesia, a dorsal midline skin incision was made from T6 to T9 and the musculature covering the dorsal vertebral column was retracted to expose the spinal lamina. A partial laminectomy of the T7 and T8 vertebrae was performed to expose the spinal cord. The spinal cord, including the dura, was transected completely using microscissors. The completeness of the lesion was verified by separating the cut ends of the spinal cord with small cotton pellets and by passing a fine glass probe through the lesion site. The skin incision was closed using small surgical staples.

After surgery, the wound sites were treated with triple antibiotic ointment (Bacitracin) and the mice were given lactated Ringer's solution (1.5 ml/30 g body weight, s.c.). Because preventing leg extension during recovery has been shown to facilitate subsequent learning in

rats, both hindlegs were bound with the knee and ankle joints fully flexed until PaWL testing. The mice recovered in an incubator maintained at 37°C until fully awake and then were returned to their home cages. The mice were allowed to recover for 24 hr before PaWL testing. To minimize bias, the surgeons and testers were blind to the diet and exercise conditions during surgery and PaWL testing.

Bipedal treadmill stepping

All mice were tested hind limb stepping on a treadmill once a week for 7 weeks post spinal cord transection. Mice were placed in a harness, which was secured to the body weight support system (Velcro). All animals were tested from 3cm s^{-1} to 15cm s^{-1} forward and reversely with a 3cm s^{-1} step while the body weight support system supported 85% of the mouse's body weight. During testing, the animal was tested 20s for each speed before move to the next one. After being tested at all speeds, all the mice were given serotonin agonist, Quipazine (0.3mg/kg body weight, Sigma) i.p. and tested again on treadmill at all speeds forward and reverse 20min after injection. Between tests, all mice were placed in the harness 20-25min/day for acclimation. All the locomotion tests were recorded and analyzed by SIMI motion capture system.

Paw Withdrawal Learning Paradigm (PaWL) Procedure

PaWL experimental setup

The PaWL test was conducted 24 h after the spinal cord transection surgery on mice. The details of the PaWL testing for mice have been described previously. Briefly, during testing the mice were restrained in a closed cloth harness with two slots cut at the end of the harness to allow for both hind limbs to hang freely (**Figure 4-1**). Two fine-wire hook electrodes were constructed by removing 1 mm of insulation at the end of nylon-coated single strand stainless

steel wires (California Fine Wire Co., Grover City, CA). Each wire was passed through a 32-gauge needle: one electrode was inserted intramuscularly into the left TA muscle and the second electrode was inserted subcutaneously at the base of the lateral malleolus on the same side to serve as a ground. The electrodes were attached to a stimulator (S88, Grass Product Group; W. Warwick, RI), through a stimulus isolation unit (SIU5; Grass Product Group) and a constant current isolation unit (CCU1; Grass Product Group). A stimulus duration of 50 msec followed by a 10 msec delay between consecutive pulses was used throughout the PaWL test session as previously described.

ELISA and western blot analysis.

Fresh-frozen spinal cords were homogenized in 110 mgml-1 in 2% w/v sodium dodecyl sulphate (SDS) in water with protease inhibitors (Roche) to recover soluble amyloid. The sample was then centrifuged and the pellet homogenized in 70% formic acid in water to obtain the insoluble amyloid fraction. Homogenates were spun at 100,000g for 1h. Supernates were diluted in buffer EC (0.02M sodium phosphate, pH 7.0, 0.2 mM EDTA, 0.4M NaCl, 0.2% bovine serum albumin, 0.05% CHAPS) on ice. To obtain the soluble amyloid fraction and protein for western blotting, frozen spinal cord were homogenized in cell lysis buffer (Cell Signaling), sonicated briefly and centrifuged at 14,000 r.p.m. for 10 min. Aβ42 was measured by ELIS (Covance) following the manufacturers protocol. Immunoblotting was performed using the following polyclonal antibodies C-terminal APP (Calbiochem), PSD95 (Cell Signaling)

RESULTS

The drag steps, slower speed and the imbalance between left and right hind limb in J20 quadruapedal stepping were fully rescued after 4-Day GSI application.

As shown in Chapter 2, the kinematics analysis and comparison between the J20 and WT quadrupedal treadmill stepping shows that there are three prominent differences between the locomotion pattern of J20 and WT. The three significant features that differentiate J20 from the WT quadrupedal stepping are: 1) slower stepping speed; 2) imbalance/ losing coordination between left and right limbs; 3) more drag steps (**Fig. 2-1**). While these three features were still observed in the J20 +Vehicle group mice, 4-Day consecutive GSI daily delivery significantly improved the quadrupedal stepping quality in J20 mice.

The bilateral hind limbs 3D coordinates of mice tested by quadrupedal treadmill stepping were recorded and tracked by SIMI software, and then be normalized, averaged and visualized by Matlab. **Fig. 5-1A** shows that the imbalance between left and right hind limbs observed earlier in Chapter 2 is no longer significant after GSI treatment but not the vehicle treatment. **Fig. 5-1B** compares the quadrupedal coordination pattern in the 4mon J20 taken vehicle only or taken GSI for 4 days before the test. Within the same time (3.5 min), 4mon J20 mice with GSI were all able to finish 10 consecutive steps with 1 drag step (The percentage of good steps: 100*1/40%=797.5%). However, in the J20 +vehicle group, only 8-9 alternative stepping sets were completed. There were 8 drag steps among the 35 total steps. Within the same time, the J20 + vehicle group generated fewer treadmill steps and demonstrated a lower percentage of good steps (100*27/35%=77.143%). (4mon J20 + GSI, n=25; 4mon J20+ Vehicle, n=18).

4-day GSI delivery improved bipedal stepping kinematics pattern and increased bipedal step number in spinal J20 mice.

Because the quadrupedal stepping improvement in the GSI treated group could also due to the hAβ decrease in supraspinal structures, e.g. GSI might cause hAβ decrease in the motor cortex and then contributed to the functional improvement in the quadrupedal stepping, the GSI application was also tested in spinal J20 and WT mice. The GSI influence on the spontaneous locomotion recovery after the complete spinal cord transection was again evaluated by the bipedal treadmill stepping test.

4-Day GSI delivery is sufficient to fully rescue the spontaneous bipedal stepping recovery in the 13mon J20 mice (**Fig. 5-2B$_3$, B$_4$**). However, GSI could not fully restore the spontaneous locomotion recovery curve in 4mon J20 (**Fig.5-2B$_1$, B$_2$**), especially in Post-transection Week 5 and Week 6. This result suggests that other mechanisms than soluble Aβ amount may also contribute to the spontaneous locomotion recovery delay observed in 13mon J20 mice. **Fig. 5-2C** shows the schematics of the tracked hind limb joints position, **Fig.5-2D** is the Western Blot results showing that the lumbar spinal Aβ expression was significantly decreased after 4-day GSI delivery. **Fig. 5-2E$_{1-4}$** showed the tracked hind limb joint coordination in the 1st week testing. The joint coordination and the recovery of bipedal stepping were facilitated by GSI. J20 +GSI **(E$_3$)** stepped even better than WT mice in the 1st week test **(E$_4$).** In the 7th week, the bipedal stepping pattern of the J20 mice was not significantly different from that of the WT **F$_{1-4}$)**.

GSI showed different effects on 4mon and 13mon PaWL performance. Applying GSI to J20 and WT mice also induced different effect.

Fig. 5-3B shows the correlation between the PaWL response duration percentage (learning quality) with the lumbar spinal $hA\beta_{42}$ or $hA\beta_{40}$. Decreasing the lumbar spinal $hA\beta_{42}$ and $hA\beta_{40}$ in the J20 group significantly increased the spinal learning qualities in PaWL paradigm. However, interestingly, WT with GSI showed that when the lumbar spinal $hA\beta_{40}$ was down regulated, PaWL learning quality would decrease. **Fig. 5-3C** shows that the 4-Day GSI delivery fully rescued the PaWL learning performance in 13mon J20 mice but only partially recover the learning capability in the 4mon J20 group.

DISCUSSION

Why GSI application would decrease the PaWL learning quality in the WT mice?

There could be two possibilities in the GSI induced spinal learning quality decrease. One is that the learning process is disturbed because of GSI inhibited the Notch signaling pathway. Another possibility is that dose-dependent biphasic activation happens in GSI as well as Aβs. The previous researches showed that γ-Secretase can bind at the same time its substrate, its transition state inhibitor, and its different non-transition-state inhibitors. This indicates that γ-secretase can bind its substrate and its inhibitors to different sites at different concentrations, and different sites have different functional properties. Subsequent more quantitative analysis of different γ-secretase inhibitors showed that changes in the substrate level could change dose-response curves and the inhibition potency by more than one order of magnitude. At lower substrate levels different inhibitors show unusual biphasic activation-inhibition dose-response curves for Aβ 1–40 and Aβ 1–42, which can change to standard dose-response curves at the higher substrate levels. Interestingly, the biphasic dose-response can be

observed only in the pathogenic β-secretase → γ-secretase branch of APP metabolism, while the α-secretase → γ-secretase branch shows a standard dose-response.

Thus, further studies about the dose-dependent processing of APP and the quantitative analysis of APP metabolism should be done in the future in order to understand the underlying mechanism of how the drugs as γ-secretase inhibitors induce side effects in vivo.

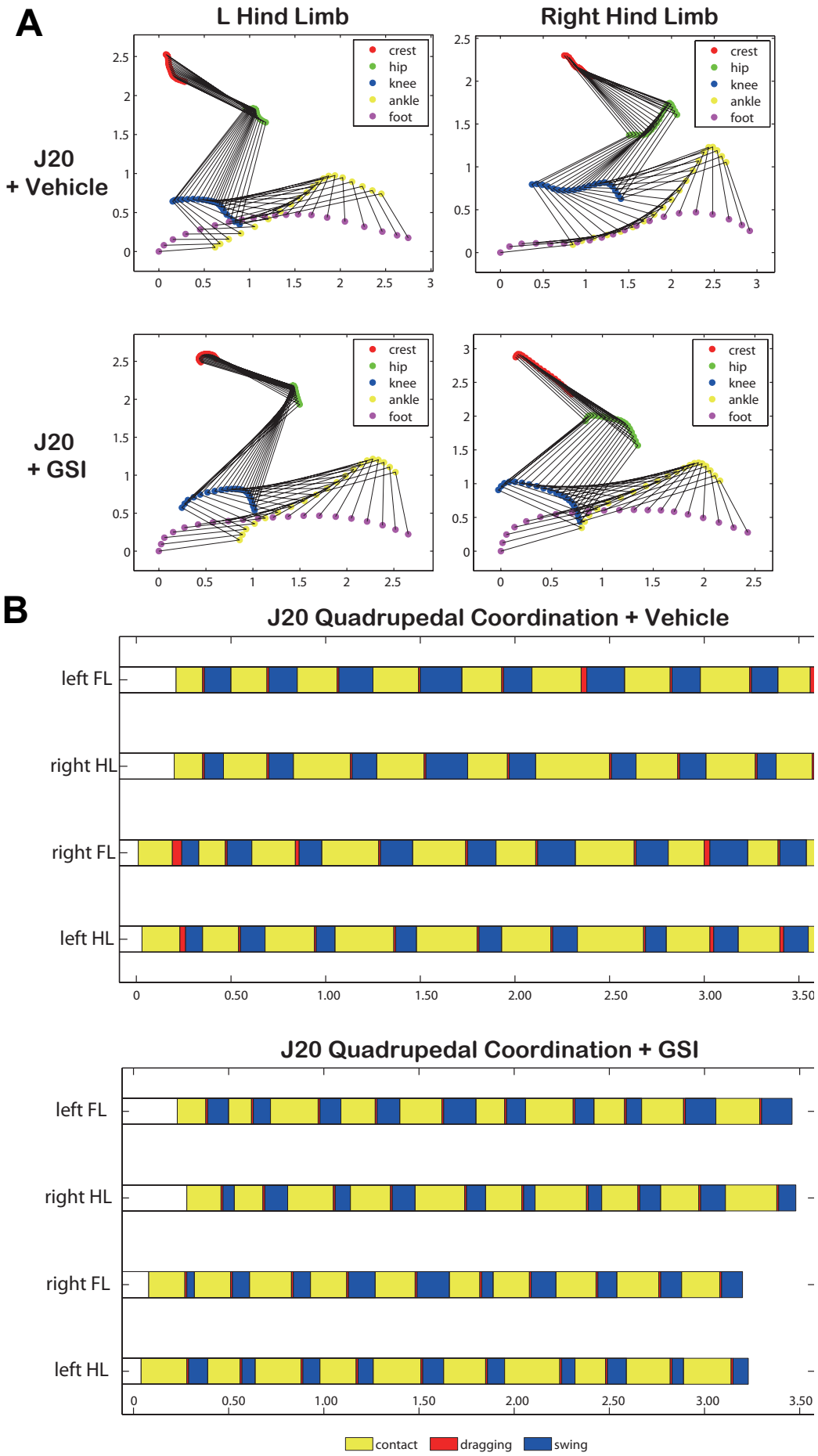
A
L Hind Limb
Right Hind Limb
J20
+ Vehicle
J20
+ GSI
crest
hip
knee
ankle
foot
B
J20 Quadrupedal Coordination + Vehicle
left FL
right HL
right FL
left HL
0
0.50
1.00
1.50
2.00
2.50
3.00
3.50
J20 Quadrupedal Coordination + GSI
contact
dragging
swing

Figure 5- 1

Figure 5-1. The J20 mice featured quadrupedal stepping kinematics impairments were fully rescued by 4-Day GSI application.

The bilateral hind limbs 3D coordinates of mice tested by quadrupedal treadmill stepping were recorded and tracked by SIMI software, and then be normalized, averaged and visualized by Matlab. The stepping kinematics patterns of 4mon J20 and WT mice were tested with vehicle (Saline with cranberry juice) or GSI For 4mon J20 mice, **A)** shows that the imbalance between left and right hind limbs observed earlier in Chapter 2 is no longer significant after GSI treatment but not the vehicle treatment. **B)** compares the quadrupedal coordination pattern in the 4mon J20 taken vehicle only or taken GSI for 4 days before the test. Within the same time (3.5 min), 4mon J20 mice with GSI were all able to finish 10 consecutive steps with 1 drag step (The percentage of good steps: 100*1/40%=797.5%). However, in the J20 +vehicle group, only 8-9 alternative stepping sets were completed. There were 8 drag steps among the 35 total steps. Within the same time, the J20 + vehicle group generated fewer treadmill steps and demonstrated a lower percentage of good steps (100*27/35%=77.143%). (4mon J20 + GSI, n=25; 4mon J20+ Vehicle, n=18).

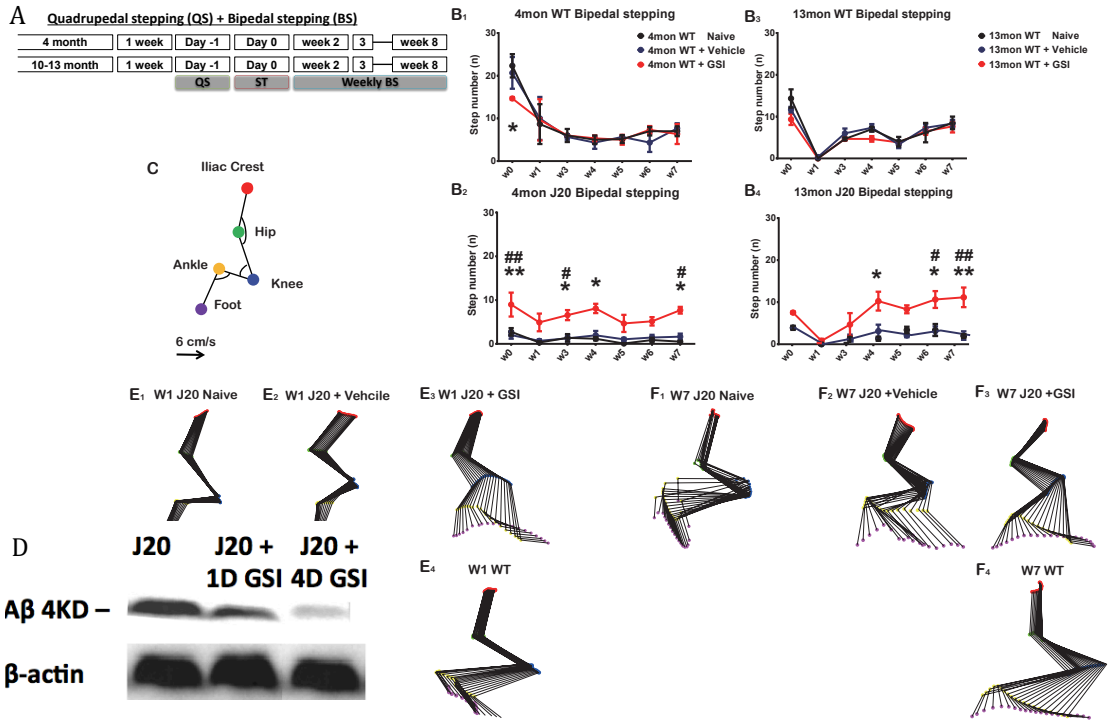

Figure 5- 2

Figure 5-2 4-day GSI delivery improved bipedal stepping kinematics pattern and increased bipedal step number in spinal J20 mice.

A) The illustration of the timeline of quadrupedal – bipedal treadmill stepping group. After the quadrupedal treadmill stepping baseline was taken, all the animals were acclimated onto the bipedal treadmill for a week before the complete spinal cord transection. After the complete transection, all the animals took one week for recovery and then started bipedal stepping test once a week to measure the spontenous recovery of hind limb kinematics pattern. GSI/vehicle delivery started 4 days before the test and was delivered for 4 consecutive days. After the test, the GSI delivery would pause for 3 days and resume again to prepare the mouse for next around of test of the following week. **B)** 4-Day GSI delivery is sufficient to fully rescue the spontaneous bipedal stepping recovery in the 13mon J20 mice (**B_3, B_4**). However, GSI could not fully restore the spontaneous locomotion recovery curve in

4mon J20 (**B_1**, **B_2**), especially in Post-transection Week 5 and Week 6. This result suggests that other mechanisms than soluble Aβ amount may also contribute to the spontaneous locomotion recovery delay observed in 13mon J20 mice. **C)** shows the schematics of the tracked hind limb joints position, **D)** is the Western Blot results showing that the lumbar spinal Aβ expression was significantly decreased after 4-day GSI delivery. **E_{1-4})** show the tracked hind limb joint coordination in the 1st week testing. The joint coordination and the recovery of bipedal stepping were facilitated by GSI. J20 +GSI (E_3) stepped even better than WT mice in the 1st week test **(E_4).** In the 7th week, the bipedal stepping pattern of the J20 mice was not significantly different from that of the WT **F_{1-4})**. */#: P<0.05; **/##: P<0.01

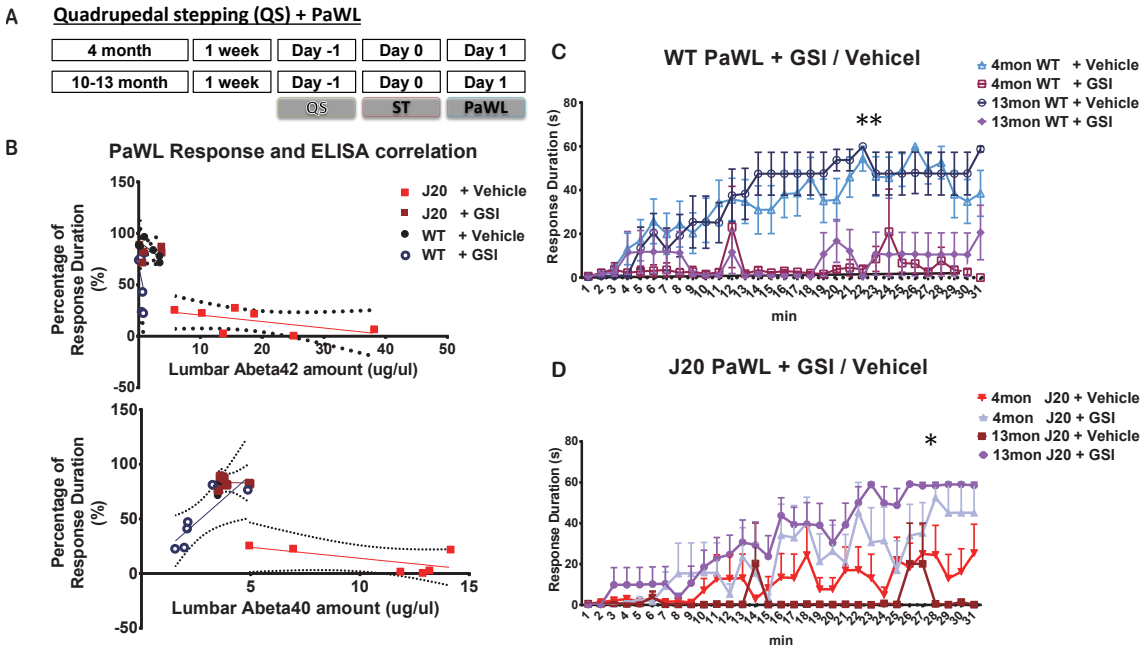

Figure 5- 3

Figure 5-3. The 4-day GSI delivery completely rescued the instrumental learning deficits in PaWL through reducing spinal Aβ42

A) The illustration of the timeline of quadrupedal – PaWL group. After the quadrupedal treadmill stepping baseline was taken, all the animals were acclimated onto the PaWL harness for a week before the complete spinal cord transection. The PaWL was performed within 24hrs after the transection. GSI/vehicle delivery started 2 days before the complete spinal cord transection surgery. The GSI was also delivered right before the complete transection surgery as well as 3hr before the PaWL test to ensure that GSI was delivered in 4 consecutive days. B) The correlation between the PaWL response duration percentage (learning quality) with the lumbar spinal $hA\beta_{42}$ or $hA\beta_{40}$. Decreasing the lumbar spinal $hA\beta_{42}$ and $hA\beta_{40}$ in the J20 group significantly increased the spinal learning qualities in PaWL paradigm. However, WT with GSI demonstrated decreased PaWL learning quality when the lumbar spinal $hA\beta_{40}$ decreases. C) 4-Day GSI delivery fully rescued the PaWL learning performance in 13mon J20 mice but only partially recover the learning capability in the 4mon

J20 group. *: P<0.05, **: P<0.01.

Chapter 6: Alternative options other than the pharmacological means in regulating the AD spinal cord

Introduction

The mammalian respiratory system is controlled by a complex network of neurons interconnected among several nuclei located in the brainstem. The origin of the respiratory rhythm has been attributed to the pre-Bötzinger Complex (preBötC) located in the ventral medulla (14, 29) 27) and the parafacial respiratory group (pFRG) located in the rostro-ventrolateral medulla (11, 28). Pontine nuclei also seem to be important for generating the eupneic rhythm (21, 32). The rhythm generating elements within the pons and medulla are intimately interconnected and embedded within neuron groups that shape the pattern of the respiratory output. Thus, within this larger respiratory central pattern generator, there are individual rhythm generating elements that come into play in a variety of different circumstances. Among the key structures for respiratory control are the ventral respiratory column (VRC), pontine respiratory group (PRG) and dorsal respiratory group (DRG) (21). This network of neurons in turn activates the motor neurons of respiratory muscles in a highly choreographed sequence, which leads to remarkably stable and well-coordinated inspiratory and expiratory flow during activities as diverse as quiet eupnea, speech and vigorous exercise (4). The respiratory central pattern generator (CPG) may overlap and

coordinate with other CPGs so that the respiratory pattern may be involved in or encompassed within a variety of other activities, such as swallowing, coughing and sighing.

Speculation about the existence of spinal respiratory neurons with rhythmic properties in the spinal cord was raised when inspiratory unit activities were recorded in C1-C2 segments of transected cats (1), and it is now well documented that there are inspiratory neurons found in the upper cervical cord (12, 16, 17, 22). A study using an *in vitro* preparation of the neonatal mouse brainstem-spinal cord has shown that spontaneous rhythmic respiratory burst activity can be generated in the cervical ventral roots of C1/C2 and C4 following transection of the spinal cord above C1 (19).

To date, studies that have identified cervical spinal cord involvement in respiratory function have used *in vitro* testing (1, 10, 12, 19). To gain a better understanding of the role of the upper cervical spinal cord in respiration, we examined the effect of electrical stimulation of the cervical spine on respiratory activity in intact anesthetized mice. We applied direct, constant current stimulation to the epidural surface of the exposed spinal cord from the most caudal region of the medulla (C0) through C1 to C5 and recorded the respiratory output. The aim of our study was (1) to identify a stimulation intensity required to evoke a respiratory response and (2) to determine if there were an optimal cervical regions to stimulate in order to increase respiratory activity in healthy adult mice. Our results showed that epidural stimulation at the C3 level of the spinal cord with 1.5 mA increased the respiratory rate and the sigh frequency, but did not change the tidal volume in anesthetized mice. Our findings show that respiratory function, possibly involving two respiratory related CPGs – eupnea and sighing - can be altered by stimulation of the cervical spinal cord if the appropriate stimulation intensity and location are used.

Methods

Animal

Mixed gender 5-month-old C57BL/6 mice were used in this study. All mice were kept and tested according to protocols approved by Animal Research Committee (ARC) at University of California, Los Angeles. All procedures were conducted on mice anesthetized by isoflurane. All mice were subjected to sham and monopolar electric epidural stimulations of the spinal cord.

Laminectomy

To perform the laminectomy, the animal was placed under anesthesia and spread prone on a surgical pad. The laminae from the C1 to C6 vertebral levels were gently removed to expose the spinal cord with intact dura matter. Gauze pads soaked in mineral oil were placed on top of the spinal cord to keep it moist, and the dorsal skin on either side of the wound was carefully clipped together with surgical clips to keep the gauze in place. The animal was then positioned for a tracheostomy and intubation.

Tracheostomy and intubation

Respiratory flows were measured in anesthetized and tracheostomized mice. The tracheostomy and intubation methods were adapted from the protocol described by Moldestad et al. (25). Briefly, a 50~60 mm intravenous catheter (Venflon Pro. BD, 18-20 GA, BD, NJ, USA) was inserted gently between two tracheal rings, and its position was secured by super glue. The animal was observed for 5 min to detect any possible respiratory problems before the super glue completely solidified. Finally, the animal was connected to a pneumotachograph and moved into position for epidural stimulation (see **Fig 6-1A**).

Epidural electrical stimulation protocol

Figure 1B shows the dorsal spinal surface after the laminectomy, and Fig 1C illustrates the epidural stimulation protocol at each cervical level. This protocol was used in all the studies reported here. Pre-sham-baseline respiratory activity was recorded for 2 min, followed by sham epidural stimulation. To conduct the sham stimulation, two polyimide-insulated stainless steel microelectrodes (1 mm tip exposure, AM system, Carlsborg, WA), one stimulation electrode and one reference electrode with a fixed distance of 1mm between each electrode, were gently pressed onto the epidural surface of the spinal cord for 30 s with no current applied. The post-sham-baseline was recorded immediately after for 3 min. The pre-stimulation baseline was then recorded for a further 3 min followed by a 30s electrical stimulation using the same pair of electrodes. Finally, a 5 min post-stimulation baseline was recorded. The same sequence of sham and active epidural stimulation was repeated on the next cervical level in a randomized sequence (C0-C5).

Testing for electrical stimulation intensity and location in cervical spinal cord to evoke a respiratory response.

We first carried out a study to determine if there were suitable intensities and cervical spinal cord levels to evoke a respiratory response in the anesthetized mouse. In this study, 13 mice were used. We tested the brainstem (C0) and C1 to C5 cervical levels with stimulus strengths of 0.3 mA, 0.9-1.0 mA and 1.5 mA using a constant current stimulator. For this study, all the stimulations were performed along the dorsal medial-lateral surface of the spinal cord, and all spinal cord levels were tested bilaterally in a randomized manner. A constant stimulation frequency of 20 Hz and monophasic electrical stimulation, 1% duty cycle and square wave

pulse pattern were used in this study. The ground was placed on the spinal cord 1 mm away from the stimulation electrode for these monopolar stimulations.

Cervical C3 stimulation to examine changes in respiratory response

After the optimal stimulation intensity and cervical level were determined (see results section), a separate study was conducted to examine whether stimulation at each cervical level was sufficient to evoke a respiratory response. A total of 24 mice were used in this study. A laminectomy from C1 to C6 was performed as described above, and all animals were tested using the epidural stimulation protocol as described previously.

Physiological recordings

For all the studies, diaphragmatic electromyographic (EMG) recordings were carried out. A 3-cm incision was made at the base of the rib cage to expose the abdominal surface of the diaphragm. Monopolar electrodes were inserted medially into the diaphragm, and EMG muscle activity was recorded. The EMG recording wires were connected to an amplifier, and the EMG signal was band-pass filtered between 30 and 3,000 Hz and digitized at 10 KHz. An amplifier (3000 AC/DC Differential Amplifier, AM system, Carlsborg, WA), an A/D board (DT1890, Data Translation Inc., Marlboro, MA) and a data analysis software system (DataView, St. Andrew University) were used to record the EMG signals for subsequent analysis. Heart rate (beats per minute), oxygen saturation are monitored and recorded by the PhysioSuite™ system MouseSTAT ® Pulse Oximeter & Heart Rate monitor module (Kent Scientific).

Data collection

The respiratory patterns as well as vital physiological variables (heart rate, peripheral oxygen saturation, respiration rate, and body temperature) of tested animals were monitored throughout the whole test using the PhysioSuite™ system (Kent Scientific). The respiratory flow was monitored through a pneumotachograph and pressure transducer (Biopac Systems, Inc., Goleta, CA) and recorded on a computer using DataView (University of St Andrews). The digitization rates of all the channels were 10 KHz.

Data analysis

For each round of sham and stimulation recording, the data used for analysis were as follows: 1 min pre-sham, 30 sec sham, 3 min post-sham, 1 min pre-stimulation, 30 sec stimulation and 3 min post-stimulation. The respiratory frequency and peak-to-peak amplitude (tidal volume) were extracted. The extracted data were de-noised with a running average filter (time constants = 250 ms), normalized (rectified and smoothed with a Gaussian filter) and visualized through MATLAB (MathWorks, Natick, MA). The analyzed data were presented as a ratio comparing sham to pre-sham, post-sham to pre-sham, stimulation to pre-stimulation, and post-stimulation to pre-stimulation. These data were also used to analyze the occurrence of sighs. Sighs have a characteristic flow morphology and are followed by a brief expiratory pause. Sighs were typically about twice the volume of a normal breath (3). Sigh data were presented as the absolute number of sighs and absolute frequency. Patterns of sigh and eupnea frequency response for each mouse tested were compared to each other to examine if there was a correlation between the sigh response and the eupneic response to epidural stimulation.

The response to epidural stimulation at any spinal level differed among animals. In order to objectively categorize the different patterns of responses, we employed cluster analysis, which can be used to systematically and hierarchically categorize data based on the mathematical similarity of the responses. We performed the hierarchical cluster (Hclust) analysis using R software (https://www.r-project.org) where each trace of the ratio of respiratory activity during stimulation was compared to baseline respiratory activity over time. Hclust uses a distance matrix based on dissimilarity (calculated as the square root of sum of squares of differences in particular attributes) and estimates the Euclidean distance between different data sets (respiratory frequency responses to epidural stimulation in our case). The greater the distance between two patterns of response, the greater the difference in the shape of each trace of respiratory frequency ratios.

For this analysis, we analyzed each point on the ratio of respiratory frequency at 0.25 secs intervals to estimate the differences among frequency responses among animals. If the calculated distance was smaller than 7.5 hierarchical units, the recording was considered to be in the same cluster. If the distance was larger than 7.5 hierarchical units, the recording was placed in a separate cluster. The distance cut-off of 7.5 was validated post-hoc by checking the standard error of the mean within clusters as well as through checking the correlation within and between the clusters. The Kendall Rank Coefficient test and Kendall's Tau-b were used for correlation validation. Both tests are used to test whether the variables within each cluster are truly different. Different cut-off values (2.5, 5, 7.5, 10 and 12.5) were tested with these two tests, and 7.5 was the minimum distance for the variables to achieve correlation validation.

Statistics

A one-way, repeated measures ANOVA was used for all data analyses. If the ANOVA indicated that significant differences existed among treatments, pre-planned paired comparisons were made using p-values adjusted by the Bonferroni method. In all cases, $p < 0.05$ was considered statistically significant.

Results

Optimization of current intensities

Systematic stimulation of the brainstem (C0) and C1 to C5 cervical levels using different current intensity was carried out to identify the optimal stimulation intensity and cervical level required to elicit a respiratory response. Stimulation at 1.5 mA induced cardiac arrest, and therefore, this stimulation intensity was not continued at these cervical levels. An example of a single animal treated with epidural stimulation at 1.5 mA intensity at the C1 level is shown in **Fig 6-2**. The stimulation caused a prolonged apnea, followed by a brief period of irregular respiratory effort before profound bradycardia developed. Brief periods followed in which the heart rate rose, but was not sustained. At no time did we observe any gasps, and the cause of death looked like cardiovascular collapse after an apneic response to epidural stimulation. Electrical stimulation at C0 and C1 at 0.3 and 1.0 mA and at C2 and C4 at 0.3, 0.9-1.0 and 1.5 mA did not significantly increase respiration frequency (**Fig 6-3**). At the C3 level, 0.3 and 1.0 mA stimulation did not affect the respiratory frequency. However, 1.5 mA stimulation at C3 significantly increased the respiratory frequency during the period of stimulation ($p = 0.0387$). The increase in respiratory frequency also continued during the post-stimulation stages of recording even though stimulation had ceased (**Fig 6-3,** see *; $p = 0.0017$). Only 1.5 mA current intensity was tested at C5 as the location was close to a major

blood vessel that impeded epidural stimulation. No respiratory change was observed at C5 using the 1.5 mA stimulation strength (**Fig 6-3**).

Stimulation of C3 with 1.5 mA increases respiratory frequency but not the tidal volume

We determined that 1.5 mA at C3 was the optimal stimulation and location to elicit a change in respiratory frequency. Subsequently, we examined in-depth the frequency response elicited when C3 was stimulated with an electrical current of 1.5 mA. Our results show that there was a significant increase ($p < 0.0001$) in the ratio of stimulated respiratory frequency compared to the sham stimulation (**Fig 6-4A**). The increase in respiratory frequency was seen during stimulation (see black arrow) and persisted in the post-stimulation phase (see red arrow). We only recorded for 3 min post-stimulation, and the duration of the facilitation of respiratory frequency may have persisted longer in some mice. We observed no significant change in the tidal volume of respiration when C3 was stimulated compared to the sham stimulation (**Fig 6-4B**). Our results indicate that cervical epidural stimulation can increase the number of breaths taken, but not the depth of each breath.We calculated minute ventilation breath-by-breath and these results are shown in **Fig 6-4C**. Minute ventilation rose significantly during and after epidural stimulation and tracked the respiratory frequency changes almost exactly. Sham stimulation had no effect on minute ventilation.

There was no significant difference in the heart rate between Sham and Stimulation studies, and the heart rate was stable across all three stimulation conditions (baseline, during and after stimulation) (**Fig 6-4C**). Oxygen saturation was also stable throughout each study and not different between the sham studies and the actual period of epidural stimulation, slight increase in oxygen saturation after stimulation was detected. (**Fig 6-4D**)

Hierarchical cluster analysis.

Using Hclust analysis we showed that the responses among animals could be grouped into different hierarchical clusters of respiratory responses when sham or epidural stimulation with 1.5 mA at C3 was carried out (**Fig 6-5A, B**). Twenty-three out of 24 of the sham stimulation responses belonged to the same cluster (**Fig 6-5Ci**). Only one of the 24 sham stimulation sequences fell into a different hierarchical cluster (**Fig 6-5Cii**), indicating that during sham stimulation, respiration was unchanging and similar across virtually all sham stimulation sequences in all of the animals. When epidural stimulation was used, six hierarchical clusters were identified (**Fig 6-5D**). The clusters differed in terms of the timing of the increase in respiratory frequency, and the persistence of the increase in respiratory frequency once epidural stimulation ceased. Clusters 1, 3, 4 and 6 contained 16 of the 24 animals studied (**Fig 6-5Di, iii, iv and v**), and these clusters shared two features: the respiratory rate rose during epidural stimulation and the respiratory rate remained elevated at some level above baseline after epidural stimulation had been turned off. These four clusters differed only in the variability or level of the changes in respiratory frequency. Cluster 2 contained 6 of the 24 animals studied (**Fig 6-5Dii**), and in this cluster there was an initial increase in respiratory frequency that was not sustained after stimulation ceased. Cluster 5 contained 2 animals (**Fig 6-5Dv**) in which epidural stimulation did not alter respiratory frequency, but respiratory frequency rose and was sustained after epidural stimulation ceased. The final cluster contained only 1 animal (**Fig 6-5Dvi**) in which the respiratory frequency rose during epidural stimulation, and respiratory frequency was quite variable in the period following epidural stimulation. Even in clusters 2 and 5, all of the animals had some increase in respiratory frequency at some point during or immediately after epidural stimulation. In contrast, 23 of the 24 animals in the sham stimulation group had no discernible change in respiratory frequency.

Stimulation with 1.5 mA at C3 increased the number of sighs

The number of sighs also increased significantly when mice received epidural stimulation of 1.5 mA at C3 compared to sham stimulation (Figure 6; see *, $p = 0.0011$). There was an increase in the number of sighs during stimulation compared to the pre-stimulation baseline ($p = 0.002$), and also during the 3 mins post-stimulation compared to the pre-stimulation baseline ($p < 0.0001$). Therefore, the number of sighs was elevated for up to 3 minutes after stimulation before returning to pre-stim baseline levels, but sighing diminished in many animals within 3 minutes after epidural stimulation stopped. These results differed from the eupneic respiratory frequency response where respiratory frequency was elevated for a more substantial part of the post-stimulation period and showed little evidence of abating in 18 of the 24 animals studied (clusters 1, 2, 4, 5 and 6).

No correlation between patterns of sigh and eupnea frequency when stimulated with 1.5 mA at C3.

We assessed whether there was any correlation between the pattern of sigh and eupnea frequency responses after stimulation with 1.5 mA at C3. When each animal was stimulated, the pattern of sighing fell into one of four categories (much like the eupneic clusters). We simplified the categories of sigh and eupneic responses such that the categories included (1) no change during stimulation and no change after stimulation (only sighing clusters fulfilled these criteria), (2) no change during stimulation, but increased respiratory frequency post-stimulation (e.g., eupnea cluster, 5) (3) increased during stimulation, but without a sustained post-stimulation increase in respiratory frequency (e.g., cluster 3) and (4) increased during stimulation and sustained for some part of the post-stimulation period (e.g., all the remaining eupnea clusters). We compared the sigh response pattern and the eupnea response patterns of

each mouse during and after epidural stimulation and found no correlation between the pattern of frequency change of eupnea and the pattern of change of sigh frequency (Figure 7). In only 8 of 24 animals were the patterns of sighing and eupneic responses similar.

Discussion

The brainstem has been recognized as the main site for the generation of rhythmic respiratory drive based on a long history of studies in intact, anesthetized and decerebrate animals (21, 31, 32) and more recently on experiments using neonatal *in vitro* preparations (13, 28). The respiratory neurons are distributed in a number of different nuclei in the brainstem throughout the dorsal and ventral regions of the medulla and pons, and neurons within each nucleus make a unique and time dependent contribution to the generation of the pattern of respiratory activity. While not yet definitive, the cervical spinal cord may also contribute to respiratory rhythm generation, as spontaneous rhythmic breathing occurs in cervical spinalized dogs (6) and cats (1). Further, *in vitro* studies have demonstrated the presence of inspiratory and pre-inspiratory neurons at the level of upper cervical spinal cord (9, 18, 22, 26). However, *in vitro* studies, in artificial and reduced preparations do not fully recapitulate the physiological respiratory circuit for eupnea. The neural circuit generating and shaping eupnea is a large and complex network of interacting neurons that integrate multitude of afferent inputs and endogenously generated neural activity among multiple pontine, medullary and possibly spinal cervical locations. Therefore, we used epidural stimulation of the dorsal surface of the cervical spinal cord to assess the contribution of different cervical segments to respiratory neurogenesis in intact, anesthetized mice.

To our knowledge, this is the first study that examined respiratory function related to the

cervical spinal cord in a whole mouse. Previous studies have used *in vitro* slice preparations or whole spinal cord/brain stem explants (18, 28). By utilizing epidural stimulation in the cervical spinal cord, we found that 1.5 mA stimulation at C3 evoked a significant respiratory change; 1.5 mA stimulation at C3 increased the respiratory frequency during epidural stimulation, and in many animals, respiratory frequency remained elevated after epidural stimulation ceased. Tidal volume was not affected by epidural stimulation, but minute ventilation increased significantly. These respiratory frequency responses were only seen when epidural stimulation was delivered at C3 and not at levels C0 through C2 or C4 and C5. In contrast, tidal volume did not change during or after epidural stimulation at C3 or any other cervical level tested. The number of sighs also increased during epidural stimulation at C3, and the increase in sigh frequency also persisted after epidural stimulation stopped, but the facilitation of post-stimulation sighing was less persistent than the post-stimulation facilitation of the eupneic rhythm. Finally, there were differences among the responses of individual animals, and there appeared to be a clustering of respiratory frequency responses that largely reflected the timing and durability of the change in respiratory frequency during and after epidural stimulation.

We discovered that 1.5 mA, 20 Hz epidural stimulation delivered at the level of C3 significantly increased the respiratory frequency, but not the tidal volume. The location of this responsive center at C3 appears to be caudal to the C2 segment that demarcated the caudal border of high cervical respiratory group as defined by optical signals from a brainstem-spinal cord preparation (26). This may indicate that there are heretofore unrecognized elements of the respiratory CPG caudal to C2, or there may be unique electrophysiological properties at C3 that allow current administered at C3 to influence more rostral respiratory CPG function without the C3 region possessing CPG activity of its own. If the response to stimulation at C3 were derived from current spread to C2 and more rostral

elements, we might have expected direct stimulation of C1 and C2 to have a larger effect on respiratory frequency, and we found no effect of epidural stimulation at these spinal levels at all or the stimulation was fatal to the mouse.

The spinal cord is segmentally organized, and there is a tendency to focus on the repetitive, similarity of each spinal segment. The unique susceptibility of the C3 level to modulation by epidural stimulation suggests that there are specific, non-segmentally repeated elements at C3 that contribute to or are part of the neural systems that generate eupnea and sighing. The restricted focality of the response to epidural stimulation argues against the idea that we might have activated more rostral brainstem structures directly (central chemoreceptors, carotid body afferents, etc.)

On the other hand, one unique feature of the C3 locus is that it is a site of integration of sensory information particularly related to the spinal trigeminal nucleus (STN) (2, 24). At the level of the medulla, STN, hypoglossal nucleus, and pre-Bötzinger complex are all reasonably close together and possess well-established reciprocal connections (13). It is possible that stimulation of C3 activates the afferent sensory fibers of STN which then influence the respiratory rhythm. There may be other tracts that are activated by C3 stimulation (e.g. medial longitudinal fasciculus) that integrate and coordinate the activity of brainstem nuclei. For example, the phrenic nerves carry afferents as well as the motor nerves to the diaphragm, and this afferent information does enter the spine at or near C3. Modulation of these afferents is another potential source of information projecting rostrally to respiratory control centers in the brainstem. Although it is interesting that any rostrally projecting axons of passage might have been affected by epidural stimulation, there was no increase in respiratory activity when the C1 and C2 levels were stimulated, which argues against simple activation of rostrally projecting axons of passage. Thus, elucidating the mechanism(s) of respiratory responses to epidural stimulation at C3 and determining what unique features of

C3 generate this response will require further studies.

The mechanism of modulation of the cervical respiratory network is likely through the interneuronal cervical respiratory circuit rather than direct phrenic motor neuron activation as there was no tonic respiratory muscle contraction during eupnea during epidural stimulation, but rather an increase in respiratory frequency. We performed a cluster analysis of the patterns of respiratory sigh activity. The cluster analysis of pre-, intra-, and post-stimulation conditions and sigh data also support the proposed mechanism of accessing the cervical interneuronal network rather than direct phrenic motor neuron activation as the frequency of sighing was also modulated, and sighs were present rather than unaffected or absent. The increase in sigh frequency during C3 stimulation (Figure 4) along with clustering of respiratory patterns (Figure 5) support the idea that the C3-brainstem respiratory circuit is connected and integrated with the ponto-medullary respiratory CPG since epidural stimulation affected the frequency of eupnea and the frequency of sighs, both of which have the CPGs within the brainstem. Moreover, the pattern of responses to epidural stimulation of eupnea and sighing were not correlated in individual animals. It seems unlikely that complete and separate CPGs for sighing and eupnea would be represented in the cervical spine, and so the dual effect of epidural stimulation strongly favors the hypothesis that cervical spinal neurons are part of an extended set of respiratory CPGs throughout the brainstem and upper cervical spine that support both sighing and eupnea. That two forms of respiratory activity were modified by epidural stimulation at C3 also makes it unlikely that the respiratory responses arose from a direct effect on motor neurons, which would have been expected to modify the duration or intensity of inspiratory and/or expiratory muscle activity, which we did not see. Sighing has been associated with the retrotrapezoid nucleus/parafacial respiratory group (RTN/pFRG) and projects to preBötC (27), while eupnea is related to a complex interaction of brainstem respiratory nuclei (21, 30). Stimulation of a topographically distinct

location in the cervical spine with associated alterations in both eupneic and sighing frequency and respiratory pattern suggests a reciprocally connected circuit between the respiratory centers for sighing and eupnea and the spinal cord and brainstem. The data gathered here are consistent with a hierarchical model of independent CPGs related to respiratory function in which the C3 region is a node or nexus of access to the respiratory circuit.

The results presented demonstrate some of the advantages of studying intact animals, but there are limitations as well, especially in mice. We were not able to measure or control the arterial CO_2 or arterial O_2 levels in these animals. The oxygen saturation was stable, but since minute ventilation increased during and after epidural stimulation at C3, it is possible, even likely, that some degree of hypocapnia developed during these studies. Hypocapnia may be associated with increased sighing in humans (33), though whether this is a cause or an effect of sighing is unclear. Sigh frequency in rodents was unresponsive to changes in inspired CO_2 (3). Nevertheless, we cannot rule out the possibility that changes in O_2 or CO_2 levels may have contributed to the increase in sigh frequency during or after epidural stimulation. In future studies, it will be important to control the levels of arterial O_2 and CO_2 to understand the origins of the frequency responses to epidural stimulation. Last, we only measured heart rate, and not blood pressure. Nevertheless, we found no evidence that changes in cardiovascular function might alter the respiratory activity that we observed.

Interestingly, we discovered that there is an impact of stimulation on respiratory frequency that persists after removal of the stimulation. Such an observation supports the theory that spinal cord stimulation activates the cervical spinal motor circuit and lowers the threshold of activation or resting membrane potential for motor tasks with persistent and residual effects (23). One might imagine that the increased respiratory frequency occurs by facilitation or disinhibition or both. In favor of facilitation, it is noteworthy that a sustained increase in

respiratory frequency, termed long term facilitation, follows intermittent hypoxia (8), and this long term facilitation seemed to depend on serotonergically induced plasticity. The epidural stimulation is clearly different from intermittent hypoxia, but epidural stimulation seemed to induce a similarly sustained increase in respiratory frequency in many of the animals, and serotonin has been used to enhance respiratory and motor function after spinal cord injury through a mechanism of increased spinal excitability and state permissive for motor activation (5, 7, 15). Disinhibition is also a possible mechanism of increasing the frequency of eupnea and gasping, and there are many GABAergic interneurons at each segmental level of the spine, which may have been modulated by epidural stimulation so as to allow a sustained increase in respiratory frequency. Moreover, there are examples of increased respiratory activity following spinal injury that have been attributed to disinhibition of these spinal interneurons (20). Defining the roles of facilitation and disinhibition (or both) in the response to epidural stimulation will also require further studies.

Summary.

We found that epidural stimulation of the dorsal spinal cord at the C3 level increased the frequency of eupnea and sighing. Stimulation at no other cervical level from the caudal medulla to C5 had any effect on either eupnea or sighing. For both eupnea and sighing, the increase in frequency persisted after epidural stimulation ceased in many animals. The duration of post-stimulation frequency facilitation was greater for eupnea than sighing. These findings suggest that spinal elements at the C3 level make a unique and heretofore unappreciated contribution to respiratory frequency generation for both eupnea and sighing, probably through an interaction with or participation in the CPGs for eupnea and sighing. The mechanisms of the responses to epidural stimulation merit further study to elucidate the therapeutic potential of cervical epidural stimulation in individuals with spinal cord injuries.

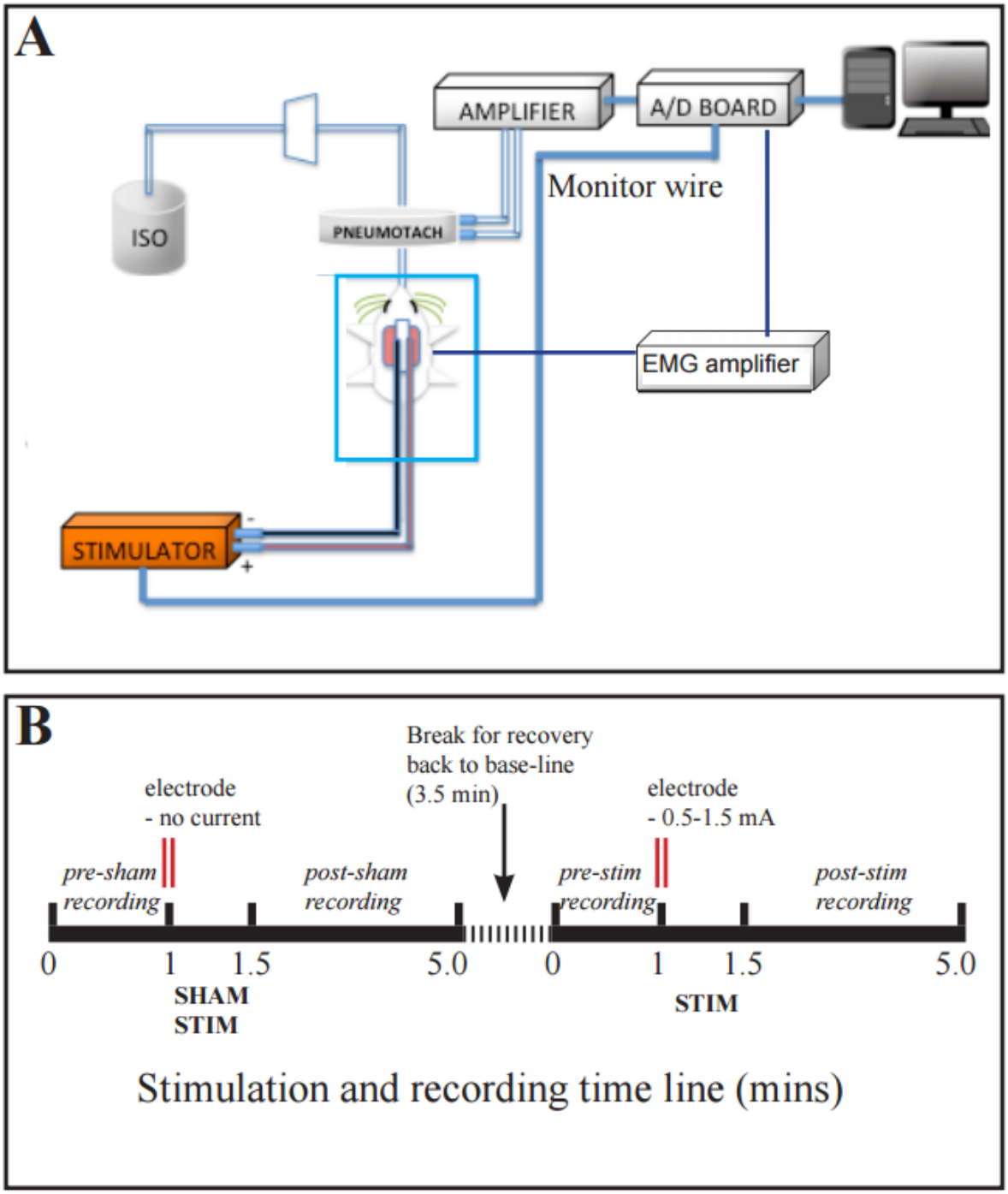

Figure 6- 1

Figure 6-1. **Experimental set-up.** In (A), the experimental set-up used in this study is shown, (B) shows the epidural stimulation sites on dorsal lateral spinal cord, and (C) shows the

recording time line for each cervical level, with sham experiment recorded first followed by stimulation.

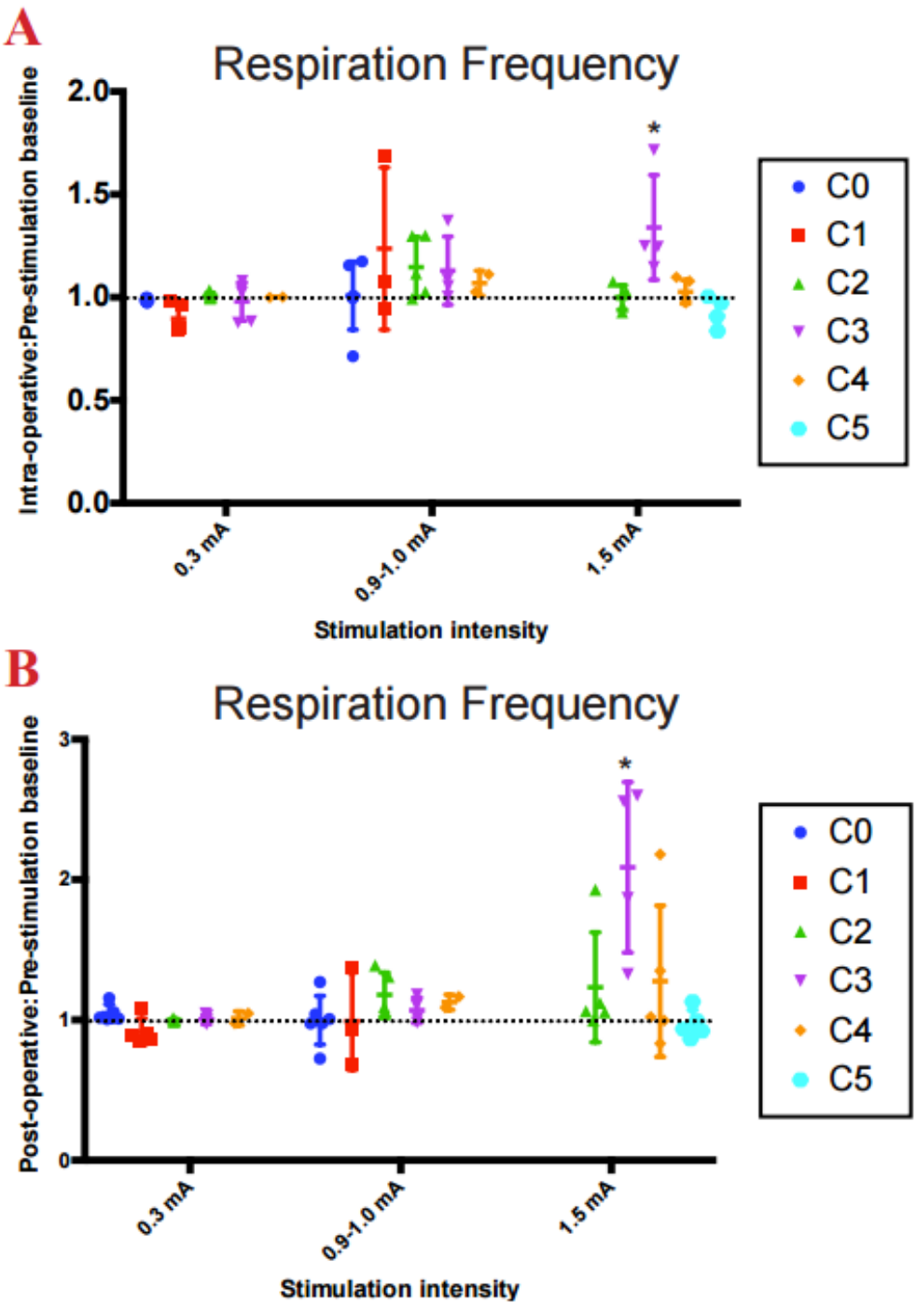

Figure 6- 2

Figure 6-2. Epidural stimulation at C1 at 20Hz and 1.5 mA intensity resulted in immediate, strong respiration (an apnea), followed by intermittent and ineffective respiratory activity and then bradycardia and apparent cardiovascular collapse.

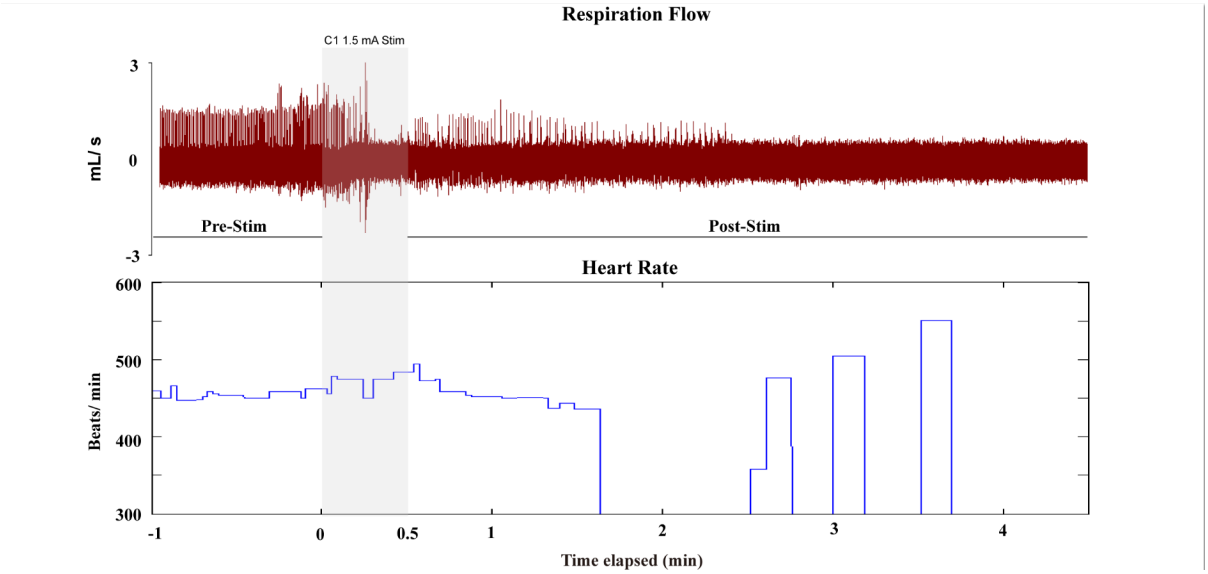

Figure 6- 3

Figure 6-3. **Determining the current intensity to use for each cervical level tested.** The electrical stimulation intensities used were 0.3, 0.9-1.0 or 1.5 mA. A) The respiratory frequency ratio of intra-operative recording compared to the pre-stimulation baseline is shown, and B) the respiration frequency ratio of post-stimulation recording compared to the pre-stimulation baseline is shown. In both analyses, the stimulation intensity of 1.5 mA at C3 caused the only significant increase in the respiratory ratio (see *). For C0 and C1, the stimulation intensity of 1.5mA was too strong and induced cardiac arrest. For C5, only 1.5 mA was tested as the location was close to a major blood vessel that impeded the recording.

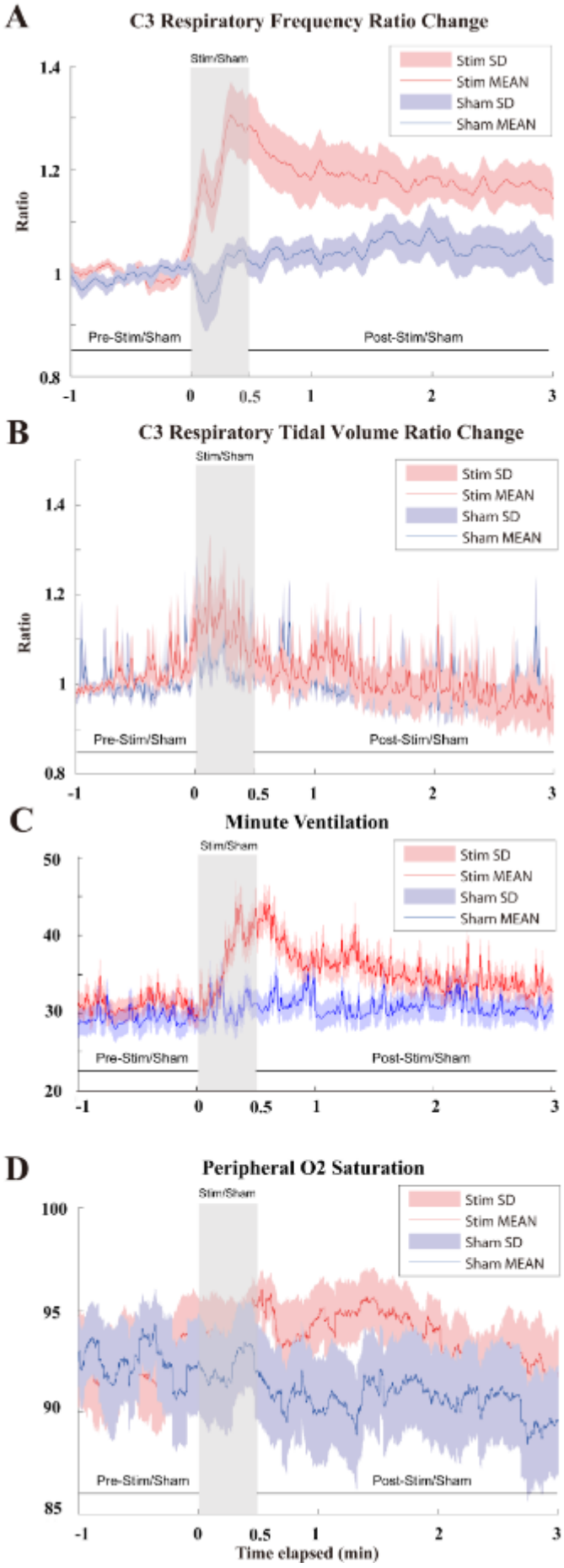
A
C3 Respiratory Frequency Ratio Change
Stim/Sham
Stim SD
Stim MEAN
Sham SD
Sham MEAN
Ratio
1.4
1.2
1
0.8
Pre-Stim/Sham
Post-Stim/Sham
-1
0
0.5
1
2
3
B
C3 Respiratory Tidal Volume Ratio Change
Stim/Sham
Stim SD
Stim MEAN
Sham SD
Sham MEAN
Ratio
1.4
1.2
1
0.8
Pre-Stim/Sham
Post-Stim/Sham
-1
0
0.5
1
2
3
C
Minute Ventilation
Stim/Sham
Stim SD
Stim MEAN
Sham SD
Sham MEAN
50
40
30
20
Pre-Stim/Sham
Post-Stim/Sham
-1
0
0.5
1
2
3
D
Peripheral O2 Saturation
Stim/Sham
Stim SD
Stim MEAN
Sham SD
Sham MEAN
100
95
90
85
Pre-Stim/Sham
Post-Stim/Sham
-1
0
0.5
1
2
3
Time elapsed (min)

Figure 6- 4

Figure 6-4. **Respiratory frequency increased when C3 was stimulated (20 Hz, 1.5 mA).** (A) shows the respiratory frequency change when C3 was electrically stimulated or a sham stimulation was carried out. (B) shows the respiratory peak-to-peak amplitude ratio change when C3 was electrically stimulated or a sham stimulation was carried out. The ratio was calculated using each recorded data point compared to the calculated baseline median. (n=24). The respiratory frequency was significantly increased during epidural stimulation compared to sham stimulation ($p<0.05$). However, there was no change in respiratory peak to peak amplitude during epidural stimulation compared to the sham stimulation. (C) C3 20Hz 1.5mA electrical epidural stimulation increased minute ventilation. The minute ventilation is calculated by multiplying the respiration frequency and the tidal volume. The minute ventilation increased significantly during and 1.41 min post the stimulation (*: $p<0.05$, p1= 0.01137, p2= 0.04027). n=24.

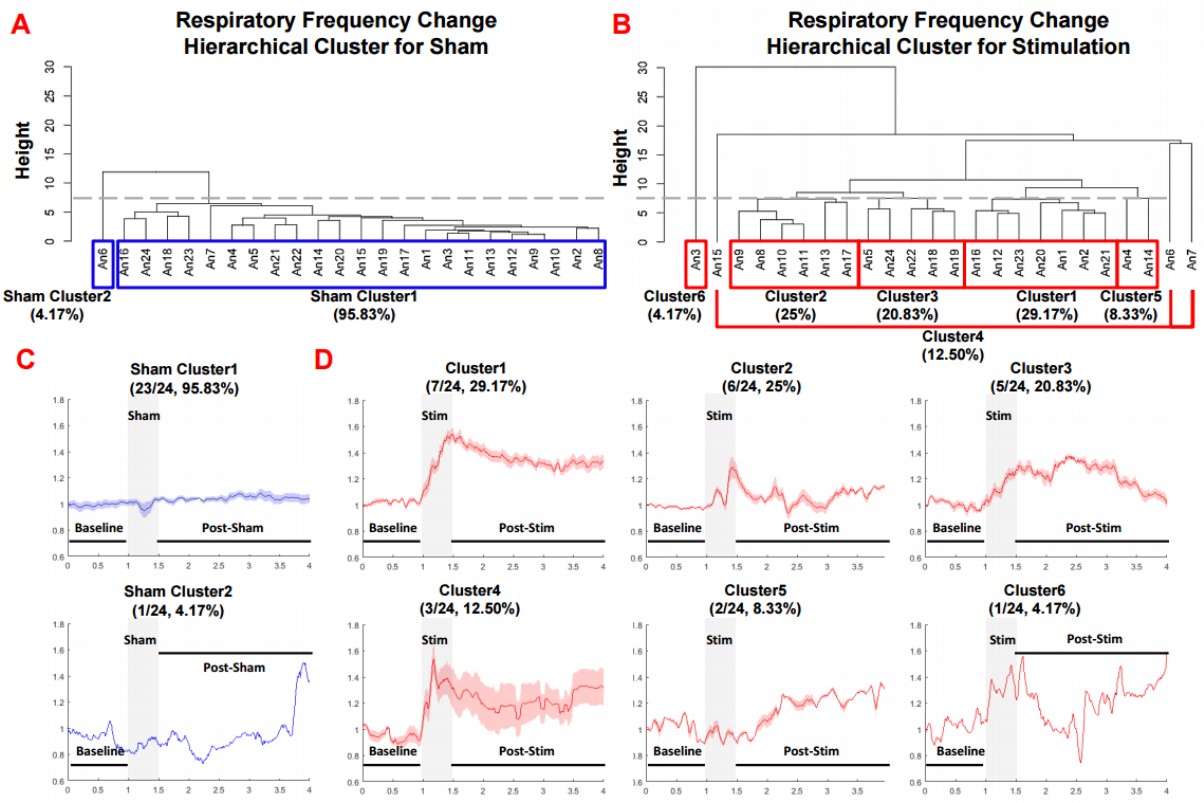

Figure 6- 5

Figure 6-5. **Hierarchical cluster showing different respiratory frequency change pattern due to epidural stimulation at C3 with 1.5 mA.** The hierarchical cluster dendograms of the sham group (A) and the epidural stimulation group (B) are shown above. Individual recordings were placed in separate clusters if the distance between each tracing was greater than 7.5 hierarchical units (An = animal). (C) Tracings of the average clusters for the sham group: (i) sham cluster 1, which consisted of data from 23 of 24 animals, and (ii) sham cluster 2 which contained data from only 1 animal. (D) Tracings of the average clusters for the epidural stimulation group: (i) cluster 1 contained 7 of 24 animals, (ii) cluster 2 contained 6 of 24 animals, (iii) cluster 3 contained 5 of 24 animals, (iv) cluster 4 contained 3 of 24 animals, (v) cluster 5 contained 2 of 24 animals and (vi) cluster 6 contained only 1 animal.

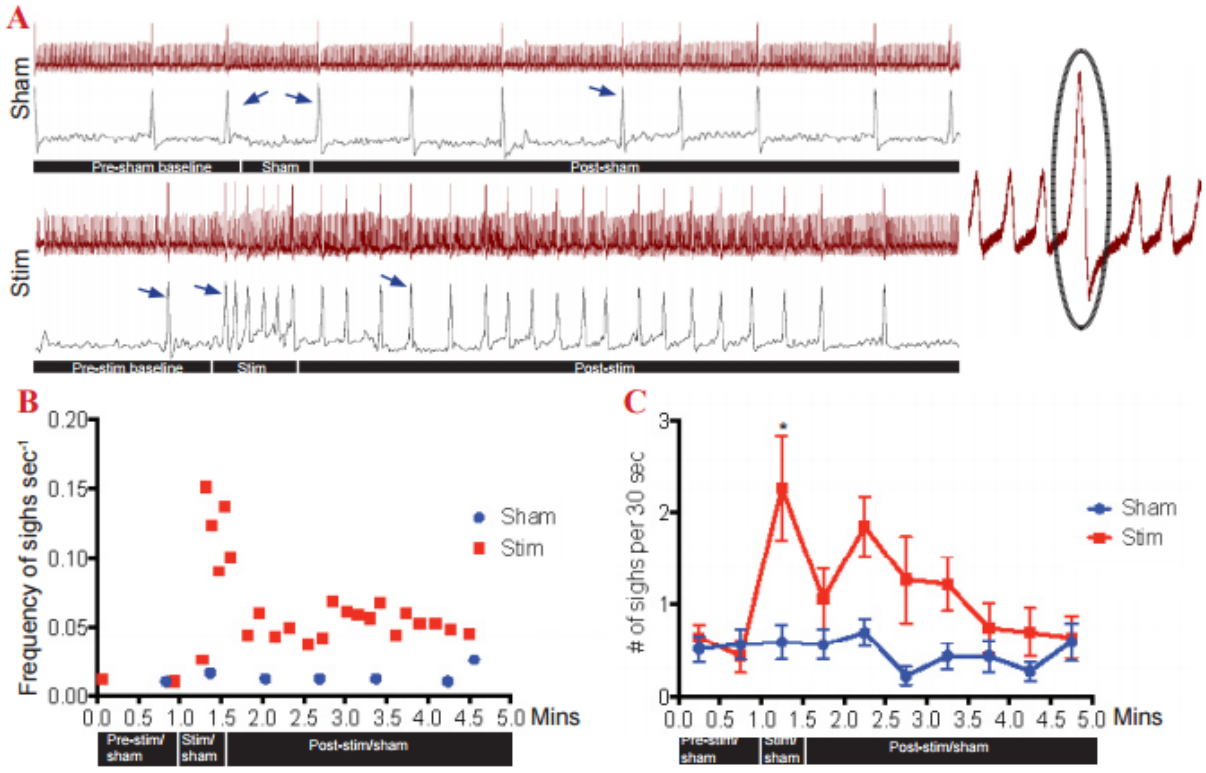

Figure 6- 6

Figure 6-6. **Stimulation at C3 (20 Hz, 1.5 mA) alters sigh frequency.** (A) is a representative trace showing the recorded tidal volume (red trace) and smoothed tidal volume (black trace) of respiration pre-stimulation, during sham or during epidural stimulation and after sham or epidural stimulation. The peaks (see blue arrows) indicate sighs, and a representative sigh is shown in detail (black dash circle on the right). (B) shows a representation of the frequency of sighs per second depending on whether sham stimulation or epidural stimulation was used. (C) shows the number of sighs for every 30 seconds in all the mice tested (n=19) either pre-stimulation, during sham or during epidural stimulation and after sham or epidural stimulation. The number of sighs was greater during epidural stimulation compared to the pre-stimulation, baseline period ($p = 0.002$); significantly greater during epidural stimulation was delivered compared to the same period during sham

stimulation (p = 0.0011, see asterisk); and sigh frequency remained significantly elevated for up to 3 min after epidural stimulation stopped compared to sham (p < 0.001, see asterisk).

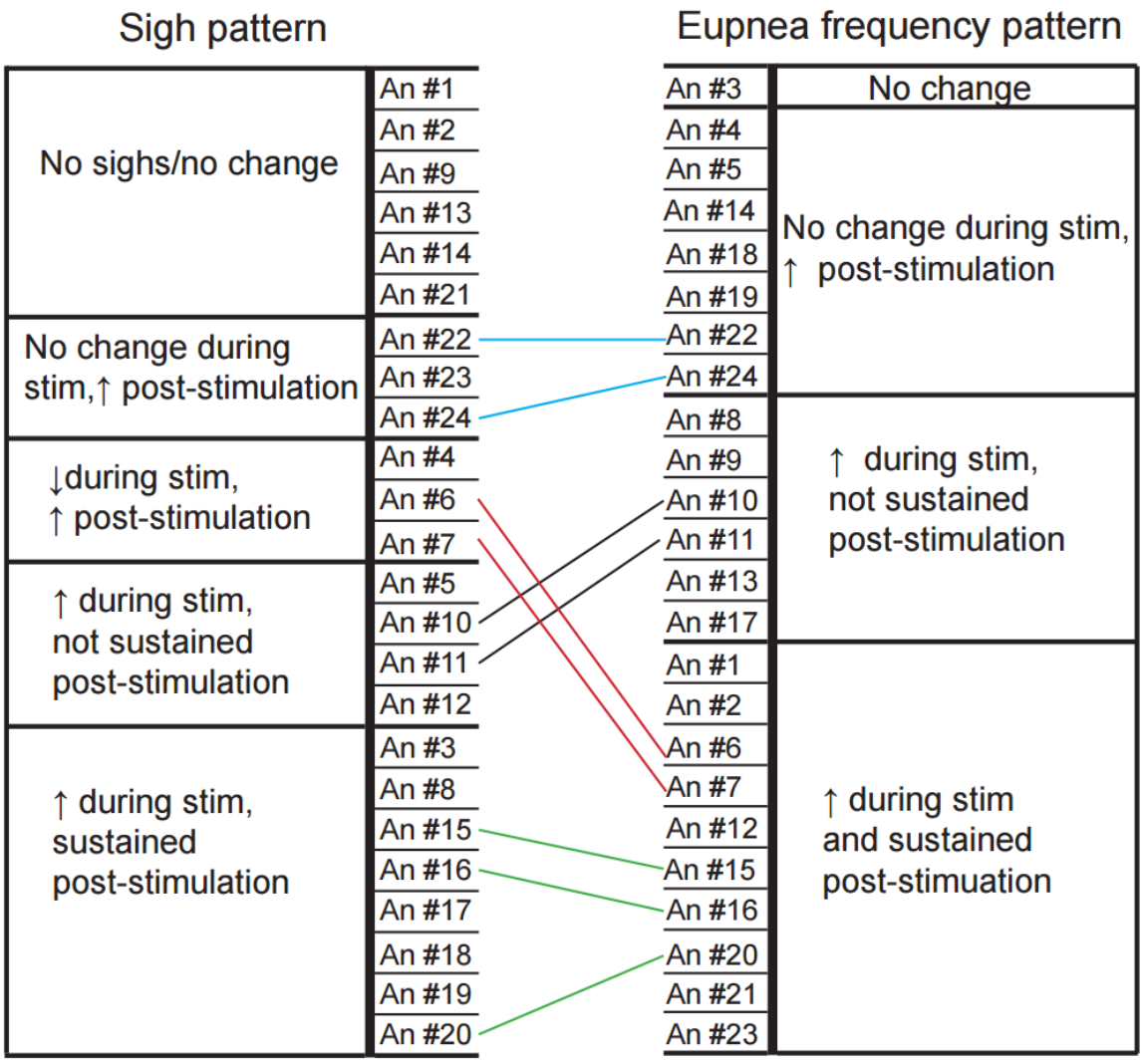

Figure 6- 7

Figure 6-7. **Sigh and eupnea response after stimulation is not correlated.** The left side of the chart shows the pattern of sigh clustering based on the response to stimulation compared to pre-stimulation sigh baseline. The right side of the chart shows eupnea frequency clustering based on the response to epidural stimulation compared to the pre-stimulation eupnea baseline. Each animal appears on each side of the figure according to the pattern of sighing and eupneic responses, and those animals in which the pattern of changes in sigh and

eupnea were similar during and after epidural stimulation are printed in bold, red text. The effects of epidural stimulation on the frequency of eupnea and sighs seemed to be uncorrelated in individual animals in that 16 of 24 animals had different sigh and eupneic responses patterns to epidur

REFERENCE

1. Joseph, M. S. *et al.* Treadmill training stimulates BDNF mRNA expression in motor neurons of the lumbar spinal cord in spinally transected rats. *Neuroscience* **8,** 135–144 (2012).

2. Manuscript, A. & Nanostructures, S. P. C. NIH Public Access. *Nano* **6,** 2166–2171 (2008).

3. Serrano-Pozo, A., Frosch, M. P., Masliah, E. & Hyman, B. T. Neuropathological alterations in Alzheimer disease. *Cold Spring Harb. Perspect. Med.* **1,** 1–23 (2011).

4. Alzheimer, A., Bick, K., Amaducci, L., Pepeu, G. (Eds. . A characteristic disease of the cerebral cortex. In:The Early Story of Alzheimer's Disease. *Liviana Press. Padova, Italy,* **pp. 1–3. A,** (1907).

5. Allsop, D., Landon, M., Kidd, M. The isolation and amino acid composition of senile plaque core protein. *Brain Res.* **259,** 348–352 (1983).

6. Kang, J. *et al.* The precursor of Alzheimer's disease amyloid A4 protein resembles a cell-surface receptor. *Nature* **325,** 733–736 (1987).

7. Hardy, J. & Allsop, D. Amyloid deposition as the central event in the aetiology of Alzheimer's disease. *Trends Pharmacol. Sci.* **12,** 383–388 (1991).

8. Sherrington, R. *et al.* Cloning of a gene bearing missense mutations in early-onset familial Alzheimer's disease. *Nature* **375,** 754–760 (1995).

9. Cruts M, Hendriks L, V. B. C. The presenilin genes: a new gene family involved in Alzheimer disease pathology. *Hum. Mol. Genet.* **5,** 1449–1455 (1996).

10. Levy-lahad, E. *et al.* Candidate Gene for the Chromosome 1 Familial Alzheimer ' s Disease Locus. *Science (80-.).* **269,** 973–977 (1995).

11. Rogaev, E. I. *et al.* Familial Alzheimer's disease in kindreds with missense mutations in a gene on chromosome 1 related to the Alzheimer's disease type 3 gene. *Nature* **376,** 775–778 (1995).

12. Alzheimer's Disease Collaborative Group. The structure of the presenilin 1 (S182) gene and identification of six novel mutations in early onset AD families. *Nat Genet* **11,** 219–222 (1995).

13. Hutton, M. & Hardy, J. The presenilins and Alzheimer's disease. *Hum. Mol. Genet.* **6,** 1639–1646 (1997).

14. Zhong, N. & Weisgraber, K. H. Understanding the association of apolipoprotein E4 with Alzheimer disease: Clues from its structure. *J. Biol. Chem.* **284,** 6027–6031 (2009).

15. Chen, J., Li, Q. & Wang, J. Topology of human apolipoprotein E3 uniquely regulates its diverse biological functions. *Proc. Natl. Acad. Sci. U. S. A.* **108,** 14813–8 (2011).

16. Frieden, C. & Garai, K. Structural differences between apoE3 and apoE4 may be useful in developing therapeutic agents for Alzheimer's disease. *Proc. Natl. Acad. Sci.* **109,** 8913–8918 (2012).

17. Lin, G. G. & Scott, J. G. Apolipoprotein E and Alzheimer disease: risk, mechanisms, and therapy. **100,** 130–134 (2012).

18. Naidoo, A., Naidoo, K., Yende-zuma, N. & Gengiah, T. N. NIH Public Access. **19,** 161–169 (2015).

19. Giacobini, E. & Gold, G. Alzheimer disease therapy--moving from amyloid-β to tau. *Nat. Rev. Neurol.* **9,** 677–86 (2013).

20. Tortosa, E. *et al.* Microtubule-associated protein 1B (MAP1B) is required for dendritic spine development and synaptic maturation. *J. Biol. Chem.* **286,** 40638–40648 (2011).

21. Grundke-Iqbal, I. *et al.* Abnormal phosphorylation of the microtubule-associated protein tau (tau) in Alzheimer cytoskeletal pathology. *Proc. Natl. Acad. Sci. U. S. A.* **83,** 4913–7 (1986).

22. Grundke-iqbal, I. *et al.* ASSEMBLY IN ALZHEIMER ' S DISEASE Failure of Microtubule Assembly from Alzheimer Brain. 421–426 (1985).

23. Iqbal, K. *et al.* Identification and localization of a tau peptide to paired helical filaments of Alzheimer disease. *Proc Natl Acad Sci U S A* **86,** 5646–5650 (1989).

24. Lee, V. M., Balin, B. J., Otvos, L. & Trojanowski, J. Q. A68: a major subunit of paired helical filaments and derivatized forms of normal Tau. *Science* **251,** 675–678 (1991).

25. Morris, M. *et al.* Tau post-translational modifications in wild-type and human amyloid precursor protein transgenic mice. *Nat Neurosci* **18,** 1183–1189 (2015).

26. Gomez-Isla, T. *et al.* Neuronal loss correlates with but exceeds neurofibrillary tangles in Alzheimer's disease. *Ann Neurol* **41,** (1997).

27. Kamenetz, F. *et al.* APP processing and synaptic function. *Neuron* **37,** (2003).

28. Nalivaeva, N. N. & Turner, A. J. The amyloid precursor protein: A biochemical enigma in brain development, function and disease. *FEBS Lett.* **587,** 2046–2054 (2013).

29. van der Kant, R. & Goldstein, L. S. B. Cellular Functions of the Amyloid Precursor Protein from Development to Dementia. *Dev. Cell* **32,** 502–515 (2015).

30. Dewachter, I. *et al.* Deregulation of NMDA-receptor function and down-stream signaling in APP[V717I] transgenic mice. *Neurobiol Aging* **30,** (2009).

31. Turner, P. R., O'Connor, K., Tate, W. P. & Abraham, W. C. *Roles of amyloid precursor protein and its fragments in regulating neural activity, plasticity and memory*. *Progress in Neurobiology* **70,** (2003).

32. Hermann, D. *et al.* Synaptic transmission is impaired prior to plaque formation in amyloid precursor protein-overexpressing mice without altering behaviorally-correlated sharp wave-ripple complexes. *Neuroscience* **162,** (2009).

33. Hu, N. W., Smith, I. M., Walsh, D. M. & Rowan, M. J. Soluble amyloid-beta peptides potently disrupt hippocampal synaptic plasticity in the absence of cerebrovascular dysfunction in vivo. *Brain* **131,** (2008).

34. Hung, L. W. *et al.* Amyloid-beta peptide (Abeta) neurotoxicity is modulated by the rate of peptide aggregation: Abeta dimers and trimers correlate with neurotoxicity. *J Neurosci* **28,** (2008).

35. Gong, Y. *et al.* Alzheimer's disease-affected brain: presence of oligomeric Abeta ligands (ADDLs) suggests a molecular basis for reversible memory loss. *Proc. Natl. Acad. Sci.* **100,** (2003).

36. Kelly, B. L. & Ferreira, A. beta-Amyloid-induced dynamin 1 degradation is mediated by N-methyl-D-aspartate receptors in hippocampal neurons. *J Biol Chem* **281,** (2006).

37. Lue, L. F. *et al.* Soluble amyloid beta peptide concentration as a predictor of synaptic change in Alzheimer's disease. *Am J Pathol* **155,** (1999).

38. Li, S. *et al.* Soluble oligomers of amyloid Beta protein facilitate hippocampal long-term depression by disrupting neuronal glutamate uptake. *Neuron* **62,** (2009).

39. McLean, C. A. *et al.* Soluble pool of Abeta amyloid as a determinant of severity of neurodegeneration in Alzheimer's disease. *Ann Neurol* **46,** (1999).

40. Shankar, G. M. *et al.* Natural oligomers of the Alzheimer amyloid-beta protein induce reversible synapse loss by modulating an NMDA-type glutamate receptor-dependent signaling pathway. *J Neurosci* **27,** (2007).

41. Shankar, G. M. *et al.* Amyloid-beta protein dimers isolated directly from Alzheimer's brains impair synaptic plasticity and memory. *Nat Med* **14,** (2008).

42. Shrestha, B. R. *et al.* Amyloid beta peptide adversely affects spine number and motility in hippocampal neurons. *Mol Cell Neurosci* **33,** (2006).

43. Barghorn, S. *et al.* Globular amyloid beta-peptide oligomer-a homogenous and stable neuropathological protein in Alzheimer's disease. *J Neurochem* **95,** (2005).

44. Busche, M. A. *et al.* Clusters of hyperactive neurons near amyloid plaques in a mouse model of Alzheimer's disease. *Science (80-.).* **321,** (2008).

45. Brody, D. L. *et al.* Amyloid-beta dynamics correlate with neurological status in the injured human brain. *Science (80-.).* **321,** (2008).

46. Cleary, J. P. *et al.* Natural oligomers, but not monomers, of the amyloid $β$-protein specifically disrupt the memory of learned behavior. *Nat. Neurosci.* **8,** (2005).

47. Dahlgren, K. N. *et al.* Oligomeric and fibrillar species of amyloid-$β$ peptides differentially affect neuronal viability. *J Biol Chem* **277,** (2002).

48. Enya, M. *et al.* Appearance of sodium dodecyl sulfate-stable amyloid beta-protein (Abeta) dimer in the cortex during aging. *Am J Pathol* **154,** (1999).

49. Mucke, L. *et al.* High-level neuronal expression of abeta 1-42 in wild-type human amyloid protein precursor transgenic mice: synaptotoxicity without plaque formation. *J Neurosci* **20,** (2000).

50. Podlisny, M. B. *et al.* Aggregation of secreted amyloid beta-protein into sodium dodecyl sulfate-stable oligomers in cell culture. *J Biol Chem* **270,** (1995).

51. Walsh, D. M., Tseng, B. P., Rydel, R. E., Podlisny, M. B. & Selkoe, D. J. The oligomerization of amyloid beta-protein begins intracellularly in cells derived from human brain. *Biochemistry* **39,** (2000).

52. Wang, J., Dickson, D. W., Trojanowski, J. Q. & Lee, V. M. The levels of soluble versus insoluble brain Abeta distinguish Alzheimer's disease from normal and pathologic aging. *Exp Neurol* **158,** (1999).

53. O'Brien, R. & Wong, P. Amyloid precursor protein processing and alzheimer's disease. *Annu. Rev. Neurosci.* **1987,** 185–204 (2011).

54. Joshi, P., Liang, J. O., DiMonte, K., Sullivan, J. & Pimplikar, S. W. Amyloid precursor protein is required for convergent-extension movements during Zebrafish development. *Dev. Biol.* **335,** 1–11 (2009).

55. Tyan, S.-H. *et al.* Amyloid precursor protein (APP) regulates synaptic structure and function. *Mol.Cell Neurosci.* **51,** 43–52 (2012).

56. Wang, Q. *et al.* Many Neuronal and Behavioral Impairments in Transgenic Mouse Models of Alzheimer's Disease Are Independent of Caspase Cleavage of the Amyloid Precursor Protein. **27,** 380–392 (2014).

57. Barnes, N. Y. *et al.* Increased production of amyloid precursor protein provides a substrate for caspase-3 in dying motoneurons. *J. Neurosci.* **18,** 5869–80 (1998).

58. Magara, F. *et al.* Genetic background changes the pattern of forebrain commissure defects in transgenic mice underexpressing the beta-amyloid-precursor protein. *Proc. Natl. Acad. Sci. U. S. A.* **96,** 4656–4661 (1999).

59. Dawson, G. R. *et al.* Age-related cognitive deficits, impaired long-term potentiation and reduction in synaptic marker density in mice lacking the ??-amyloid precursor protein. *Neuroscience* **90,** 1–13 (1999).

60. Zheng, H. *et al.* p-Amyloid Precursor Protein-Deficient Show Reactive Gliosis and Decreased Locomotor Activity. **81,** 525–531 (1995).

61. Smith, K. D. B., Peethumnongsin, E., Lin, H., Zheng, H. & Pautler, R. G. Increased Human Wildtype Tau Attenuates Axonal Transport Deficits Caused by Loss of APP in Mouse Models. *Magn. Reson. Insights* **4,** 11–18 (2010).

62. Kamal, a, Almenar-Queralt, a, LeBlanc, J. F., Roberts, E. a & Goldstein, L. S. Kinesin-mediated axonal transport of a membrane compartment containing beta-secretase and presenilin-1 requires APP. *Nature* **414,** 643–648 (2001).

63. Heber, S. *et al.* Mice with Combined Gene Knock-outs Reveal Essential and Partially

Redundant Functions of Amyloid Precursor Protein Family Members. *J. Neurosci.* **20,** 7951–7963 (2000).

64. Walsh, D. M. *et al.* Amyloid $β$-protein fibrillogenesis: Detection of a protofibrillar intermediate. *J Biol Chem* **272,** (1997).

65. Shankar, G. M. & Walsh, D. M. Alzheimer's disease: synaptic dysfunction and A$β$. *Mol. Neurodegener.* **4,** 48 (2009).

66. Selkoe, D. J. Alzheimer's disease: genes, proteins, and therapy. *Physiol Rev* **81,** (2001).

67. Walsh, D. M. *et al.* Certain inhibitors of synthetic amyloid beta-peptide (Abeta) fibrillogenesis block oligomerization of natural Abeta and thereby rescue long-term potentiation. *J Neurosci* **25,** (2005).

68. Lambert, M. P. *et al.* Diffusible, nonfribrillar ligands derived from A$β$1-42are potent central nervous system neurotoxins. *Proc Natl Acad Sci USA* **95,** (1998).

69. Lashuel, H. A. *et al.* Mixtures of wild-type and a pathogenic (E22G) form of Abeta40 in vitro accumulate protofibrils, including amyloid pores. *J Mol Biol* **332,** (2003).

70. Harper, J. D., Wong, S. S., Lieber, C. M. & Lansbury, P. T. Assembly of A$β$ amyloid protofibrils: An in vitromodel for a possible early event in Alzheimer's disease. *Biochemistry* **38,** (1999).

71. Nybo, M., Svehag, S. E. & Holm Nielsen, E. An ultrastructural study of amyloid intermediates in A beta1-42 fibrillogenesis. *Scand J Immunol* **49,** (1999).

72. Lewczuk, P. Amyloid-β 42/40 Cerebrospinal Fluid Concentration Ratio in the Diagnostics of Alzheimer's Disease: Validation of Two Novel Assays. *J. Alzheimer's*

Dis. **43,** 183–191 (2015).

73. Dumurgier, J. *et al.* Cerebrospinal fluid amyloid-β 42/40 ratio in clinical setting of memory centers: a multicentric study. *Alzheimers. Res. Ther.* **7,** 30 (2015).

74. Lacor, P. N. *et al.* Abeta oligomer-induced aberrations in synapse composition, shape, and density provide a molecular basis for loss of connectivity in Alzheimer's disease. *J Neurosci* **27,** (2007).

75. Cheng, I. H. *et al.* Accelerating amyloid-beta fibrillization reduces oligomer levels and functional deficits in Alzheimer disease mouse models. *J Biol Chem* **282,** (2007).

76. Tomiyama, T. *et al.* A new amyloid beta variant favoring oligomerization in Alzheimer's-type dementia. *Ann Neurol* **63,** (2008).

77. Davies, C. A., Mann, D. M., Sumpter, P. Q. & Yates, P. O. A quantitative morphometric analysis of the neuronal and synaptic content of the frontal and temporal cortex in patients with Alzheimer's disease. *J Neurol Sci* **78,** (1987).

78. Lesne, S. *et al.* A specific amyloid-beta protein assembly in the brain impairs memory. *Nature* **440,** (2006).

79. Masliah, E. *et al.* Altered expression of synaptic proteins occurs early during progression of Alzheimer's disease. *Neurology* **56,** (2001).

80. Geinisman, Y., deToledo-Morrell, L., Morrell, F., Persina, I. S. & Rossi, M. Age-related loss of axospinous synapses formed by two afferent systems in the rat dentate gyrus as revealed by the unbiased stereological dissector technique. *Hippocampus* **2,** (1992).

81. Hsieh, H. *et al.* AMPAR removal underlies Abeta-induced synaptic depression and dendritic spine loss. *Neuron* **52,** (2006).

82. Klyubin, I. *et al.* Amyloid beta protein dimer-containing human CSF disrupts synaptic plasticity: prevention by systemic passive immunization. *J Neurosci* **28,** (2008).

83. Barghorn, S. *et al.* Structure, microtubule interactions, and paired helical filament aggregation by tau mutants of frontotemporal dementias [In Process Citation]. *Biochemistry* **39,** (2000).

84. Townsend, M., Shankar, G. M., Mehta, T., Walsh, D. M. & Selkoe, D. J. Effects of secreted oligomers of amyloid {{}beta{}}-protein on hippocampal synaptic plasticity: a potent role for trimers. *J Physiol* **572,** (2006).

85. Walsh, D. M. *et al.* Amyloid beta-protein fibrillogenesis. Structure and biological activity of protofibrillar intermediates. *J Biol Chem* **274,** (1999).

86. Koffie, R. M., Hyman, B. T. & Spires-Jones, T. L. Alzheimer's disease: synapses gone cold. *Mol. Neurodegener.* **6,** 63 (2011).

87. Bitan, G. *et al.* Amyloid $β$-protein (A$β$) assembly: A$β$ 40 and A$β$ 42 oligomerize through distinct pathways. *Proc Natl Acad Sci USA* **100,** (2003).

88. Tamagno, E., Bardini, P., Guglielmotto, M., Danni, O. & Tabaton, M. The various aggregation states of beta-amyloid 1-42 mediate different effects on oxidative stress, neurodegeneration, and BACE-1 expression. *Free Radic Biol Med* **41,** (2006).

89. Wang, H. Y., Lee, D. H., Davis, C. B. & Shank, R. P. Amyloid peptide Abeta(1-42) binds selectively and with picomolar affinity to alpha7 nicotinic acetylcholine receptors. *J Neurochem* **75,** (2000).

90. JB, B. Amyloid precursor protein (APP) contributes to pathology in the SOD1(G93A) mouse model of amyotrophic lateral sclerosis. *Hum Mol Genet.* **1,** 3871–82 (2012).

91. Ikonomovic, M. D. *et al.* Alzheimer's pathology in human temporal cortex surgically excised after severe brain injury. *Exp. Neurol.* **190,** 192–203 (2004).

92. Gehrmann, J., Banati, R. B., Cuzner, M. L., Kreutzberg, G. W. & Newcombe, J. Amyloid precursor protein (APP) expression in multiple sclerosis lesions. *Glia* **15,** 141–51 (1995).

93. Hsia, A. Y. *et al.* Plaque-independent disruption of neural circuits in Alzheimer's disease mouse models. *Proc Natl Acad Sci USA* **96,** (1999).

94. Geurts, A. C. H., Ribbers, G. M., Knoop, J. A. & van Limbeek, J. Identification of static and dynamic postural instability following traumatic brain injury. *Arch. Phys. Med. Rehabil.* **77,** 639–644 (1996).

95. Ducker, T. B. Spinal Cord. *Animals* 417–433 (1977).

96. Pajoohesh-Ganji, A. *et al.* Inhibition of amyloid precursor protein secretases reduces recovery after spinal cord injury. *Brain Res.* **1560,** 73–82 (2014).

97. Courtine, G. *et al.* Transformation of nonfunctional spinal circuits into functional states after the loss of brain input. *Nat. Neurosci.* **12,** 1333–1342 (2009).

98. Kiehn, O. Locomotor circuits in the mammalian spinal cord. *Annu. Rev. Neurosci.* **29,** 279–306 (2006).

99. Kiehn, O. Decoding the organization of spinal circuits that control locomotion. *Nat. Rev. Neurosci.* **17,** 224–238 (2016).

100. Kwan, A. C., Dietz, S. B., Webb, W. W. & Harris-Warrick, R. M. Activity of Hb9 Interneurons during Fictive Locomotion in Mouse Spinal Cord. *J. Neurosci.* **29,** 11601–11613 (2009).

101. de Luca, C. J., Foley, P. J. & Erim, Z. Motor unit control properties in constant-force isometric contractions. *J. Neurophysiol.* **76,** 1503–16 (1996).

102. Westgaard, R. H. & de Luca, C. J. Motor unit substitution in long-duration contractions of the human trapezius muscle. *J. Neurophysiol.* **82,** 501–504 (1999).

103. Nagendran, A., Pillat, R., Adam, K., Welch, G. & Hughes, C. A Unitied Framework for Individualized Avatar-Based Interactions. *Presence Teleoperators Virtual Environ.* **23,** 109–132 (2013).

104. Persad, C. C., Jones, J. L., Ashton-miller, J. a, Alexander, N. B. & Giordani, B. Adults With Cognitive Impairment. *America (NY).* **63,** 1350–1355 (2008).

105. Ally, B. a, Jones, G. E., Cole, J. a & Budson, A. E. Sensory gating in patients with Alzheimer's disease and their biological children. *Am. J. Alzheimers. Dis. Other Demen.* **21,** 439–47 (2007).

106. Pun, S., Santos, A. F., Saxena, S., Xu, L. & Caroni, P. Selective vulnerability and pruning of phasic motoneuron axons in motoneuron disease alleviated by CNTF. *Nat. Neurosci.* **9,** 408–419 (2006).

107. Re, D. B. *et al.* Necroptosis drives motor neuron death in models of both sporadic and familial ALS. *Neuron* **81,** 1001–1008 (2015).

108. Della Sala, S., Spinnler, H. & Venneri, a. Walking difficulties in patients with Alzheimer's disease might originate from gait apraxia. *J. Neurol. Neurosurg.*

Psychiatry **75,** 196–201 (2004).

109. Ebersbach, G. *et al.* Comparative analysis of gait in Parkinson's disease, cerebellar ataxia and subcortical arteriosclerotic encephalopathy. *Brain* **122,** 1349–1355 (1999).

110. Matsushima, A. *et al.* Clinical assessment of standing and gait in ataxic patients using a triaxial accelerometer. *Cerebellum & Ataxias* 1–7 (2015). doi:10.1186/s40673-015-0028-9

111. Stolze, H. *et al.* Typical features of cerebellar ataxic gait. *J. Neurol. Neurosurg. Psychiatry* **73,** 310–312 (2002).

112. Arthur, M. M. P., Thornby, M. S. J. & Kharas, N. F. Clinical Assessment of Spasticity Problem in Spinal Cord Injury : **77,** (1996).

113. Barton, P. M. & Hayes, K. C. Neck flexor muscle strength, efficiency, and relaxation times in normal subjects and subjects with unilateral neck pain and headache. *Arch. Phys. Med. Rehabil.* **77,** 680–687 (1996).

114. Campagnolo, D., Davis, B. A. & Blacksin, M. F. Computed Tomography- Guided Aspiration of a Ganglion Cyst of the Anterior Cruciate Ligament : A Case Report. **77,** (1996).

115. Canela, M., Ama, A. J. & Pons, J. L. Converging Clinical and Engineering Research on Neurorehabilitation. *Converging Clin. Eng. Res. NR* **1,** 255–258 (2013).

116. Chappell, R. Letter to the editor. *Int. J. Radiat. Oncol. Biol. Phys.* **36,** 988–989 (1996).

117. Chuang, T., Lb, S.-W. & Chan, R. Guillain-Barr6 Syndrome : An Unusual Complication. **77,** 729–731 (1996).

118. Halbertsma, J. P. K., Van Bolhuis, A. I. & G??eken, L. N. H. Sport stretching: Effect on passive muscle stiffness of short hamstrings. *Arch. Phys. Med. Rehabil.* **77,** 688–692 (1996).

119. Hillen, M. E., Wagner, M. L. & Sage, J. I. 'Subclinical' orthostatic hypotension is associated with dizziness in elderly patients with Parkinson disease. *Arch. Phys. Med. Rehabil.* **77,** 710–712 (1996).

120. J.H., P. Case for gait analysis as part of the management of incomplete spinal cord injury. *Spinal Cord* **41,** 479–482 (2003).

121. Keenan, A. M. & Bach, T. M. Video assessment of rearfoot movements during walking: A reliability study. *Arch. Phys. Med. Rehabil.* **77,** 651–655 (1996).

122. Kerrigan, D. C., Abdulhadi, H. M., Ribaudo, T. A. & Della Croce, U. Biomechanic effects of a contralateral shoe-lift on walking with an immobilized knee. *Arch. Phys. Med. Rehabil.* **78,** 1085–1091 (1997).

123. Kerrigan, D. C., Deming, L. C. & Holden, M. K. Knee recurvatum in gait: A study of associated knee biomechanics. *Arch. Phys. Med. Rehabil.* **77,** 645–650 (1996).

124. Kohlmeyer, K. M., Hill, J. P., Yarkony, G. M. & Jaeger, R. J. Electrical stimulation and biofeedback effect on recovery of tenodesis grasp: A controlled study. *Arch. Phys. Med. Rehabil.* **77,** 702–706 (1996).

125. Krawetz, P. & Nance, P. Gait analysis of spinal cord injured subjects: Effects of injury level and spasticity. *Arch. Phys. Med. Rehabil.* **77,** 635–638 (1996).

126. Roorda, L. D., Roebroeck, M. E., Lankhorst, G. J., Van Tilburg, T. & Bouter, L. M. Measuring functional limitations in rising and sitting down: Development of a

questionnaire. *Arch. Phys. Med. Rehabil.* **77,** 663–669 (1996).

127. Sutton, J. P., DeJong, G. & Wilkerson, D. Function-based payment model for inpatient medical rehabilitation: An evaluation. *Arch. Phys. Med. Rehabil.* **77,** 693–701 (1996).

128. Boudarham, J. *et al.* Variations in Kinematics during Clinical Gait Analysis in Stroke Patients. *PLoS One* **8,** (2013).

129. Ferrarello, F. *et al.* Tools for observational gait analysis in patients with stroke: a systematic review. *Phys. Ther.* **93,** 1673–85 (2013).

130. Kent, P., Hill, K. & Bernhardt, J. Functional prediction post-stroke. *Aust J Physiother* **39,** 281–289 (1993).

131. Vicenzino, G. & Twomey, L. Sideflexion induced lumbar spine conjunct rotation and its influencing factors. *Aust. J. Physiother.* **39,** 299–306 (1993).

132. Riddoch, S. & Grimmer, K. Developing a clinical indicator for obstructive mastitis. *Aust. J. Physiother.* **39,** 321–322 (1993).

133. Stevenson, T. J. & Garland, S. J. Standing balance during internally produced perturbations in subjects with hemiplegia: Validation of the balance scale. *Arch. Phys. Med. Rehabil.* **77,** 656–662 (1996).

134. Sport, M. Concept for clinical motion analysis applied biomechanics MEDICINE.

135. Hebert, L. E. *et al.* Upper and lower extremity motor performance and functional impairment in Alzheimer's disease. *Am. J. Alzheimers. Dis. Other Demen.* **25,** 425–31 (2010).

136. von Euler, C. On the central pattern generator for the basic breathing rhythmicity. *J.*

Appl. Physiol. **55,** 1647–59 (1983).

137. Lindsey, B. G., Rybak, I. A. & Smith, J. C. Computational models and emergent properties of respiratory neural networks. *Compr. Physiol.* **2,** 1619–1670 (2012).

138. Courtine, G. *et al.* Recovery of supraspinal control of stepping via indirect propriospinal relay connections after spinal cord injury. *Nat. Med.* **14,** 69–74 (2008).

139. Osuna-Carrasco, L. P. *et al.* Quantitative analysis of hindlimbs locomotion kinematics in spinalized rats treated with Tamoxifen plus treadmill exercise. *Neuroscience* **333,** 151–161 (2016).

140. Buchman, A. S. & Bennett, D. A. Loss of motor function in preclinical Alzheimer ' s disease. *Expert Rev Neurother.* **11,** 665–676 (2011).

141. Lorke, D. E., Lu, G., Cho, E. & Yew, D. T. Serotonin 5-HT2A and 5-HT6 receptors in the prefrontal cortex of Alzheimer and normal aging patients. *BMC Neurosci.* **7,** 36 (2006).

142. Zidan, M. *et al.* Alterações motoras e funcionais em diferentes estágios da doença de Alzheimer. *Rev. Psiquiatr. Clin.* **39,** 161–165 (2012).

143. Setogawa, S., Yamaura, H., Arasaki, T., Endo, S. & Yanagihara, D. Deficits in memory-guided limb movements impair obstacle avoidance locomotion in Alzheimer's disease mouse model. *Sci. Rep.* **7220,** 1–10 (2014).

144. Jouvet, M. Physiological Reviews. *Physiol. Rev.* **47,** 117–177 (1941).

145. Shah, P. K. *et al.* Variability in step training enhances locomotor recovery after a spinal cord injury. *Eur. J. Neurosci.* **36,** 2054–2062 (2012).

146. Lovely, R. G., Gregor, R. J., Roy, R. R. & Edgerton, V. R. Effects of training on the recovery of full-weight-bearing stepping in the adult spinal cat. *Exp. Neurol.* **92,** 421–435 (1986).

147. de Leon, R. D., Hodgson, J. A., Roy, R. R. & Edgerton, V. R. Locomotor capacity attributable to step training versus spontaneous recovery after spinalization in adult cats. *J. Neurophysiol.* **79,** 1329–1340 (1998).

148. Reinkensmeyer, D. J. *et al.* A robotic stepper for retraining locomotion in spinal-injured rodents. **3,** 2889–2894 vol.3 (2000).

149. Leclaire, R. *et al.* Back school in a first episode of compensated acute low back pain: a clinical trial to assess efficacy and prevent relapse. *Arch. Phys. Med. Rehabil.* **77,** 673–679 (1996).

150. D, P., Stern, Y. & Pelton, G. H. Combining early markers strongly predicts conversion from mild cognitive impairment to Alzheimer's disease D. *Biol Psychiatry.* **64,** 871–879 (2009).

151. Fong, A. J. Spinal Cord-Transected Mice Learn to Step in Response to Quipazine Treatment and Robotic Training. *J. Neurosci.* **25,** 11738–11747 (2005).

152. Ziegler, M. D., Zhong, H., Roy, R. R. & Edgerton, V. R. Why Variability Facilitates Spinal Learning. *J. Neurosci.* **30,** 10720–10726 (2010).

153. Liu, X. Z. Neuronal and glial apoptosis after traumatic spinal cord injury. . *J. Neurosci.* **17,** 5395–5406 (1997).

154. Guertin, P. A. Central Pattern Generator for Locomotion: Anatomical, Physiological, and Pathophysiological Considerations. *Front. Neurol.* **3,** 183 (2013).

155. Dykman, R. A. and P. S. S. Successive and maintained conditioning in spinal carnivores. *J Comp Physiol Psychol.* **49,** 27–35 (1956).

156. Patterson, M. M., J. E. Steinmetz, A. L. B. and A. G. R. Associative processes in spinal reflexes. *Conditioning* 637–650 (1982).

157. Patterson, M. M., C. F. C. and R. F. T. Effects of a classical conditioning paradigm on hind-limb flexor nerve response in immobilized spinal cats. *J Comp Physiol Psychol 84* **84,** 88–97 (1973).

158. Patterson, M. M. Classical conditioning of spinal reflexes: The first seventy years. *Model systems and the neurobiology of associative learning: A Festschrift in honor of Richard F. Thompson* 1–22 (2001).

159. Yeoman, M. S., Brierley, M. J. & Benjamin, P. R. Central pattern generator interneurons are targets for the modulatory serotonergic cerebral giant cells in the feeding system of Lymnaea. *J Neurophysiol* **75,** 11–25 (1996).

160. Groves, P., D. Glanzman, M. P. and R. T. Excitability of cutaneous afferent terminals during habituation and sensitization in acute spinal cat. *Brain Res.* **18,** 388–392 (1970).

161. Durkovic, R. G. Retention of a classically conditioned reflex response in spinal cat. *Behav Neural Biol* **43,** 12–20 (1985).

162. Durkovic, R. G. and L. J. P. D-2-amino-5-phosphonovalerate, and NMDA receptor antagonist, blocks induction of associative long-term potentiation of the flexion reflex in spinal cat. *Neurosci Lett* **257,** 162–164 (1988).

163. Horridge, G. A. Learning of leg position by headless insects. *Nature* **193,** 697–698 (1962).

164. Buerger, A. A. and A. F. Learning of leg position in chronic spinal rats. *Nature* **225,** 751–752 (1970).

165. Buerger, A. and A. D. Spinal kittens: Long-term increases in electromyograms due to a conditioning routine. *Physiol. Behav.* **3,** 99–103 (1968).

166. Grau, J. W. & Hook, M. A. Spinal Neurons Exhibit a Surprising Capacity to Learn and a Hidden Vulnerability When Freed from the Brain ' s Control. 177–180 (2006).

167. Crown, E. D., A. R. Ferguson, R. L. J. and J. W. G. Instrumental learning within the spinal cord. II. Evidence for central mediation. *Physiol Behav* **77,** 259–267 (2002).

168. Joynes, R. L., A. R. Ferguson, E. D. Crown, B. C. P. and J. W. G. Instrumental learning within the spinal cord: V. Evidence the behavioral deficit observed after noncontingent nociceptive stimulation reflects an intraspinal modification. *Behav Brain Res* **141,** 159–170 (2003).

169. Joynes, R. L. and J. W. G. Mechanisms of Pavlovian conditioning: role of protection from habituation in spinal conditioning. *Behav Neurosci* **110,** 1375–1387 (1996).

170. Joseph, M. S., Z. Ying, Y. Zhuang, H. Zhong, A. Wu, H. S. Bhatia, R. Cruz, N. J. Tillakaratne, R. R. Roy, V. R. E. and F. G.-P. Effects of diet and/or exercise in enhancing spinal cord sensorimotor learning. *PLoS One* **7,** e41288 (2012).

171. Gomez-Pinilla, F., J. R. Huie, Z. Ying, A. R. Ferguson, E. D. Crown, K. M. Baumbauer, V. R. E. and J. W. G. BDNF and learning: Evidence that instrumental training promotes learning within the spinal cord by up-regulating BDNF expression. *Neuroscience* **148,** 893–906 (2007).

172. Ittner, L. M. *et al.* Dendritic function of tau mediates amyloid-?? toxicity in

alzheimer's disease mouse models. *Cell* **142,** 387–397 (2010).

173. Joseph, M. S. Mechanisms of spinal learning related to a simple motor task in a mammalian system by. (2016).